

**The Numerical Simulation of Two-Phase  
Flows in Settling Tanks**

**Daniel Brennan**

Thesis submitted for the degree of  
Doctor of Philosophy  
of the University of London

Imperial College of Science, Technology and Medicine  
Department of Mechanical Engineering  
Exhibition Road, London SW7 2BX

January 2001

*Dedicated To My Parents.*

---

## Abstract

This study describes the development and application of a mathematical model of the two-phase flow regime found in settling tanks used in the activated sludge process. The phases present are water, the continuous medium, and activated sludge, the dispersed phase. The flow field is considered to be isothermal, incompressible and without phase change. The model is based on the Drift Flux model where Eulerian conservation equations are used for the mixture mass and momentum together with a convection diffusion equation for modelling the distribution of the dispersed phase. Constitutive relationships are used to model the relative motion between the phases.

The rheological effects of the dispersed phase on the mixture, and of an accumulated settled bed of the dispersed phase, are modelled using a shear thinning Bingham plastic formulation. Empirical relationships are used to model the concentration dependent physical properties of settling velocity, yield stress and plastic viscosity. The effects of turbulence are modelled using a two-equation buoyancy modified  $k-\epsilon$  turbulence model.

In order to obtain the solution to the resulting set of non-linear partial differential equations, a finite volume discretisation technique is employed using the PISO algorithm. This is coupled with a specially developed treatment for pressure correction, here, the hydrostatic pressure is treated separately and the density gradient at the cell face is calculated directly from nodes either side of the cell face.

The performance of the model is assessed by applying it to three validation cases using activated sludge suspensions as the working medium. These are; a lock exchange experiment measuring velocity; a model scale settling tank measuring velocity and concentration and a full scale settling tank measuring velocity and concentration. The results were encouraging with velocity and dispersed phase concentration being generally well predicted throughout.

---

## Acknowledgements

I would like to express my sincere gratitude to my supervisor, Prof. A. D. Gosman, for his guidance, constructive criticism and continued support. I would also like to thank my industrial supervisors Dr Jeremy Dudley and Dr Brian Chambers from the Water Research Center, and the Water Research Center itself for providing the financial support for this research.

Very special thanks are due to Henry Weller for his key and vital support, friendship, invaluable insights and for the use of his research code FOAM. Many thanks also are due to members and previous members of the research group including Mr H Rusche, Dr D Hill, Dr G Tabor, Dr H Jasak and Dr D Clerides for their support and many helpful discussions.

My thanks are also due to Mrs N Scott-Knight who arranged many of the financial and administrative matters.

D Brennan.

December 2000.

# Contents

<b>1</b>	<b>Introduction</b>	<b>23</b>
1.1	Objective . . . . .	24
1.2	Present Contribution . . . . .	25
1.3	Thesis Outline . . . . .	26
<b>2</b>	<b>Settling Tanks Within the Activated Sludge Process</b>	<b>29</b>
2.1	The Activated Sludge Process . . . . .	29
2.2	Types of Settling Tanks . . . . .	30
2.3	Flow Field Characteristics of Settling Tanks . . . . .	32
2.4	Settling Velocity . . . . .	36
2.4.1	Settling of a Single Floc . . . . .	37
2.4.2	Hindered Settling . . . . .	40
2.5	Activated Sludge Rheology . . . . .	45
2.5.1	Bed Form Development . . . . .	49
2.6	Previous Models of Settling Tank Performance . . . . .	52
2.6.1	Single Phase Computational Models . . . . .	52
2.6.2	Dispersed Phase Transport Models . . . . .	56
2.7	Experimental Studies . . . . .	66
2.8	Closure . . . . .	68
<b>3</b>	<b>Mathematical Formulation of Two Phase Flow</b>	<b>73</b>
3.1	Lagrangian Approaches . . . . .	74

3.2	Eulerian Methods in Two Phase Flow . . . . .	76
3.2.1	Averaging. . . . .	77
3.2.2	Two Fluids Model. . . . .	80
3.3	Diffusion (Mixture) Model Field Equations. . . . .	82
3.3.1	Equations of State and Mixture Properties . . . . .	84
3.3.2	Kinematic Constitutive Equations. . . . .	84
3.3.3	Diffusion Model Field Equations . . . . .	86
3.3.4	Drift Flux Model Field Equations . . . . .	87
3.3.5	Closure . . . . .	89
<b>4</b>	<b>Turbulence Modelling.</b>	<b>91</b>
4.1	Introduction. . . . .	91
4.2	General Effects of The Dispersed Phase. . . . .	92
4.3	Buoyancy Effects. . . . .	94
4.4	Buoyancy Modified k- $\epsilon$ equations . . . . .	95
4.5	The Effects of Buoyancy Modification on the flow field. . . . .	96
4.6	Closure . . . . .	102
<b>5</b>	<b>Numerical Solution Procedure.</b>	<b>103</b>
5.1	Introduction. . . . .	103
5.2	Discretisation of the Solution Domain. . . . .	104
5.3	Discretisation of the Governing Differential Equations. . . . .	105
5.3.1	Convection Terms. . . . .	107
5.3.2	Diffusion Terms. . . . .	109
5.3.3	Source Terms. . . . .	110
5.3.4	Final Form of the Discretised Equation. . . . .	111
5.3.5	Pressure Equation. . . . .	112
5.4	Boundary Conditions. . . . .	116
5.4.1	Fixed Value Boundary Conditions . . . . .	117
5.4.2	Fixed Gradient Boundary Conditions . . . . .	118

---

	11
5.4.3 Wall Boundary Conditions . . . . .	118
5.5 Solution Algorithm. . . . .	121
5.6 Conclusions . . . . .	122
<b>6 Model Scale Simulations.</b>	<b>123</b>
6.1 The Lock Exchange Experiment. . . . .	123
6.2 Experimental Procedure. . . . .	124
6.3 Numerical Simulation. . . . .	126
6.3.1 The Physical Properties of Activated Sludge. . . . .	127
6.3.2 Results. . . . .	129
6.3.3 Conclusion. . . . .	132
6.4 The Dahl Experiment. . . . .	138
6.4.1 Physical Properties of Activated Sludge . . . . .	139
6.5 Experimental Apparatus. . . . .	139
6.5.1 Experimental Procedure . . . . .	141
6.6 Numerical Simulation. . . . .	141
6.6.1 Cases (i) and (ii) Full Depth Inlet . . . . .	143
6.6.2 Results Influent Flow Rate 19.1 l/s . . . . .	143
6.6.3 Results Influent Flow rate 5.4 l/s . . . . .	151
6.6.4 Discussion. . . . .	153
6.6.5 Cases (iii) and (iv) Slot Inlet. . . . .	155
6.6.6 Slot Inlet - Single Phase Analysis. . . . .	155
6.6.7 Results Influent Flow Rate 5.2 l/s . . . . .	158
6.6.8 Results Influent Flow Rate 12.0 l/s . . . . .	165
6.7 Discussion. . . . .	168
<b>7 Full Scale Simulations.</b>	<b>171</b>
7.1 Introduction. . . . .	171
7.2 The Experimental Investigation of The Limmattal Settling Tank. . . . .	172

7.3 2D Simulation of the Limmattal Tank . . . . .	177
7.3.1 Results of the 2D Simulation . . . . .	179
7.3.2 The Flow Field within The Hopper. . . . .	184
7.4 3D Simulation of The Limmattal Settling Tank. . . . .	193
7.4.1 Results from a Single Phase Calculation. . . . .	193
7.4.2 Results from The Two Phase Calculations. . . . .	197
7.4.3 Simulation with a 1.042:1 density ratio. . . . .	197
7.4.4 General Description of Flow field. . . . .	198
7.4.5 Simulation with a 2:1 density ratio. . . . .	209
7.4.6 Simulation with a 1.3:1 density ratio. . . . .	209
7.4.7 Mixing and Dispersal of the Density Current . . . . .	217
7.5 Conclusions . . . . .	219
<b>8 Summary and Conclusions.</b>	<b>223</b>
8.1 Summary. . . . .	223
8.2 Suggestions for Further Research. . . . .	227

<b>A Derivation of the Drift Flux Model from the Two Fluid Model.</b>	<b>231</b>
A.1 Mixture Continuity. . . . .	231
A.2 The Mixture Momentum Equations. . . . .	232
A.3 Continuity Equation for the Dispersed Phase. . . . .	235

# List of Figures

2.1 Schematic of Rectangular Settling Tank. . . . .	31
2.2 Schematic of Cylindrical Settling Tank. . . . .	31
2.3 Schematic of a Density Current within a Settling Tank. . . . .	33
2.4 Variation of Drag Coefficient with Rep for a Single Floc. Settling Velocity from Li (1987) . . . . .	40
2.5 Stages in Batch Settling Experiment. . . . .	43
2.6 Settling Velocity versus Solids Fraction. . . . .	45
2.7 Activated Sludge Rheogram, adapted from Toorman(1992). . . . .	46
3.1 Streamline and Velocity Vector Relationship in Two-Phase Flow. Ishii (1975). . . . .	85
4.1 Buoyancy Modified k- $\epsilon$ Model, Velocity Field. . . . .	99
4.2 Standard k- $\epsilon$ Model, Velocity Field. . . . .	99
4.3 Laminar Flow, Velocity Field. . . . .	99
4.4 Buoyancy Modified k- $\epsilon$ Model, Effective Viscosity. . . . .	100
4.5 Standard k- $\epsilon$ Model, Effective Viscosity. . . . .	100
4.6 Buoyancy Modified k- $\epsilon$ Model, Turbulent Intensity. . . . .	101
4.7 Standard k- $\epsilon$ Model, Turbulent Intensity. . . . .	101
4.8 Comparisons of Laminar Flow, Standard and Buoyancy Modified k- $\epsilon$ Models. . . . .	101
5.1 Control Volume. . . . .	104

5.2 Control Volume with Boundary Face. . . . .	117
6.1 Schematic of Lock exchange Experiment. . . . .	125
6.2 Interface Velocity - Lock Exchange Experiment. . . . .	130
6.3 Mixture Velocity, Vector Field. 10s . . . . .	134
6.4 Mixture Velocity, Vector Field. 35s . . . . .	134
6.5 Mixture Velocity, Vector Field. 50s . . . . .	134
6.6 Solids Fraction.10s . . . . .	135
6.7 Solids Fraction.35s . . . . .	135
6.8 Solids Fraction.50s . . . . .	135
6.9 Secondary Flow 0.80m. t = 50s. . . . .	136
6.10 Secondary Flow 0.85m. t = 50s. . . . .	136
6.11 Secondary Flow 0.87m. t = 50s. . . . .	136
6.12 Isosurface of Median Value of Solids Fraction. t = 50sec. . . . .	137
6.13 Schematic of Albourg Settling Tank. . . . .	140
6.14 Boundary Conditions. Full Depth Inlet. . . . .	143
6.15 Velocity and Solids Fraction Plots, 19.1l/s. Early part of Experiment. . . . .	145
6.16 Velocity and Solids Fraction Plots,19.1l/s. Late part of Experiment. . . . .	145
6.17 Flow rate 19.1l/s. Mixture Velocity, Vector Plot 900s. . . . .	146
6.18 Flow rate 19.1l/s. Mixture Velocity, Vector Plot 2100s. . . . .	146
6.19 Flow rate 19.1l/s. Mixture Velocity,Velocity Vector 3200s. . . . .	146
6.20 Flow rate 19.1l/s. Solids Fraction 600s. . . . .	147
6.21 Flow rate 19.1l/s. Solids Fraction 1700s. . . . .	147
6.22 Flow rate 19.1l/s. Solids Fraction 3000s. . . . .	147
6.23 Flow rate 19.1l/s. Mixture Velocity, Vector Plot 7400s. . . . .	148
6.24 Flow rate 19.1l/s. Mixture Velocity, Vector Plot 8400s. . . . .	148
6.25 Flow rate 19.1l/s. Mixture Velocity, Velocity Vector 9400s. . . . .	148

6.26 Flow rate 19.1l/s. Solids Fraction 7100s.	149
6.27 Flow rate 19.1l/s. Solids Fraction 8100s.	149
6.28 Flow rate 19.1l/s. Solids Fraction 9100s.	149
6.29 Flow rate 19.1l/s. Laminar Viscosity 7100s.	150
6.30 Flow rate 19.1l/s. Turbulent Viscosity 7100s.	150
6.31 Velocity and Solids Fraction Plots, 5.4l/s. Early part of Experiment.	152
6.32 Velocity and Solids Fraction Plots, 5.4l/s. Late part of Experiment.	152
6.33 Computational Domain. Slot Inlet. Scaled 2x Vertically.	156
6.34 Boundary Conditions. Slot Inlet.	157
6.35 Flow rate 5.2l/s. Slot Inlet. Vector Field. Single Phase Flow.	157
6.36 Velocity and Solids Fraction Plots, 5.2l/s. Early part of Experiment.	159
6.37 Velocity and Solids Fraction Plots, 5.2l/s. Late part of Experiment.	159
6.38 Flow rate 5.2l/s. Mixture Velocity. Vector Plot 900s.	160
6.39 Flow rate 5.2l/s. Mixture Velocity. Vector Plot 1920s.	160
6.40 Flow rate 5.2l/s. Mixture Velocity. Velocity Vector 2800s.	160
6.41 Flow rate 5.2l/s. Solids Fraction 600s.	161
6.42 Flow rate 5.2l/s. Solids Fraction 1600s.	161
6.43 Flow rate 5.2l/s. Solids Fraction 2200s.	161
6.44 Flow rate 5.2l/s. Mixture Velocity. Vector Plot 7000s.	162
6.45 Flow rate 5.2l/s. Mixture Velocity. Vector Plot 7900s.	162
6.46 Flow rate 5.2l/s. Mixture Velocity. Vector Plot 8800s.	162
6.47 Flow rate 5.2l/s. Solids Fraction 5100s.	163
6.48 Flow rate 5.2l/s. Solids Fraction 7680s.	163
6.49 Flow rate 5.2l/s. Solids Fraction 8280s.	163
6.50 Flow rate 5.2l/s. Laminar Viscosity 7200s.	164
6.51 Flow rate 5.2l/s. Turbulent Viscosity 7200s.	164

6.52 Velocity and Solids Fraction Plots, 12.0l/s. Early part of Experiment.	166
6.53 Velocity and Solids Fraction Plots, 12.0l/s. Late part of Experiment.	166
6.54 Flow rate 12.0l/s. Vector Field 2550s. Deposition of Settled Bed.	167
6.55 Flow rate 12.0l/s. Vector Field 2700s. Erosion of Settled Bed.	167
6.56 Flow rate 12.0l/s. Vector Field 2850s. Re-deposition of Settled Bed.	167
7.1 Schematic of Limmattal Settling Tank.	173
7.2 Mid-Depth Section through the Inlet Baffles. Limmattal Settling Basin.	174
7.3 Computational Domain. 2D Simulation. Limmattal Settling Basin.	177
7.4 Boundary Conditions. 2D Simulation. Limmattal Settling Basin.	178
7.5 Velocity Profiles. Density Ratio 1.042:1. 2D Simulation.	180
7.6 Solids Fraction. Density Ratio 1.042:1. 2D Simulation.	180
7.7 Velocity. Comparative Study. Density Ratios 1.042:1 and 2:1. Fr 0.0659. 2D Simulation.	181
7.8 Solids Fraction. Comparative Study. Density Ratios 1.042:1 and 2:1. Fr 0.0659. 2D Simulation.	181
7.9 Velocity Field. Density Ratio; 1042:1000. t = 4500s. 2D Simulation.	182
7.10 Solids Fraction. Density Ratio; 1042:1000. t = 4500s. 2D Simulation.	182
7.11 Turbulent Viscosity. Density Ratio; 1042:1000. t = 4500s. 2D Simulation.	182
7.12 Vector Field 212s.	187

7.13 Flow Field Schematic. . . . .	187
7.14 Solids Fraction 212s. . . . .	187
7.15 Vector Field 512s. . . . .	188
7.16 Flow Field Schematic. . . . .	188
7.17 Solids Fraction 512s. . . . .	188
7.18 Vector Field 2500s. . . . .	189
7.19 Flow Field Schematic. . . . .	189
7.20 Solids Fraction 2500s. . . . .	189
7.21 Vector Field 3500s. . . . .	190
7.22 Flow Field Schematic. . . . .	190
7.23 Solids Fraction 3500s. . . . .	190
7.24 Vector Field 7500s. . . . .	191
7.25 Flow Field Schematic. . . . .	191
7.26 Solids Fraction 7500s. . . . .	191
7.27 Laminar Viscosity 7500s. . . . .	192
7.28 Computational Domain . . . . .	194
7.29 Computational Domain, First 10m. . . . .	195
7.30 Velocity Profiles. Single Phase Flow Regime. 3D Simulation. . . . .	196
7.31 Velocity Profiles. Single Phase Flow Regime. 3D Simulation. . . . .	196
7.32 Velocity Profiles. Density Ratio 1.042:1. 3D Simulation. . . . .	199
7.33 Velocity Profiles. Density Ratio 1.042:1. 3D Simulation. . . . .	199
7.34 Solids Fraction. Density Ratio 1.042:1. 3D. Simulation. . . . .	200
7.35 Solids Fraction. Density Ratio 1.042:1. 3D Simulation. . . . .	200
7.36 Velocity Field. Density Ratio; 1042:1000. z = 1.75m. t = 6155s. . . . .	202
7.37 Velocity Field. Density Ratio; 1042:1000. z = 0.5m. t = 6155s. . . . .	203
7.38 Velocity Field. Density Ratio; 1042:1000. z = 3.75m. t = 6155s. . . . .	203
7.39 Solids Fraction. Side View. Density Ratio; 1042:1000. t = 6155s. . . . .	203
7.40 Solids Fraction. Bed Form Development. Density Ratio; 1042:1000. z = 1.75m. t = 6030s. . . . .	204

7.41 Sludge Hopper. Return Sludge Density Current. Density Ra- tio;1042:1000. z = 1.75m. t = 6155s. . . . .	205
7.42 Horizontal Velocity Component. 'Mountain Plot'. Density Ra- tio; 1042:1000. t = 6155s. . . . .	205
7.43 Secondary Flow 5m . . . . .	207
7.44 Secondary Flow 20m . . . . .	207
7.45 Secondary Flow 40m . . . . .	207
7.46 Velocity Profiles. Density Ratio 2:1. 3D Simulation. . . . .	211
7.47 Velocity Profiles. Density Ratio 2:1. 3D Simulation. . . . .	211
7.48 Solids Fraction. Density Ratio 2:1. 3D Simulation. . . . .	212
7.49 Solids Fraction. Density Ratio 2:1. 3D Simulation. . . . .	212
7.50 Velocity Field. Density Ratio; 2:1. z = 1.75m. t = 5233s. . . . .	213
7.51 Velocity Field. Surface Return Current. Density Ratio; 2:1. t = 5283s. . . . .	213
7.52 Velocity Profiles. Density Ratio 1.3:1. 3D Simulation. . . . .	214
7.53 Velocity Profiles. Density Ratio 1.3:1. 3D Simulation. . . . .	214
7.54 Solids Fraction. Density Ratio 1.3:1. 3D. Simulation. . . . .	215
7.55 Solids Fraction. Density Ratio 1.3:1. 3D Simulation. . . . .	215
7.56 Iso Surface. Solids Fraction = 0.003. Density Ratio 1.3:1. 3D Simulation. . . . .	216
7.57 Schematic of Density Current Velocity Profiles. . . . .	218
7.58 Settling Tank Flow Field Schematic. . . . .	219

# Nomenclature

## Greek

$\alpha$	Solids Fraction;
$\gamma$	Local Shear Rate.
$\epsilon$	Turbulent kinetic energy dissipation rate. Sediment erosion rate.
$\rho$	Density.
$\mu$	Dynamic Viscosity.
$\mu_t$	Turbulent Viscosity.
$\nu$	Kinematic Viscosity.
$\nu_t$	Turbulent Kinematic Viscosity.
$\sigma$	Turbulent Prandtl number.
$\sigma^t$	Total Stress Tensor.
$\tau_w$	Reynolds Stress Tensor.
$\tau_y$	Wall Shear Stress.
$\tau_y$	Yield Stress.
$\tau$	Viscous Shear Stress Tensor.
$\chi$	Phase Indicator Function.

## Roman

$\mathbf{A}_f$	Cell Face Area Vector.
$C$	Concentration.
$C_d$	Dimensionless Drag Coefficient.
$C_L$	Lift Coefficient.
$d$	Diameter.

$\mathbf{d}_n$	Relative Position of Neighbouring Coefficient.
$\mathbf{g}$	Gravity Vector.
$F$	Densimetric Froude Number.
$\mathbf{F}$	Total Force Vector, Cell Face Flux.
$\mathbf{F}_d$	Drag Force.
$\mathbf{j}$	Phase Volumetric Flux.
$\mathbf{I}$	Unit Tensor.
$k$	Turbulent Kinetic Energy.
$L$	Direction cosines.
$m_p$	Mass of Particle.
$\mathbf{M}$	Interfacial Momentum Transfer.
$M_m$	Capillary Force.
$\mathbf{n}_k$	Surface Normal Interior to Phase k.
$N$	Number of Realisations.
$P$	Pressure.
$r$	Particle radius.
$R$	Universal Gas Constant.
$R_e$	Reynolds Number.
$Re_p$	Particle Reynolds Number.
$S_k$	Surface Propogation Speed.
$S_p$	Implicit Part of Source Term.
$S_u$	Explicit Part of Source Term.
$t, T$	Time, Temperature.
$t_p$	Particle Responce Time.
$\mathbf{u}$	Velocity Vector.
$\mathbf{u}_r$	Relative Velocity.
$v_{dj}$	Drift Velocity.
$\nabla V, V$	Volume, Magnitude of Relative Velocity Vector.
$V_o$	Terminal Velocity.
$V_s$	Settling Velocity.
$y^+$	Normalised Distance to the Wall.

## Subscripts

k	Pertaining to Phase k.
c	Pertaining to the Continuous Phase.
d	Pertaining to the Dispersed Phase.
dj	Pertaining to the Drift Velocity.
f	Pertaining to the Fluid.
in	Pertaining to the Inlet Value.
m	Pertaining to the Mixture.
out	Pertaining to the Outlet Value.
p	Pertaining to the Particle.
r	Relative.
$\alpha$	Pertaining to the Solids Fraction.
$\phi$	Pertaining to equation $\phi$ .
eff	Effective Value.

## Superscripts

,	Turbulent fluctuation.
"	Surface fluctuation.
t	Turbulent.
T	Transpose.
*	Intermediate value.

# Chapter 1

## Introduction

The activated sludge process is based on the observation that when waste water is aerated for a period of time the content of organic matter is reduced and a flocculent sludge is formed, Hanel(1988). Soluble biochemical oxygen demand, BOD, is also reduced. Sedimentation tanks are used in the process to settle the sludge from suspension and to thicken the resulting sediment, Stamou and Rodi (1984).

Settling by gravity is of great importance in water and waste water treatment where settling tanks can account for 30% of total plant investment. Despite the practical importance of these tanks, current design practice relies heavily on empirical formulae which do not take full account of the detailed hydrodynamics of the system.

In recent years efforts have been made to replace empirical design methods by mathematical models which accurately reproduce the physical processes involved in sedimentation tanks, Stamou and Rodi (1984). The basic differential equations governing the flow and concentration field can be assembled and solved by numerical methods on computers. In this way the effects of geometric changes in tank configuration and variations in other parameters, such as influent flow rates and the sedimentation characteristics of suspended solids, can be predicted. This would make a contribution to optimising tank

design and operational efficiency.

The effects of other physico - chemical processes such as flocculation and particle break - up, can be included in the mathematical model thereby indicating what effects these processes have on the overall efficiency of the tank.

### 1.1 Objective

The aim of this work is to analyse and model the two phase flow regime found in settling tanks and compare the model with experimental data. The two phases present are water, the continuous medium and activated sludge, the dispersed phase. For this study the flow field is considered to be isothermal, incompressible and without phase change. The main features of this regime are;

**1)** The gravitational settling of a heavier dispersed phase. As the concentration of the dispersed phase increases with settling, the hydrodynamic field around each particle is affected by the proximity of its neighbours and the drag on each particle increases. The net effect is a reduction in settling velocity. This process is known as hindered settling and will be discussed in Chapter 2.

**2)** The presence of a sediment-driven density current brought about by the inflow of a two phase mixture which is heavier than the fluid within the upper part of the settling tank. This influent mixture flows as a bottom current underneath the less dense tank fluid, De Vantier and Larock (1987). The current derives its momentum from the conversion of the gravitational potential energy of the mixture at the inlet into the kinetic energy of the density current.

**3)** Non-Newtonian shear-thinning behaviour of the dispersed phase and of the mixture, coupled with the gradual accumulation of a thixotropic settled bed of the dispersed phase.

**4)** Modifications to turbulence brought about by density stratification, the presence of a particulate dispersed phase, non-Newtonian rheology and regions

of low Reynolds number in areas of the flow field. These factors affect the choice of turbulence model.

It is necessary to characterise the relative importance of these features and include the most significant in the subsequent mathematical model. Wherever possible, the components of the features that make up the model were tested against analytical solutions, experimental data or both.

## 1.2 Present Contribution

A literature survey was undertaken to establish the current status of experimental analysis and numerical simulation of settling tank performance, this survey is presented in Chapter 2. There are a number of diverse physical features of the flow field within the settling tank, outlined in section 1.1. In order to encompass this range of features the survey was extended to cover the fields of non-Newtonian rheology and the deposition and re-entrainment of cohesive and non-cohesive sediments.

A Drift flux model, Ishii(1975) Chapter 3, which consists of a mixture continuity equation, a mixture momentum equation and a convection diffusion equation for the dispersed phase has been coded in finite volume form. Concentration dependent Bingham plastic rheology within the mixture is also simulated, section 2.5. Within the two phase flow field, turbulence is simulated by a buoyancy modified  $k-\epsilon$  model. The equation set for this model is presented in Chapter 4.

Effort has been extended in developing a procedure for the interpolation of the momentum equation onto cell faces, Rhie and Chow(1983), for buoyancy dominated problems on co-located meshes, Weller(1997). The treatment of density within this procedure enables velocity fields at a low densimetric Froude number to be correctly predicted with greater accuracy and stability in the pressure correction equation set.

The resulting model has been compared against experimental data for velocity and concentration gathered on model scale settling tanks, Chapter 6, and full scale settling tanks, Chapter 7, the later calculation being carried out in 3D. The numerical simulations adequately reproduced the experimental conditions, very good agreement was found for velocity and concentration at some stations with good to adequate agreement found at the rest. New features of the flow field have been identified, these were obtained from detailed examination of the hydrodynamics within the hopper and main body of the tank over a long time period. In the hopper, as the concentration of the dispersed phase increases, laminar viscosity gradually becomes the dominant force in shaping the flow field. The fluid mechanics and mechanism of mixing at the interface of the density driven current and the ambient medium in the main body of the tank is also examined in some detail.

## 1.3 Thesis Outline

In Chapter 2 the activated sludge process is outlined together with the role of settling tanks in this process. Previous models of settling tank performance are reviewed together with a survey of experimental studies. Additional material on the non-Newtonian rheology of activated sludge mixtures and the behaviour of settled sediment beds is presented.

Chapter 3 is devoted to the mathematical model of this type of two - phase flow. The model is based on the notion of interpenetrating continua within an Eulerian framework. This framework is adopted for the derivation of the conservation equations for mass and momentum of the mixture and the mass of the dispersed phase.

Chapter 4 deals with the modelling of turbulence. The standard and buoyancy modified  $k - \epsilon$  models are presented. A critical comparison is made of the standard and buoyancy modified  $k - \epsilon$  model in a stably stratified density

driven flow field. Finally the boundary conditions for the equation set are described.

The method of solution of the set of governing equations is described in Chapter 5. Discretisation of the continuous partial differential equations using the finite-volume, co-located grid arrangement is outlined, together with a special treatment for density which enhances the stability and accuracy of the solution. Higher order differencing schemes are also considered.

The results of comparisons with experimental data are presented in Chapters 6 and 7. The numerical model is compared with data gathered in;

- i) a lock exchange experiment simulated in 2D and 3D, velocity comparisons only, with data gathered by Larsen(1977).
- ii) a large scale model tank simulated in 2D comparing velocity and concentration in the free stream and the settled bed, data gathered by Dahl(1993).
- iii) a full scale settling tank simulated in 2D and 3D, comparing velocity and concentration in the free stream and modeling the accumulation and withdrawal of the settled bed, data gathered by Ueberl(1995).

Discussion of the results and hydrodynamics of the flow field also takes place within these chapters. Chapter 8 summarises the findings and conclusions of the study and presents some suggestions for further work on the subject.

## Chapter 2

# Settling Tanks Within the Activated Sludge Process

### 2.1 The Activated Sludge Process

The activated sludge process has two main stages namely aeration and sedimentation. The waste water is fed into the aeration tank, also known as the biological or primary reactor, oxygen is supplied to the waste water either by mechanical aeration or by bubbling compressed air or oxygen through the reactor, Hanel (1988). The sludge produced consists of a heterogeneous population of micro organisms. The makeup of these changes continually in response to variations in the composition of waste water and environmental conditions. The micro organisms present include unicellular bacteria, fungi, algae, protozoa and rotifers. A food chain is thus established whereby primary waste is consumed by bacteria which are subsequently consumed by other micro organisms.

The flocculant and sedimentary nature of the sludge generated in the primary reactor is to some extent determined by the food to micro organism (F/M) ratio. For most waste waters the optimum F/M ratio is between 0.3

and 0.6 kg BOD per day applied per kg of activated sludge in the aeration tank, Hanel(1988).

The sludge flocs or particles, range in size from  $10^{-9}$ m to  $10^{-3}$ m. They are very heterogeneous in composition and shape. They consist of suspended organic and inorganic matter with a large composition of bacteria held together by a colloidal matrix. Floc shapes can be characterised as spherical, flattish, star shaped, interlaced, rugged and lobulated or loosely reticulated amorphous flocs, Hanel(1988). Particle size distribution at the outlet of the aeration tank is detailed by Roth(1981) and Patry and Takacs (1992).

At some plants the outflow from the aerator is fed to a flocculation unit where synthetic polymers or iron salts can be added to promote aggregation of the smaller particles. Mixing, by stirring or inducing high velocity gradients of the incoming fluid, promotes coagulation. The outflow is then fed to the settling tank, often called the ‘secondary settling tank’ or ‘secondary clarifier’ at this location. It is this component, described below in detail, which is the focus of the present research.

### 2.2 Types of Settling Tanks

The majority of settling tanks are either rectangular, Figure 2.1, or cylindrical, Figure 2.2, in shape, Smethurst(1992). No one standard design exists but a typical rectangular tank can be around 30m long, 3m deep and 10m wide with the inlet and outlet at opposite ends of the longest dimension. This is the type of tank studied in this report. Baffles, which may be perforated, are sometimes placed near the inlet to reduce the momentum of the influent jet. Sludge settles at the bottom of the tank and is withdrawn by scrapers moving towards a hopper in the tank floor.

Cylindrical tanks are around 30m in diameter with depths from 3.5m at the centre to 2.5 m at the circumferential walls. The floor of these tanks tends

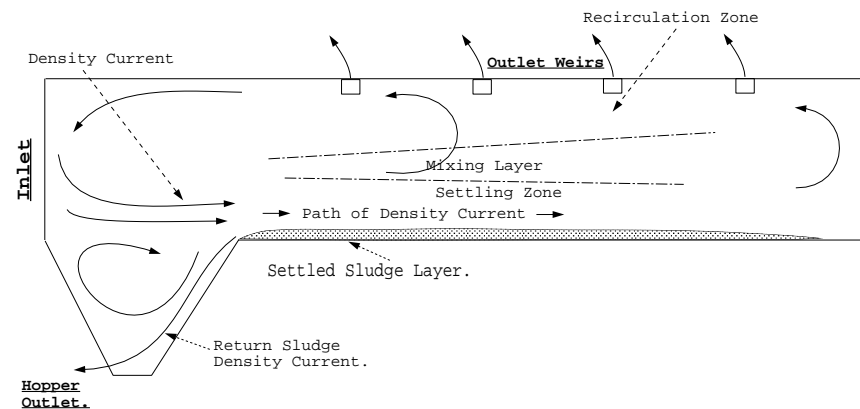


Figure 2.1: Schematic of Rectangular Settling Tank.

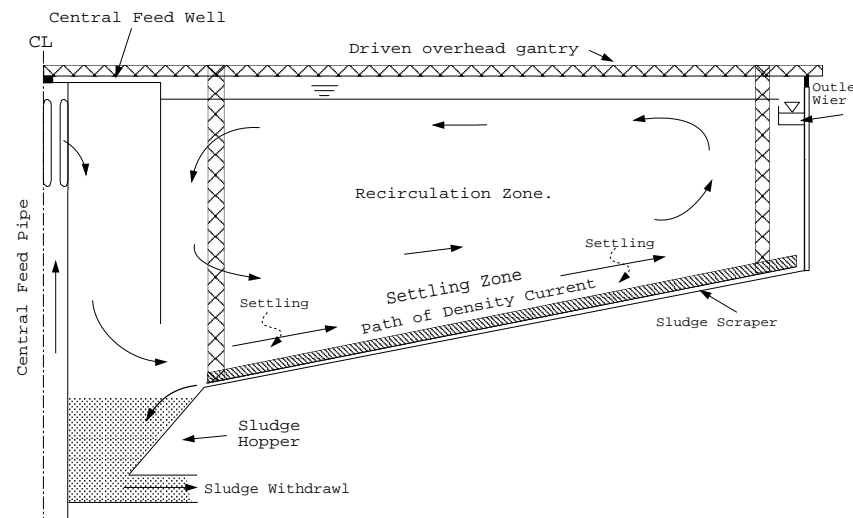


Figure 2.2: Schematic of Cylindrical Settling Tank.

to slope towards the centre. Inflow generally occurs through a central feed well with effluent weirs at the tank circumference, Smethurst(1992). Sediment collection is usually affected by scrapers on a revolving gantry pushing the sludge towards a central hopper where it is withdrawn. In both rectangular and cylindrical tanks, the scrapers and their drive mechanisms affect tank hydrodynamics and can cause disturbances to the sediment layer, Smethurst(1992). The overflow rate, defined as the total volume of influent per day divided by the tank surface area, is typically in the region of 9 to  $60\text{m}^3/\text{day}/\text{m}^2$ .

Inlet velocities to settling tanks are in the region of 0.1 m/s to 0.6 m/s. Slower influent velocities may cause sedimentation in the inlet feed system and higher velocities may cause the flocs to be broken up by high shear, this is known as floc disruption. Settleable solids concentration in the influent is typically in the range 500 to 5000mg/l. Solids densities are typically  $1300 \text{ kg/m}^3$  to  $2000 \text{ kg/m}^3$ , although in this study a solids density of  $1042 \text{ kg/m}^3$  was used in the simulation of the Limmattal settling tank in Chapter 7, Ueberl(1995). Settling studies of the solids fraction by batch settling tests, discussed in section 2.4.2, indicate settling velocities of  $0.36 \times 10^{-3}$  to  $8.3 \times 10^{-3}\text{m/s}$ , Larsen(1977).

### 2.3 Flow Field Characteristics of Settling Tanks

In an effort to try and resolve the flow field characteristics found in settling tanks, Larsen (1977) carried out 22 experiments on 10 rectangular secondary settling tanks found in Sweden. He measured velocity with an Ultrasonic velocity probe, solids concentration was measured by taking samples at various tank depths. More recently, Ueberl(1995) conducted measurements of velocity and concentration profiles on the Limmattal rectangular final settling tank in Sweden. Velocity and concentration profiles were measured for a variety of inlet and outlet configurations with different inlet velocities and concentrations. Other full scale studies are outlined in sections 2.6.2 and 2.7.

The findings of these studies provide an insight into the hydrodynamics of settling tanks. The presence of a dispersed phase concentration of a higher value in the inlet flume than in the bulk flow causes the influent to plunge to the floor of the tank, the so-called ‘density waterfall’. This plunged flow runs along the bottom of the tank as a density current, Figure 2.3, in many cases for practically its entire length. Velocities in this current can reach up to ten

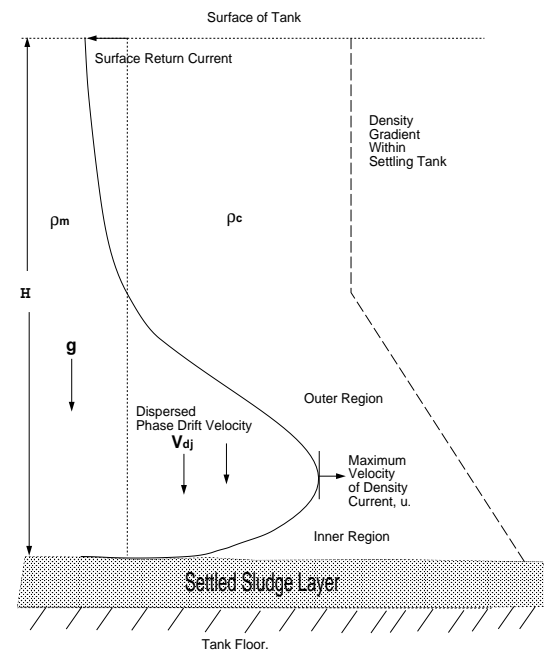


Figure 2.3: Schematic of a Density Current within a Settling Tank.

times the nominal tank through-flow velocity.

By ignoring viscous forces and equating the potential energy of the density difference between the lighter and heavier fluid,  $\Delta\rho g H$ , to the kinetic energy of the density current,  $\frac{1}{2}\rho_m u^2$ , Figure 2.3, it is possible to derive a 1-D relationship

for the velocity of the density current;

$$u = C \sqrt{\frac{\Delta\rho}{\rho_m} g H} \quad (2.1)$$

where  $C$  is a coefficient whose value depends on the local conditions, i.e. it may not be constant,  $u$  = density current velocity,  $H$  = depth of fluid in the tank,  $g$  = acceleration due to gravity,  $\Delta\rho$  = density difference between the fluids,  $\rho_m$  = density of the influent mixture. These quantities are shown in Figure 2.3. This relationship is used to determine the density of activated sludge in lock exchange experiments. Lock exchange experiments are discussed more fully in Chapter 6, where a numerical simulation is also carried out.

Most of the sedimentation into the settled sludge layer or blanket takes place from the density current. This settled sludge layer covers the tank floor for most of its length, it can be up 0.5m deep in places with solids concentrations of 10,000 to 15,000mg/l, Larsen(1977). In a situation with a predominantly uniform flow field across the width of the tank, the settled sludge layer should also be of uniform depth across the tank width. The layer is non-Newtonian in character and exhibits thixotropic properties, i.e. it shows evidence of a continuous solid phase that can resist deformation.

In the final third of the tank the current dissipates, the velocity profile changes from the distinct ‘jetting’ shape of Figure 2.3 to a more uniform ‘streaming’ velocity profile. The dissipation is brought about by deposition, viscous forces and turbulent mixing.

The density current induces recirculation in the upper part of the tank, this may consist of a single or multiple eddies extending over the entire tank length, see Figure 2.1. Dispersed phase concentration is low in this region. Flow at the surface is thus directed to towards the inlet. Flow at or near the inlet tends to be highly 3D in character. In a well designed tank, the flow field is predominantly 2D in character down stream of the inlet.

Although through flow velocities are low the tank is large, resulting in tank

Reynolds numbers in the turbulent range. In Larsen's study, Re was in the range 8,000 to 45,000, based on tank flow through velocity. Local Reynolds numbers based on density current velocities are in the region 36,000 to 131,000. However, the assumption of turbulent conditions based on Reynolds number alone does not take into account the effect of density stratification, i.e the effects of damping turbulence by the dispersed phase, Rodi(1979); as well as pockets of fluid with low velocities, e.g in corners at the tank floor, where the flow field may not always be turbulent. These effects need to be borne in mind when considering an appropriate turbulence model as will be done in Chapter 4.

Flow regimes where buoyancy effects are important should be judged not simply in terms of inlet concentration but in terms of the dimensionless parameters of Richardson and Froude number according to Lyn, Stamou, Rodi (1992). In density stratified flow the eddy viscosity depends on the stratification. This dependence is frequently related to the Richardson number which expressed as the ratio of buoyancy to kinetic energy. With high values of the Richardson number, i.e where buoyancy dominates over kinetic energy, the turbulence is suppressed and thus the turbulent exchange coefficients are reduced, Larsen(1975). Richardson number  $Ri_H$ , is given as;

$$Ri_H = \frac{g\gamma C_o H}{U^2} \quad (2.2)$$

where  $g$  = gravitational constant,  $\gamma$  = the proportionality constant relating density to concentration differences,  $H$  = tank depth,  $U$  = nominal tank velocity and  $C_o$  = inlet concentration.

The densimetric Froude number at the inlet is given by;

$$F = \left[ \frac{u_0^2}{gH_{in} \frac{\rho_m - \rho}{\rho}} \right]^{1/2} \quad (2.3)$$

where  $H_{in}$  = inlet depth,  $u_0$  = inlet velocity,  $\rho_m$  = local mixture density.  $\rho$  = the density of water. For full scale settling tanks, densimetric Froude numbers are

of the order of  $10^{-4}$ , Stamou(1988).

In non-buoyant flows the overall Froude number,  $F_R = u^2/gR$ , where  $R$  = half depth of the tank, is descriptive of the distortion of the free surface as well as the importance of the distortion of the free surface in determining the characteristics of the flow field. Free surface distortion is not simulated in the computational model used in this study. In settling tanks free surface effects are only considered to be important when wind shear creates surface waves. The experiments used for the numerical simulations in this study were considered to have been conducted in the absence of wind shear.

## 2.4 Settling Velocity

In order to understand settling tank hydrodynamics, we need to know the settling velocity of the dispersed phase. In addition, the accurate prescription of this settling velocity is an important parameter in the numerical simulation of settling tank performance. The drift flux model, Chapter 3, used in the numerical simulations for this research Chapters 6 and 7, requires the velocity of the dispersed phase relative to the mixture centre of volume to be proscribed, Ishii(1975). In this study we consider this velocity to be the settling velocity.

The settling velocity of individual activated sludge flocs within settling tanks does not lend itself readily to theoretical treatment, Miller(1964). This is because, as we have seen in section 2.1, the flocs are aggregates of primary particles and very irregular in composition, shape and size.

As floc concentration increases, the flow field around any one particle is affected its neighbours. The particles begin to restrict the area through which the displaced liquid flows upwards; the velocity of this liquid will increase, and the particles settle at a lower velocity. This is known as hindered settling, Bond(1959).

In many cases at a given concentration, most or all of the particles will

fall together at a constant rate irrespective of size, Davies(1976). The settling velocity here is less than that of the fastest individual particle in the suspension.

As we shall see in section 2.4.2, when particles fall at this constant rate a clear solid/liquid interface forms between the settling particles and the clear fluid above, see Figure 2.5, and it is this settling speed which is used in this research as the settling velocity.

When the flocs finally reach the settled bed region of the settling tank, they form a dense fluid mud layer with strongly non - Newtonian rheological properties, these properties are discussed in section 2.5. Due to continuing deposition, the sediment layer, which initially was a loose fragile structure, gradually collapses under its increasing weight. The interstitial pore water is expelled; the weight of the sludge layer is progressively supported by the inter-particle reaction forces. This process is called self - weight consolidation, Teison et al. (1993).

In the next section we will look at the settling of an individual particle in an infinite medium, following which we shall examine hindered settling of suspensions.

#### 2.4.1 Settling of a Single Floc

Under the influence of gravity, any single particle in an infinite medium having a density greater than that of the medium will settle with increasing speed until the buoyancy force equals the drag force on the particle or floc. Thereafter, the settling velocity will be essentially constant and will depend upon the size, shape and density of the particle. This velocity is known as the terminal velocity,  $V_o$ , for spherical particles we have;

$$\frac{\pi d^3}{6} (\rho_d - \rho_c) g = C_D \frac{1}{2} V_o^2 \frac{\pi d^2}{4} \rho_c \quad (2.4)$$

where  $d$  is the diameter of the particle and  $C_D$  is the drag coefficient. The drag coefficient is defined as the ratio of the drag forces to the dynamic pressure on the particle cross sectional area. It has the form;

$$C_D = \frac{F}{\frac{1}{2} \rho u^2 A_p} \quad (2.5)$$

Where  $F$  is the force of resistance exerted on the solid body by the suspending fluid flowing around it and  $A_p$  is the projected area of the body on the plane normal to the flow direction, Gupta(1983).

The drag coefficient varies with the particle Reynolds number,  $Re_p$ , which characterises the flow regime around the particle. It is given by;

$$Re_p = \frac{\rho_c |\hat{\mathbf{u}} - \mathbf{u}_d| d}{\mu_m} \quad (2.6)$$

Here  $d$  is the effective particle diameter, this is the diameter of a sphere with the same cross sectional area normal to the settling direction as the particle.

The mixture viscosity is given by  $\mu_m$  and  $|\hat{\mathbf{u}} - \mathbf{u}_d|$  is the relative velocity between the particle and the continuous phase. For activated sludge settling velocities,  $Re_p$  is less than 2.0, which should always place the process within the realm of Stokes law. The drag coefficient for this regime is given by

$$C_d = \frac{24}{Re_p} \quad (2.7)$$

and the settling velocity is, by rearrangement of equation 2.4, therefore;

$$V_o = \frac{gd^2}{18\mu} (\rho_d - \rho_c) \quad (2.8)$$

With the assumption of sludge flocs being spherical, substitution of typical values of activated sludge density, and floc diameter into equation 2.8 give large over predictions in settling velocity. Sludge flocs are generally not spherical and the settling velocity is affected by the settling orientation of the flocs. The drag force depends on the floc area facing the settling direction, whereas the effective gravitational forces only depend on the volume, Li (1987). Consequently, equation 2.4 over predicts settling because the surface area normal

to the settling direction of any given floc may be far larger than the surface area of a sphere containing the same mass at the same density as the floc.

Floc orientation also effects the settling direction. If a flat, disc, or needle shaped particle starts settling down in an orientation with the longest dimension neither parallel nor perpendicular to the vertical direction, the particle path would have horizontal components, reducing settling velocity.

Li and Ganczarczyk (1987), used a multi-exposure photographic method for the combined measurement of the terminal settling velocity and size of, effectively, individual activated sludge flocs. Two settling velocity / floc size relationships were derived, correlated by the experiment. One, equation 2.9, relates the floc settling velocity,  $V_o$  to the cross sectional diameter, L. This diameter was calculated from the floc area perpendicular to the settling direction, all dimensions being in mm;

$$V_o = 0.35 + 1.77L \quad (2.9)$$

The other relates floc settling velocity to the longest dimension, D;

$$V_o = 0.33 + 1.28D \quad (2.10)$$

The latter relation gives a settling velocity of  $1.6 \times 10^{-3} \text{ m/s}$  for  $D = 1.0 \text{ mm}$ , well within the range found by Larsen(1977).

The density of the dispersed phase was given as  $1300 \text{ kg/m}^3$ , no data on the aspect ratio of the flocs was available. Hence, using this density and assuming that the flocs were spherical and of diameter L, the settling velocity and particle Reynolds number can be obtained for a given diameter in the experimental range. Substitution of the density, diameter and settling velocity into equation 2.4, enabled  $C_d$  to be calculated for a given  $Re_p$ . The following drag law formula was derived from curve fitting the resulting graph.

$$C_d = 1702.9 - 1270.9Re_p + 494.14Re_p^2 \quad (2.11)$$

This function plotted is plotted in Figure 2.4, along with the curve representing equation 2.7.

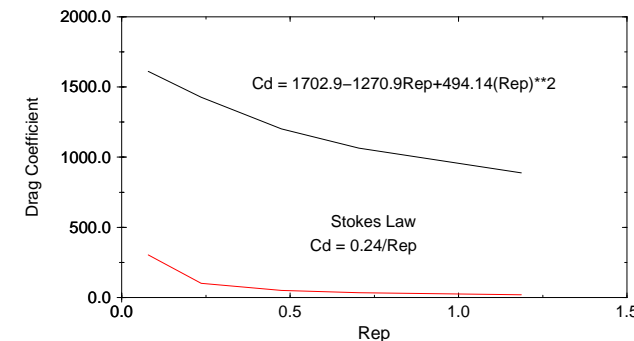


Figure 2.4: Variation of Drag Coefficient with Rep for a Single Floc. Settling Velocity from Li (1987)

## 2.4.2 Hindered Settling

As floc concentration increases, the flow field around any one particle is affected by its neighbours. Streamlines of the continuous phase flowing around individual particles begin to overlap, increasing drag. This is known as hindered settling, Bond(1959). Particle collisions may also take place, further affecting settling velocity.

In addition to hindered settling, activated sludge suspensions tend undergo a process known as flocculation. Here, the primary particles stick together increasing in size until well defined flocs form in the suspension. These flocs agglomerate to form larger units. This process results in an overall increase in solids removal from suspension as small particles adhere together and settle. However, up to a floc size of  $200 \mu\text{m}$ , this process results in a decrease in floc density, and hence an increase in floc porosity, caused by the increas-

ingly large amounts of water being trapped in the floc, Li(1987). Above this size, floc porosity changes more slowly. Consequently, the prescription of settling velocity is complicated still further over that for hindered settling due to these changes in floc density. In this study the effects of flocculation are not modelled, however, as we shall see, some of the effects of flocculation are incorporated into the prescription of settling velocity derived from batch the settling experiments Dahl(1993) used in this study.

Many hindered settling velocity relationships for the settling of suspensions have been proposed, Barnea (1973). They consists of, essentially, the terminal settling velocity of a single particle modified by some function of solids fraction introduced to take into account the increase in drag forces, Landman (1992). The Richardson and Zaki (1954) formulae, equation 2.12, has been used to describe settling of particulate slurries and dispersions;

$$V_s = \frac{2d^2g(1 - \alpha)^n(\rho_d - \rho_c)}{9\mu_c} \quad (2.12)$$

where  $\alpha$  is the solids fraction and  $n$  has a value of 4.65 to 5.25 depending on particle size. In activated sludge suspensions, there is a wide distribution of particle sizes hence a single value of  $d$  can not be used. Aside from this, this formulae does not produce the very rapid decay in settling velocity with concentration usually associated with activated sludge suspensions, illustrated in Figure 2.5.

The most commonly used method for determining activated sludge settling velocity as a function of concentration is from data gathered in batch settling experiments, Ramalho (1983). Consider a suspension with an initial uniform sludge concentration  $C$  mg/l placed in a settling cylinder, Figure 2.5a. As the sludge settles out interface (1) is established between the surface of the blanket of settled sludge and the clarified liquid above, Figure 2.5b. The zone directly below the clarified liquid is known as the interfacial zone and it has a uniform concentration. The interface settles at a velocity  $V_s$  which is considered to

be the sludge settling velocity. Simultaneously with the formation of the top interface a compaction zone is formed. Interface 2 defines the upper limit of this compaction zone which rises with constant velocity  $V$ .

Between the interface and the compaction zones is the transition zone. Settling velocity decreases due to an increase in the viscosity and density of the suspension as well as upward flowing water due to displacement by the dispersed phase. In this zone the sludge changes gradually in concentration from that of the interfacial zone to that of the compaction zone.

In Figure 2.5c, interface 1, moving downwards meets interface 2 moving upwards at a critical time  $t_c$ . At this point the transition zone fades away. The settled sludge exhibits a uniform concentration,  $X_c$ , called the critical concentration. From this point compaction starts and sludge begins to thicken eventually reaching an ultimate concentration  $X_u$ .

Plotting settling height against time reveals a section of the curve in the early stages of the experiment which is essentially a straight line. The gradient of this straight line is the zone settling velocity, ZSV, and it corresponds to the velocity at which the suspension settles prior to reaching the critical concentration  $X_c$ .

The experiment is repeated for different initial concentrations  $C$ , leading to a family of settling curves. The values of ZSV are obtained by drawing a tangent to the initial, straight line part of the cure as described above. The the values of ZSV at each different initial concentration are then plotted on a single curve. A curve fit to this data will give an expression for the settling velocity in the experimental concentration range. The effects of flocculation by differential settling, that is fast-settling particles colliding with and adhering to more slowly settling particles, is included in settling velocity measurements by this method. The expression derived by the above experiment has the general

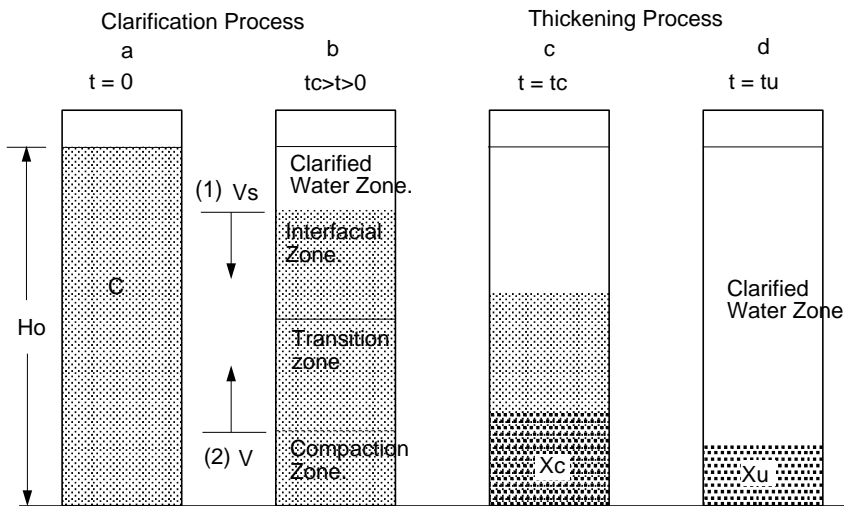


Figure 2.5: Stages in Batch Settling Experiment.

form, Takacs et al.(1991);

$$V_s = V_o e^{(-kC)} \quad (2.13)$$

where  $V_o$  is the settling velocity of a single particle in an infinite quiescent medium and  $k$  = an empirical coefficient ( generally  $k \approx 0.0005$  ). The solids concentration  $C$ , is in mg/l, and can also be expressed in terms of solids fraction  $\alpha$  and dispersed phase density  $\rho_d$ , i.e  $C = 1000.\alpha\rho_d$ .

The numerical simulations undertaken in this report used a variation of equation 2.13 with the base 10 being used for the exponential instead of the natural logarithm, e. The reason for this, expanded in Chapter 6, is that a closer curve fit was obtained against the published settling velocity / concentration data, Dahl (1993). The resulting formulae has the form;

$$V_s = V_o 10^{(-k\alpha)} \quad (2.14)$$

Where  $V_o = -2.198.10^{-3}m/s$  and  $k$  has a value 285.84 for an inlet solids

fraction of 0.002. This is similar to a formulae derived by Hultman et al. (1971) and published in Larsen (1977).

For batch settling with a range of particles of non-uniform size, Takacs et al.(1991), identified 3 regimes namely; solids in suspension which will not settle due to their loose aggregate structure, these may have a concentration of a few mg/l. Highly settleable fractions with concentrations in the range 100-500 mg/l and slowly settleable solids with concentrations greater than 500mg/l. Categorizing suspended solids concentration in this way leads to a modification of equation 2.13 and gives rise to a double exponential formulae;

$$V_s = V_o [e^{-k(C-C_{min})} - e^{-k_1(C-C_{min})}] \quad (2.15)$$

where  $C_{min}$  is the upper concentration of non settling flocs and  $k_1$  is a settling exponent for poorly-settling particles, typically 0.015. A graph plot of the exponential formulae and the experimentally derived settling velocity formulae is illustrated in Figure 2.6.

Zhou and McCorquodale (1992) compared both exponential settling velocity formulations in a 2D computational comparison of velocity and concentration data gathered at the San Jose Creek Water Reclamation Secondary Clarifier (Dittmar et al. 1987). The components of the calculation model consisted of a buoyancy modified momentum equation, the standard  $k - \epsilon$  turbulence model and a convection diffusion equation for the concentration of suspended solids, section 2.6.

The comparison revealed that with the prediction of settling velocity by the double exponential formulae, equation 2.15, the concentration profiles in the density current near the inlet were marginal closer to experimental results than the single exponential formulae. The main difference between the results, however, occurred downstream from the inlet in the ambient fluid above the density current. Here, the single exponential equation showed a concentration of zero against the measured concentration of 7 to 32 mg/l. The double

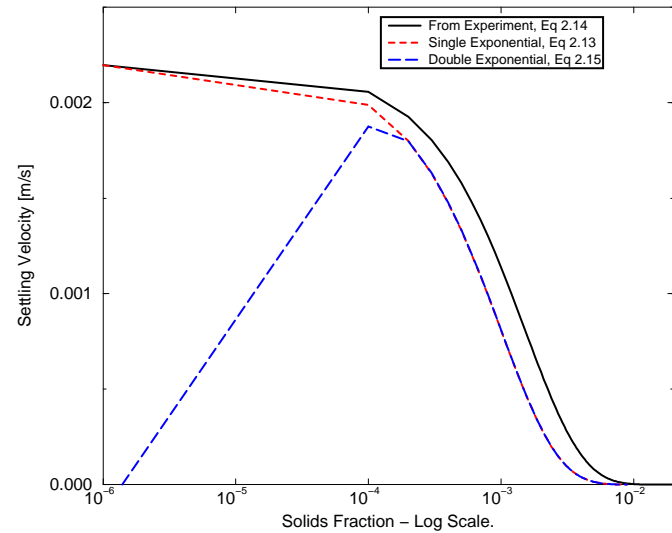


Figure 2.6: Settling Velocity versus Solids Fraction.

exponential formulae showed concentrations in the range 9 to 63 mg/l.

## 2.5 Activated Sludge Rheology.

The addition of solid particles to a fluid will affect apparent the viscosity of the resultant suspension. A summary of the types of rheological behaviour observed for sewage sludges by different authors was compiled by Casey (1983). Below a solids concentration of about 4% by weight most sludges exhibit Newtonian fluid behaviour, that is a linear relationship exists between shear stress and shear rate where the constant of proportionality,  $\mu$ , is the viscosity of the fluid, i.e water. Above this concentration most sewage sludges have been characterised as exhibiting either plastic or pseudo-plastic behaviour, Dick (1967), that is they are part of a class known as shear-thinning fluids. They may or may not possess an initial characteristic yield stress.

Of those sludges that possess a definite yield stress, the rheology is further

complicated by the fact that these sludges are also thixotropic, that is they possess an internal structure which breaks down as a function of time and shear rate.

A typical rheogram for sewage sludge exhibiting Bingham plastic behaviour, that is possessing a definite yield stress, is illustrated in Figure 2.4. This model was considered to be most appropriate for activated sludge Dick(1967). The

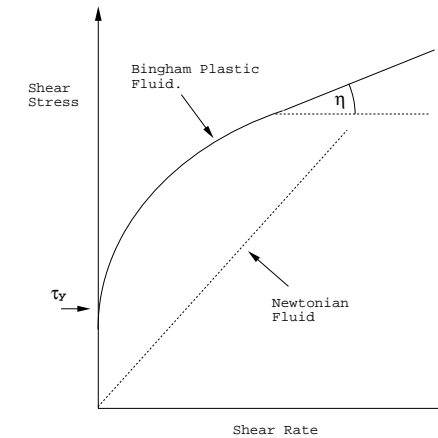


Figure 2.7: Activated Sludge Rheogram, adapted from Toorman(1992).

curve can be interpreted as follows;

- 1) The behaviour is not Newtonian since the rheogram is not a straight line.
- 2) The curve does not start at zero on the shear stress axis. A minimum shear stress needs to be exerted in order to initiate deformation of the fluid. The flow threshold or yield stress,  $\tau_y$ , is related to the structure of the sludge which consists of aggregates of primary particles, Casey (1983). The aggregates at this stage are sufficiently close together to form a continuous three dimensional network which has to be broken down in order for flow to occur.
- 3) The slope of the curve, equivalent to the apparent viscosity, is not con-

stant but decreases gradually with increasing shear stress. This variation indicates the structural modification of the suspension under the action of increasing shear stress.

The completion of aggregate breakdown with increasing shear is indicated by a constant apparent viscosity corresponding to the final linear section of the curve, the gradient of this linear section is the ‘plastic viscosity’,  $\eta$ , Casey (1983). The magnitude of  $\tau_y$  and  $\eta$  are void fraction dependent, the relationship between solids fraction,  $\tau_y$  and  $\eta$  for the sludges under consideration in this study are given in Chapters 6 and 7. The intensity of the forces of attraction between primary particles is the chief factor affecting the magnitude of the yield stress and the deformation rate at a given void fraction.

Bingham Plastic fluids are the limiting case of class of shear thinning fluids whose constitutive equation has the general form;

$$\tau_{ij} = \tau_y + K\dot{\gamma}_{ij}^n \quad (2.16)$$

Where  $\tau_{ij}$  is the stress tensor and  $\dot{\gamma}_{ij}^n$  stands for the rate of strain tensor. When the power-law index  $n = 1$ , and  $K = \eta$  then we have the Bingham model.

In using this model for activated sludge, it is assumed that the mixture is non-viscoelastic. Data on the relaxation time, which governs the degree of viscoelasticity a fluid may exhibit, is scarce for activated sludge. It is generally assumed, however, that viscoelasticity has little influence on the flow field in the main body of a settling tank.

In the case of an activated sludge mixture exhibiting Bingham fluid properties, the effective laminar mixture viscosity can be written as, Vradis and Hammad(1995);

$$\mu = \frac{\tau_y}{\sqrt{\dot{\gamma}_{ij}\dot{\gamma}_{ji}}} + \eta \quad (2.17)$$

if  $\sqrt{\dot{\gamma}_{ij}\dot{\gamma}_{ji}} > \tau_y$

$$\text{else } \mu = \infty \quad (2.18)$$

$$\text{if } \dot{\gamma} < \tau_y$$

This value is added to the viscosity of the carrier fluid, in this case water. For the resultant mixture viscosity to be a scalar function of the rate of strain tensor  $\dot{\gamma}$  it must be dependent only on the invariants of  $\dot{\gamma}$ . The invariants - signified as  $I_1$ ,  $I_2$  and  $I_3$  respectively - are those special combinations of the components of  $\dot{\gamma}$  that transform as scalars under a rotation of the coordinate system, Bird et al. (1987). They are formed by taking the trace, i.e summing the diagonal elements of  $\dot{\gamma}_{ij}$ ,  $\dot{\gamma}_{ij}^2$ , and  $\dot{\gamma}_{ij}^3$ . They are defined as;

$$\begin{cases} I_1 = \text{tr } \dot{\gamma} = \dot{\gamma}_{ii} \\ I_2 = \text{tr } \dot{\gamma}^2 = \dot{\gamma}_{ij}\dot{\gamma}_{ji} \\ I_3 = \text{tr } \dot{\gamma}^3 = \dot{\gamma}_{ij}\dot{\gamma}_{jk}\dot{\gamma}_{ki} \end{cases} \quad (2.19)$$

The first invariant can easily be shown to be  $2(\nabla \mathbf{u})$  which is zero for an incompressible fluid. For viscometric flows the third invariant is assumed to be unimportant, largely because of a lack of experimental information, which leaves only the second invariant,  $I_2$ . In Cartesian coordinates the second invariant is defined as;

$$I_2 = 2 \left[ \left( \frac{\partial \mathbf{u}}{\partial x} \right)^2 + \left( \frac{\partial \mathbf{v}}{\partial y} \right)^2 + \left( \frac{\partial \mathbf{w}}{\partial z} \right)^2 \right] + \left[ \frac{\partial \mathbf{v}}{\partial x} + \frac{\partial \mathbf{u}}{\partial y} \right]^2 + \left[ \frac{\partial \mathbf{w}}{\partial y} + \frac{\partial \mathbf{v}}{\partial z} \right]^2 + \left[ \frac{\partial \mathbf{u}}{\partial z} + \frac{\partial \mathbf{w}}{\partial x} \right]^2 \quad (2.20)$$

Using a shear-rate-dependent laminar viscosity in the momentum equations to simulate Bingham plastic rheology has been successfully tried in a number of studies, namely by; O'Donovan and Tanner (1984), for a numerical study of the Bingham squeeze film problem, Vradis and Hammad (1995) for heat transfer in flows of Bingham fluids. Of more direct relevance, Toorman and Berlamont (1992) used the above method to model the transport of estuarial mud, a cohesive sediment which exhibits similar properties to activated sludge. In their simulation a settled mud layer, or bed, was withdrawn through a

suction bell, no comparison with experimental data was made. Dahl(1993) used this approach to simulate the behaviour of activated sludge in a large scale experimental tank, comparison with bed height revealed good agreement with experimental data. Lakehal et al. (1999), also used this approach in the 2D simulation of a full-scale cylindrical tank, no comparison was made with experimental data.

It is in the settled bed region within the settling tank that the effects of the Bingham rheology are most pronounced and the ability of the model to simulate bed depth and resistance to shear most severely tested. However, it should be born in mind that most of the fluid in the tank has some degree of Non-Newtonian behaviour and as illustrated in Chapter 7, Bingham effects can dominate the flow field in the hopper region. Hence, the ability of the model to simulate the correct rheological behaviour of the fluid throughout the tank is important in determining the correct flow field.

We have seen in section 2.4 that the settled bed is initially a loose fragile structure. It gradually collapses under the increasing weight of sediment being deposited from the density current.

This bed structure can break up under shear forces (liquefaction) or increased pore water pressures (fluidisation). Further information on the behaviour of settled beds is given below in section 2.5.1.

### 2.5.1 Bed Form Development

Sediments tends to be classified into two groups; cohesive, the type found in settling tanks, and non - cohesive. Most research has focused on non - cohesive sediment transport, accumulation and resuspension; Celik and Rodi (1988), Fredose (1993) and Rampall and Leighton(1994) give an indication of the diversity of work carried out in this field.

The near-bed region or bed load layer, that is that part of the sediment in

continuous contact with the bed while still in suspension, has previously been modelled in settling tanks using non-cohesive sediment entrainment models by Zhou and McCorquodale (1992), and Lyn et al. (1992). Cohesive sediment accumulation, section 2.5, has been simulated by Dahl (1993) and Lakehal (1999). However, modelling the behaviour of activated sludge as a non - cohesive sediment makes two assumptions which are incompatible with cohesive sediment transport in the near bed region;

**1)** In non-cohesive sediment transport, deposition and erosion are assumed to be in equilibrium for a given bed shear stress, Lick(1982). Further it is assumed that the near-bed region will re-entrain from a settled bed until its maximum carrying capacity is reached. Experiments carried out by Mehta and Partheniades(1975) and Lau et al. (1994) on cohesive sediment led them to postulate that only those flocs strong enough to settle through the region of high shear near the bed are deposited and these flocs bond to the bed, no re-entrainment occurs until shear stress increases. Other flocs are broken up and returned to the main flow.

**2)** Modelling re-entrainment of non-cohesive sediment relies on the use of an ‘ effective diffusivity ’ brought about by interparticle interactions on and just above the bed. In turbulent flows this ‘ effective diffusivity ’ is dependent on turbulent fluctuations in the boundary layer above the bed impressing themselves through the laminar sub-layer in contact with the bed. This in turn creates a local increase in applied shear stress above the mean value causing settled particles to be ejected into the boundary layer region.

Experimental and theoretical work has been carried out on the subject of effective diffusivity by Rampall and Leighton (1994), Chapman and Leighton(1991) and Zhang and Acrivos(1994), amongst others. This method of resuspension relies on the sediment being composed of individual particles. This is not the case with activated sludge as the individual particles are effectively bonded to the bed. So, provided the combined mean stress and stress due to turbulent

fluctuations is less than the yield stress no re-entrainment will take place. More specifically, it implies that re-entrainment from cohesive sediments is *largely independent of turbulent intensity in the mean flow*, given the above proviso.

The present contribution does not seek to model the flow regime above the settled bed with a prescribed boundary boundary layer formulation. The heavy concentration of sediment in the density current above the bed alters the boundary layer structure producing a deep laminar sub-layer. The bed surface can be considered to behave as a porous medium with interstitial water being expelled from the surface due to consolidation within the settled layer.

Three methods of erosion of cohesive sediment have been identified according to the magnitude of the bed shear stress and the nature of the deposit, Mehta et al. (1989) and Teisson et al. (1993). They are for increasing shear stress;

**1)** Aggregate by aggregate erosion of the bed, in which increasing shear stress causes undulations appear which are gradually accentuated, deforming the sediment layer. The sediment is carried away in the form of streaks and diluted in the free stream.

**2)** Surface erosion; here the eroded surface creases and the surface is torn. Erosion takes the form of flakes which are more or less diluted in the free stream.

**3)** Mass erosion of fully consolidated beds in which the bed fails at some plane below the surface and clumps of material are eroded.

It has been noted, Larsen(1977), that a certain amount of ‘armouring’ or conditioning of the bed takes place that is, for a given shear stress surface erosion will occur and then stop. For further erosion to take place a net increase in shear stress is required.

There is no established theory for calculating the rate of erosion,  $\epsilon$ , of cohesive sediments according to Teisson et al. (1993), however, a number of empirical laws have been suggested. Mehta et al(1989), proposed the following

relationship for surface erosion;

$$\epsilon = \alpha_1 \frac{\tau - \tau_y}{\tau_y} \quad (2.21)$$

where  $\alpha_1$  is a constant,  $\tau$  is the shear stress at the bed and  $\tau_y$  is the critical shear stress of the bed.

By considering the floc erosion rate  $\epsilon_f$ , Parchure and Mehta (1985) have proposed the following expression for the mass erosion of partially-consolidated beds;

$$\epsilon = \epsilon_f^{\alpha_2(\tau - \tau_y)^b} \quad (2.22)$$

where  $\alpha_2$  and b are empirical constants.

These relationships are not used in the numerical simulations presented in this report. Deposition and erosion of the settled bed were not the main subject of the experimental investigations used to test the numerical model, so detailed data on these processes was not available. It was found that by correctly specifying  $\tau_y$  from the exponential relationship given in equation 6.3, the settled bed reached an acceptable height for the shear stress imposed by the density current.

## 2.6 Previous Models of Settling Tank Performance

### 2.6.1 Single Phase Computational Models

Single phase flow models are primarily concerned with predicting settling tank hydrodynamics. Schamber and Larock (1981) used a 2D finite element method to solve the equations of continuity and momentum together with a k- $\epsilon$  turbulence model in order to simulate the flow field of an idealised settling tank 12.2m long, 4.6m wide with an inlet depth of 3m and an outlet end depth of

2.7m. The tank had a single surface inlet and surface outlet. The  $k-\epsilon$  turbulence model was used on the premise that the flow in the tank is fully turbulent with settling tank Reynolds numbers in the range 17,000 to 170,000. Turbulence intensities were considered to be 10 to 20 percent of the mean values of velocity. No comparison with experimental data was made, thought vector plots of the flow field - which contained a single large eddy - were considered to be physically realistic. The most pronounced changes in turbulent viscosity occurred at the inlet and exit regions where velocity gradients are largest.

Celik et al. (1985) showed the suitability of numerical finite-volume methods for predicting the hydrodynamic and mixing characteristics of settling tanks. The model consisted of the two-dimensional Reynolds-averaged incompressible continuity and Navier-Stokes equations without buoyancy terms, together with the standard  $k-\epsilon$  turbulence model. Comparisons with velocity data gathered on a relatively simple laboratory scale tank with a single submerged inlet and a surface outlet, the Windsor experiment Imam et al.(1983), showed good agreement. The flow field in the tank is relatively simple with a single recirculation zone, the length of this recirculation zone was underpredicted by about 20%, under predictions of recirculation zone length is a common feature of the standard  $k-\epsilon$  turbulence model.

Adams and Rodi(1990) applied the same numerical model to a laboratory scale tank with velocity and turbulent intensity data gathered by Adams and Stamou(1988) at Karlsruhe. The tank had a submerged slot inlet which could be adjusted to different depths below the surface. This inlet arrangement produced a more complicated flow field with two recirculation zones. The larger recirculation zone occupied the region from the bottom of the inlet to the tank floor, the smaller of the two occupied the region from the top of the inlet to the free surface. This particular flow pattern exists for the ratio of the height of the slot centre to tank depth equal to 0.588. It was found that the recirculation zone length was under-predicted. As a result, the total area occupied by the

recirculation zones is approximately 20% less in the computation than in the experiment. This under prediction showed itself in comparisons of velocity data with the simulation showing that the reverse flow at the end of the recirculation zones declines too quickly. That aside, comparisons of velocity were good. Comparisons of turbulent intensity showed good quantitative agreement with the general evolution and distribution of the  $k$  field. The highest turbulence levels were found in the shear layers bordering the recirculation zones, Adams and Rodi(1990). The turbulence generated in these layers is swept downstream and also partially entrained into the recirculation zones and diffused towards the free surface. Beyond reattachment, the turbulence level drops quickly due to the absence of any significant velocity gradients.

In order to obtain information about the flow field and the turbulent exchange coefficients (the eddy diffusivity), a “Flow Through Curve”, (FTC), can be plotted. An FTC represents the time response at the outlet of a tank to a tracer pulse at the inlet and is commonly used to evaluate the hydraulic efficiency of settling tanks. This can be calculated by solving the unsteady tracer concentration convection / diffusion equation;

$$\frac{\partial C}{\partial t} + \nabla \cdot (uC) = \nabla \cdot \Gamma \nabla C \quad (2.23)$$

where  $C$  = dye concentration and  $\Gamma$  = diffusion coefficient.

This transient calculation was solved using both a hybrid scheme and the QUICK scheme and the results compared to experiment. Both schemes reproduced the FTC curve well with the QUICK scheme tending to over predict the peak concentration at the outlet by about 20%.

As indicated above, the main failure in the prediction of flow field behaviour in tanks with single phase flow is in the calculation of the length of the recirculation zones. The standard  $k-\epsilon$  model can not account adequately for the effect of streamwise curvature on the turbulence, Adams and Rodi (1990). Streamwise curvature, caused by the presence of large recirculation zones, is

a common feature of settling tank hydrodynamics. Stamou(1990) used a  $k-\epsilon$  model modified to include the effects of streamline curvature to predict the flow field and FTC on the Karlsruhe basin at Re 2500, velocity and FTC data gathered by Stamou.

The length of the long, tank floor recirculation zone was found to be predicted to within 7 percent of the measured value, a marked improvement on previous predictions with the standard  $k-\epsilon$  model. For the upper recirculation zone, the length was 50 - 67% of the experimental value, identical to predictions with the standard  $k-\epsilon$  model. Comparisons with velocity profiles taken in this region showed higher negative velocities in the upper recirculation zone. At all other measuring stations velocity comparisons were very satisfactory showing improvements over the std  $k-\epsilon$  model. Similarly, the FTC curve showed much closer correlation with the experimental results.

Turbulence intensity was not measured but comparison was made between the two turbulence models. Above the inlet  $k$ -production predicted by the standard model was very high. With the modified model, however, the very strong streamline curvature suppresses significantly the production of  $k$  and results in very small  $k$  values. Beyond re-attachment of the bottom recirculation region, the  $k$ -levels are rather low and uniform and very similar for both models, Stamou(1990).

In considering the usefulness of these single phase models it is necessary to ask how the significant features of the flow field change with an influent mixture heavier than the ambient fluid in the tank. In the studies above, the main area of interest in the flow field has been in the prediction of recirculation zones near the inlet and with accurate predictions of their length and the associated velocity field and turbulent intensity. Downstream of this recirculation region the flow field is essentially that found in an open channel.

As illustrated in section 2.3 the structure of the flow field in the inlet region is radically different in working tanks from the above. The large, tank

floor recirculation zone collapses and the region is dominated by the so called density waterfall. A density current with high velocity gradients dominates the lower part of the tank, associated with it is the density stratification of turbulence. Single phase simulations, which do not include buoyancy terms in the momentum equations and a means of transporting the dispersed phase, are incapable of reproducing these flow field features. This may be considered as the minimum requirement for simulating operational secondary settling tank hydrodynamics.

## 2.6.2 Dispersed Phase Transport Models

Schamber and Larock (1983) solved the equation governing the concentration field for a dilute suspension of spherical particles in circular or rectangular primary settling basins. In this kind of settling basin the influent dispersed phase concentration is too low, typically  $0.0002\text{kg/m}^3$ , to generate a density current, hence buoyancy effects do not need to be modelled. Their model assumed that for small particles settling in Stokes range, turbulent transport coefficients for the dispersed phase are approximately equal to turbulent diffusion coefficients of the fluid. Settled solids were presumed to be removed across the bottom boundary.

The particle concentration field was predicted by a convection diffusion equation, shown in equation 2.23, but with a sink term containing the particle settling velocity. The additional term has the form;

$$\frac{\partial V_s C}{\partial y} \quad (2.24)$$

Where  $V_s$  = dispersed phase settling velocity imposed in the vertical,  $y$ , direction. A fixed settling velocity for primary organic waste of  $0.00042\text{m/s}$  was used. The velocity field and turbulent exchange coefficients were predicted by the solution of the standard continuity, momentum and  $k-\epsilon$  equations. The numerical solution was achieved using the Galerkin finite element method.

The mathematical model was used to determine the velocity field and particle concentration for idealised 2D representations of a rectangular and circular settling basin. Vector plots showed that in both cases the flow field was dominated by a single recirculation zone that occupied practically the entire length of the tank. The computed flow patterns were shown to agree qualitatively with the available experimental data though no quantitative comparisons were made.

Stamou et al. (1989) also modelled the flow field behaviour of a primary settling tank, this one at the City of Sarnia, Ontario. Velocity and concentration data was gathered for this tank by Heinke (1977). The flow field in the tank was assumed to be steady, two dimensional and unaffected by density differences, sediment accumulation was not modelled. The Sarnia tank was rectangular 32.7m long, 9.0m wide and of average depth 2.7m. The original inlet consisted of four pipes distributed across the inlet end wall of the tank, set opposite the pipes were two baffles onto which the influent impinged. This arrangement was simplified for the purposes of the 2D simulation by assuming that the inlet baffle extended to the surface and across the full width, thus allowing no flow over or between the baffles. A uniform 2D flow field was assumed to emerge from under the idealised baffle and this was used as the inlet to the computational domain. The combination of outlet weirs was approximated as a simple overflow weir at the end of the settling zone within the tank.

The mathematical model consisted of a continuity equation, and a momentum equation which, because of the low dispersed phase of 150-200 mg/l, did not contain a buoyancy term. The standard  $k - \epsilon$  model was used to model turbulence. The suspended particles were assumed to be discrete and were divided into  $n$  groups of constant particle size, individual mass fraction  $f_i$  and associated settling velocity  $V_{si}$ . The distribution of each size category within

the flow field was given by;

$$\frac{\partial C_i}{\partial t} + \nabla \cdot u C_i = \nabla \cdot \Gamma \nabla C_i + \frac{\partial V_{si} C_i}{\partial y} \quad (2.25)$$

In this case the dispersed phase was divided into 6 size groups.

The boundary conditions assumed that there is no flux of suspended solids through the side walls, no resuspension from the bottom and that there is no transfer of solids across the free surface i.e.

$$\frac{\partial C_i}{\partial x} = 0 \quad \text{for vertical walls}$$

$$\frac{\partial C_i}{\partial y} = 0 \quad \text{for bottom walls}$$

$$\Gamma \frac{\partial C_i}{\partial y} + V_{si} C_i = 0 \quad \text{for the free surface} \quad (2.26)$$

Flow field calculations were made for three overflow rates; 30, 60 and 110m/d, corresponding to tank Re of 28200, 62000 and 95000 respectively. There was no significant effect of the overflow rate on the calculated flow field patterns. Comparison was made with velocity data gathered by Heinke (1977) at an overflow rate of 60m/d. The experimental data showed 3D behaviour, particularly near the inlet. The geometric approximations made for the simulation in this region meant that there was no flow over the top of the baffle, which there is in the full scale tank, so that a single large recirculation zone was generated behind the baffle in the simulation. This resulted in large differences between the measured and calculated velocities near the inlet. Downstream of the recirculation zone, the velocity predictions were in better agreement with (but consistently lower than) the measurements, the later still showing 3D behaviour.

Calculations of the suspended solids distribution were made for the three overflow rates with comparisons against experimental data being made for the 60m/d overflow rate. Using the experimentally given settling velocity for

each of the size fractions, good agreement was found with the recorded solids fraction field. Similarly, the removal efficiency, R, given by;

$$R = \frac{C_{in} - C_{out}}{C_{in}} \quad (2.27)$$

where  $C_{out}$  is the concentration at the outlet, was calculated as 77.8% compared with the experimentally determined value of 77.7%.

The effect of varying the turbulent Schmidt number  $\sigma_c$  in equation 2.25 on the removal efficiency was studied. It was found that increasing  $\sigma_c$  from 0.5 to 1.0, which represents a 100% increase in the level of turbulent diffusivity, led to a relatively small (1.2%) change in removal efficiency.

It was concluded that the assumptions of a uniform flow velocity and constant eddy viscosity used previously in simple hydrodynamic models of settling tank performance were invalid in most parts of the tank. The model predicted the removal efficiency of the tank very well but predictions of the velocity field could be improved by carrying out 3D calculations with a more physically realistic inlet geometry.

The existence of sediment-driven density currents is a distinguishing feature of secondary clarifiers, DeVantier and Larock (1986) modelled this feature by adopting the Boussinesq approximation in the momentum equation. With this approximation, the effects of density differences are neglected in the treatment of the inertial terms but included in the buoyancy force term. The resulting momentum equation has the form;

$$\frac{\partial \mathbf{u}}{\partial t} + \mathbf{u} \nabla \cdot \mathbf{u} = -\frac{1}{\rho} \nabla P + \nabla \cdot \Gamma \nabla \mathbf{u} + \left( \frac{\rho_s - \rho_f}{\rho_f} \right) g \quad (2.28)$$

Where  $\rho_s$  is the dispersed phase density,  $\rho_f$  is the continuous phase density.

The effect of buoyancy forces on turbulence was neglected and the standard  $k - \epsilon$  equation was used in the equation set. A convection diffusion equation, equation 2.23, with a sink term, equation 2.24, was used to model the transport and settling of activated sludge. The turbulent diffusivity of

the dispersed phase being set to 1.2 times the eddy viscosity, Cordoba-Molina(1979). Settling velocity was specified as a function of solids fraction from data supplied by Metcalf and Eddy (1979) and Larsen(1977), the latter velocity being approximately twice as large over the solids fraction range of interest. The exact equation used was not specified.

An idealised 2D section of a full scale circular clarifier with an inlet and outlet geometry similar to that found in Stamou et al. (1989), above, was simulated. The dimensions and through flow velocity were selected on the basis of standard criteria, Metcalf and Eddy (1979). Four inlet concentrations; 560mg/L, 840mg/L, 1,120mg/L and 1,400mg/L were used, though no dispersed phase density was specified.

Vector plots of velocity and contour lines of solids fraction concentration were presented. The flow field was seen to be dominated by a density current running almost the entire length of the tank above which a large recirculation eddy formed. Contour lines of solids fraction showed high levels in the density current and typically low values on the recirculation region. The predicted flow field behaviour for the basin was of the same magnitude and qualitative nature as that measured by Larsen(1977) in rectangular basins.

The model was tested for its sensitivity to the specified inflow values of  $k$  and  $\epsilon$ . Increasing influent values of  $k$  from 10% to 20% for the lowest inlet concentration case, did not significantly effect any of the turbulence parameters in the flow field.

It was concluded that the formation of a strong bottom density current and a free surface return current were correctly predicted, with the strength of the bottom current closely related to the inlet concentration, i.e increases in concentration resulted in higher maximum velocity in the density current.

Zhou and McCorquodale (1992) used a similar equation set to DeVantier and Larock (1986), above, to predict the velocity and concentration fields in the San Jose Creek Secondary clarifier, Dittmar et al.(1987), and the Jonkoping

and Tomelilla Clarifiers, Larsen(1977). A continuity equation and a buoyancy modified momentum equation, 2.28, were solved together with the standard  $k - \epsilon$  equation used to model turbulence.

A convection diffusion equation, equation 2.23, with a sink term, equation 2.24, was used to model the transport and settling of activated sludge. For the prescription of settling velocity, the single exponential formulae, equation 2.13, and the double exponential formulae, equation 2.15 were compared. These relationships, derived from batch settling experiments, enabled the hindered settling of the dispersed phase with increasing concentration to be modelled, section 2.4.2.

The San Jose Creek Clarifier is 30m long and 3m deep. It has a baffle in front of the inlet extending from the surface to about half the depth of the tank. The inlet concentration of suspended solids was 841mg/l with a sludge density of 1300kg/m<sup>3</sup>. The settling velocity of a single particle of sludge was reported as 30m/h. The Jonkoping Secondary Clarifier is 28.0m long and 3.0m deep. The inlet concentration was reported as 850mg/l with a dispersed phase density of 1360kg/m<sup>3</sup>. The Tomelilla Secondary Clarifier was 40.0m long and 1.8m deep. The inlet concentration was 2,200mg/l with a dispersed phase density of 1660kg/m<sup>3</sup>. The settling velocity of a single sludge particle was reported as 12m/h for both the latter studies.

Tank inlets were simplified to enable a 2D simulation to be carried out by replacing multiple inlets with a single slot that extended over the entire width of the tank. Sludge hoppers and the slope of the tank floor were not included in the computational domain.

The San Jose Creek Clarifier was simulated under neutral density conditions and compared with the simulation for the more dense influent. For the neutrally buoyant case, a recirculation zone is formed beneath the inlet. Downstream of this region, past the inlet baffle and in the main body of the tank, the velocity profile becomes similar to open channel flow. With the dense influent,

however, the inflow plunges directly to the tank floor, practically eliminating the recirculation zone found there in the neutrally buoyant case. Water from the main body of the tank was seen to be drawn under the inlet baffle and entrained into the plunging inflow. The model indicated that the presence of the baffle can reduce the level of entrainment and thus prevent the dilution of the dispersed phase in the influent. The flow field in the main body of the tank was dominated by the density current with a relatively high velocity surface return current.

Comparisons of concentration were good at all stations. At the tank floor, where no experimental data was gathered, the simulation showed very high values of concentration. These high values were also found in the numerical simulations of full scale tanks conducted in this research, Chapter 7. Zhou and McCorquodale compared the behaviour of the single and double exponential settling velocity formulations, they found that there was little difference in the overall concentration profiles, however, the double exponential formulation gave better predictions in the low concentration regions in the ambient fluid. This is hardly surprising as this model was formulated to take into account poorly settling solids that may remain in suspension.

Velocity and concentration profiles were compared against experiment for the Tomelilla settling tank. Again, the flow field for this tank is dominated by the density current flowing along the tank floor, comparison revealed that its maximum velocity was under predicted at a number of stations up to about half way along the tank. The 2D model could not simultaneously reproduce the observed bottom velocities and surface recirculation current, indicating that 3D effects were present. Concentration profiles were well predicted at all stations. Concentration profiles were also well predicted for the Jonkoping settling tank where no comparisons were made with velocity data.

Lyn, Stamou and Rodi (1992), carried out a 2D simulations the Alhmhut Tertiary Settling basin in Sweden and compared the results with velocity and

concentration data gathered by Larsen. The effects of buoyancy on turbulent energy and momentum balances were taken into account within the model.

In the simulation, the k equation of the turbulence model has the form;

$$\nabla \cdot (\rho \mathbf{u} k) = \nabla \cdot \left( \frac{\mu_t}{\sigma_t} \nabla k \right) + P_k - \rho \epsilon + R_{iH} \left( \frac{\mu_t}{\sigma_c} \right) \frac{\partial k}{\partial y} \quad (2.29)$$

with the  $\epsilon$  equation;

$$\nabla \cdot (\rho \mathbf{u} \epsilon) = \nabla \cdot \left( \frac{\mu_t}{\sigma_t} \nabla \epsilon \right) + C_1 \frac{\epsilon}{k} P_k - C_2 \rho \frac{\epsilon^2}{k} \quad (2.30)$$

$P_k$  is the production of k due to velocity gradients. The term  $R_{iH}$  is the Richardson number and is defined in equation 2.12. It reflects the effects of stratification on k and follows from the exact equation for k, where the influence of buoyancy is given by;

$$\frac{-g \rho' v'}{\rho_o} \quad (2.31)$$

where  $\rho'$  and  $v'$  are the fluctuating components of density and velocity and  $\rho_o$  is a reference density. This term and the more general effects of buoyancy stratification on turbulence are discussed more fully in Chapter 4. The standard values for the constants  $C_\mu$ ,  $C_1$  and  $C_2$  were used with  $\sigma_t$  set to a value of 1.

In the momentum equation, the effects of buoyancy were accounted for by the inclusion of the term  $R_{iH}C$  were C is the concentration of the dispersed phase and  $R_{iH}$  is the Richardson number.

The dispersed phase is treated as a scalar and divided into n size classes each with its own concentration and settling velocity, equation 2.25. A source term was added to this equation to account for particles being promoted from one size class to the next by flocculation. A simple flocculation model, assuming only turbulent shear induced flocculation, was used and the importance of this cause of flocculation on solids distribution was examined. The assumption was also made that only particles of the same mean diameter,  $d_h$ , coalesce and that

once collision takes place perfect adhesion of the two particles results. Particles are assumed to smaller than the Kolmogorov length scale,  $(\frac{\mu^3}{\epsilon})^{\frac{1}{4}}$ . Each size class,  $F_{floc}$ , can then be expressed in terms of the concentration of that size class  $c_i$  as;

$$F_{floc} = \left( \frac{\epsilon \rho}{\mu} \right)^{\frac{1}{2}} (\beta_{i-1} c_{i-1}^2 - \beta_i c_i^2) \quad (2.32)$$

The first term in brackets represents a source of particles of ith-size class due to flocculation from  $(i-1)$ th-size class. The second term is the sink of  $i$ th-size class due to coagulation with other particles. The empirical constant  $\beta$ , was tested with values of 1 and 2.

As with other studies, simplifying assumptions were made to the inlet geometry but in this case the sludge hopper was included in the computational domain. Comparisons showed that the velocity of the density current tended to be under predicted, with generally poor prediction of the shape of the density current. It was also observed that the buoyancy modified  $k - \epsilon$  model produced much lower values of turbulent viscosity when compared with the standard  $k - \epsilon$  model - as would be expected. Comparisons of predicted and measured concentration using the multi-disperse settling velocity model, were good at all stations except near the inlet. The turbulent shear-induced flocculation model was found to have a negligible effect on the concentration field. It was concluded that buoyancy effects and the correct modelling of settling velocity were critical in determining accurate concentration profiles.

The effects of changes in viscosity by sediment accumulation leading to the formation of a definite solid bed over which the density driven current could flow was modelled by Dahl(1993), using the Bingham plastic rheological model discussed in section 2.5. Modifications due to buoyancy were introduced into the momentum equation, it had the form shown in equation 2.28. Buoyancy modifications to the  $k - \epsilon$  turbulence model were brought about by the addition

of the term;

$$G_k = g_i \frac{\mu_t}{\rho \sigma_t} \frac{\partial \rho}{\partial x_i} \quad (2.33)$$

to the k- $\epsilon$  model, equations 4.5 and 4.6 respectively. Settling velocity was measured by batch settling test, section 2.4.2. Two dimensional comparisons were carried out against experimental data also gathered by Dahl(1993) from a 7.5m long, 1m high and 1m wide model scale settling tank and on two full scale tanks, at Lynetten and Slagelse in Denmark. The model scale experiment is used for numerical comparisons in this thesis and is described in detail in Chapter 6.

Comparisons of the model against velocity and concentration data gathered on the rig showed good agreement, with maximum velocity, density current depth and concentration in both the free stream and settled bed, being well predicted. The velocity data does show some 3D effects, however. 2D comparisons with the full scale settling tank were less satisfactory and in neither case was direct comparison made with the experimental data as it was considered that the flow field was too qualitatively different. As with the cases outlined above, simplifications to the 3D geometry were made in the inlet region. However, the main reason for the flow field disruption appeared to be the rapid and irregular build up of the settled sludge layer. A second formulation, Bokil and Bewta(1972), describing the changes in rheology with concentration was used instead of the shear thinning Bingham plastic model. The mixture viscosity was then given by;

$$\mu = 3.273x10^{(0.132C)} \quad (2.34)$$

Where C is the concentration of the dispersed phase in  $kg/m^3$ . This formulation improved the height and distribution of the sludge blanket but the main flow field still did not bear comparison with experimental measurements, at this stage the flow field in the tank was disrupted by the density current being reflected off the end wall of the tank.

Lakehal et al. (1999), simulated the flow field and sludge accumulation in a 2D section of a cylindrical clarifier, no comparison being made with experimental results. The model was essentially that used by Dahl (1993), consisting of a momentum equation, equation 2.28, with rheology simulated by a Bingham plastic formulation, section 2.5. Buoyancy modifications were included in the k- $\epsilon$  model; equations 4.5 and 4.6 respectively.

A series of numerical experiments were conducted in order to investigate the effects of varying the  $C_3\epsilon$  coefficient in the  $\epsilon$  equation. It was shown that by decreasing the value of  $C_3\epsilon$ , i.e. bringing more of the buoyancy modification term, equation 2.33, into play, the density current dissipated more quickly than when the term was absent.

## 2.7 Experimental Studies

In this section we look at experimental studies from the perspective of their suitability for model testing. One of the key requirements is that field data for the primitive variables used in the model, principally velocity and concentration, are gathered in the experiment. In addition, other properties of the flow field and the physical properties of the dispersed phase must be measured in order to carry out an accurate numerical simulation. The density, inlet concentration and settling velocity of the activated sludge should ideally be measured with, additionally, the yield stress and plastic viscosity, in order to fully characterise the sludge. The geometry of the tank should be well defined and the inlet and outlet conditions well proscribed. Few experimental studies fulfill all of these requirements.

Stamou and Rodi (1984) carried out a review of sedimentation tank experiments reported in the literature with aim of identifying those suitable for testing mathematical settling tank models. They concluded that the study by Iman (1981) was the only one suitable for this purpose. In this study velocity and FTC curves were measured on a rectangular experimental basin of rela-

tively simple inlet and outlet geometry. The rest of the studies surveyed were rejected because of complicated inlet/outlet geometries that are not entirely defined or can not be approximated easily for 2D simulations. Lack of satisfactory scope and quality of measurements such as incomplete velocity profiles due to the presence of a sludge blanket or due to equipment shortcomings were also a factor. Insufficient information regarding influent concentration with settling velocities that needed to be estimated from empirical formulae, also contributed to the unsuitability of these results. It was noted, however, that some of Larsens (1977) results on full scale settling tanks could be used for validation studies provided that suitable approximations were made in 2D simulations of the 3D geometry. Numerical comparisons have been made on some of these test cases and details are given in section 2.6.2, above.

Larsen's work provides the data for a lock exchange experiment, used in this study to test the predicted velocity of a dense incursion for a given excess density. Details of the experiment together with 2D and 3D numerical comparisons are presented in Chapter 6.

As reported above in section 2.6.2, Dahl (1993) carried out experiments and numerical simulations on a large model scale settling tank using an activated sludge suspension as the working medium. He measured concentration and velocity profiles at 3 stations along the tank centre line over a period of time long enough to observe bed form development, section 2.5.1. In addition, he measured the dispersed phase density, inlet concentration and settling velocity, making this the most complete data set for model scale tanks. This experiment was chosen for numerical comparisons using the drift flux model put forward in Chapter 3. Details of the experiment together with the results of the simulation are described in detail in Chapter 6. Dahl also carried out centre line measurements of velocity and concentration on full scale tanks at Lynetten and Slagelse, again for the purposes of numerical comparisons. Settling velocity and dispersed phase density were measured for each of the cases,

however, only measurements along the centre line of the tank were made and the overall geometry of the tank was not well defined.

For the purposes of testing the numerical model presented in this thesis on a full scale tank, the data set gathered by Ueberl(1995), was selected. Here, a comprehensive experimental study of a working settling tank at Limmattal in Sweden was carried out. Velocity and concentration profiles were gathered at 7 stations along the length and 3 stations across the width of the tank for a variety of inlet conditions and inlet and outlet geometries. A fairly comprehensive picture of the 3D flow field in the main body of the tank was built up. The tank geometry was well defined so no approximations to the inlet geometry needed to be made in the 3D simulation. Volumetric flow rates through the inlets and outlets were measured for each test condition studied, though the inlet concentration is not well defined in each experiment. Settling velocity and rheological properties of the sludge were not measured so the sludge is less well characterised than in the Dahl case. Details of the tank geometry and the experimental conditions for which 2D and 3D numerical simulations have been made is given in Chapter 7.

## 2.8 Closure

In this chapter we have attempted to characterise the problem in terms the physical properties of the activated sludge suspension and in terms of the main features of the flow field. The solid and liquid phases of the suspension can be considered as isothermal, incompressible and without phase change. Section 2.3 illustrated that because the influent into the tank is heavier than the effluent, a density current, with high solids fraction content, is formed which runs practically the entire length of the tank. Most of the settling to the sludge blanket on the tank floor takes place from the density current. The hydrodynamics and flow process of this density stratified feature must be

accurately reproduced in any numerical simulation. In the main body of the tank above the density current a recirculation eddy is formed with low values of solids fraction.

The settling velocity of the dispersed phase was discussed in section 2.4. The accurate prescription of the hindered settling velocity, section 2.4.2, has been shown in previous studies to be of central importance in predicting the dispersed phase distribution within the tank. The exponential formulae put forward in this section were seen to capture the fall off of settling velocity with concentration, as found in settling column experiments, far better than other formulae and they have been used extensively in settling tank studies.

The rheological properties of activated sludge were discussed in section 2.5, it was shown to exhibit concentration dependent shear thinning behaviour, best characterised by the Bingham plastic model. This model, which is used in the numerical simulations in this study, has two components to describe the viscosity, a yield stress,  $\tau_y$ , and a plastic viscosity,  $\eta$ . There is a large range in the magnitude of the laminar viscosity in settling tanks. In the main body of the tank above the density current, the rheology is essentially Newtonian. As the sludge settles and its concentration increases, a settled bed is formed, this region is viscosity dominated and highly non-Newtonian in character, section 2.5.1. Here, if the yield stress exceeds the local shear stress sludge accumulation increases the settled bed height. However, if the shear stress exceeds the local yield stress, liquefaction takes place, eroding the bed and releasing the dispersed phase back into solution.

Sludge accumulation was modelled by Dahl(1993) in a 2D study of a model scale tank using the Bingham plastic model for the rheology of the system. The sludge was seen to accumulate in a physically realistic way with the height and concentration of the settled bed being well predicted over the duration of the experiment. Lakehal et al. (1999) used the same model to simulate sludge accumulation in a 2D simulation of a full scale cylindrical settling tank. It is

important to model the settled bed in order to shed light on the fluid mechanics of the region, especially at the interface between the density current and the settled bed. The depth and accumulation rate of this feature also has a bearing on the performance of the settling tank. Hence, the ability of the model to predict the range of viscosity, particularly the flow field behaviour in the region of the settled bed, is investigated in the numerical simulations carried out in this report.

Previous models of settling tank performance were reviewed in section 2.6. It was observed that single phase models could not reproduce the density driven flow field features found in full scale settling tanks. Buoyancy modifications need to be included in the momentum equation and turbulence models as a minimum requirement such that the density differences in the fluid can drive the density currents in the tank. Those models which include buoyancy terms, section 2.6.2, have treated the two phase mixture as a variable density fluid. A means of transporting the dispersed phase and hence the density and viscosity distribution, also needs to be included in the model. This can be modelled in multi -component form, where the dispersed phase is divided into a number of settling velocity classes each with its own transport equation or by using a single convection diffusion equation with a concentration dependent settling velocity formulation. The multi-component system has shown no advantage over the single equation model but it is computationally more expensive hence, a single component system will be used in this study.

The models reviewed in section 2.6.2 can capture the correct qualitative behaviour in the flow field and in some cases have given accurate quantitative predictions of velocity and concentration. The full scale settling tank studies published so far have all been 2D. Geometric simplifications required to obtain a representative 2D section from a 3D domain, especially in the inlet and outlet regions, have limited the accuracy of velocity and concentration predictions, three dimensional effects being generally present in the velocity data gathered

from full scale tanks. Similarly, only one study included the hopper geometry, so it is necessary to carry out 3D simulations with an accurate reproduction of the complete geometry, to fully test any model.

Experimental studies were surveyed from the perspective of their suitability for comparing with numerical models in section 2.7. Once again, single phase experiments with water do not reproduce the same flow field features found in tanks containing a heavier dispersed phase at the inlet. Of those studies using an influent activated sludge mixture, few were suitable because of incomplete data sets or incomplete characterisation of the sludge and the inlet conditions. Data sets needed to test the numerical model put forward in this thesis were identified, however, most significantly velocity and concentration profiles gathered from a 3D full scale tank at Limmattal, Ueberl(1995).

In the next chapter we shall review the components of the drift flux model used to carry out the simulations presented in this report.

## Chapter 3

# Mathematical Formulation of Two Phase Flow

Multi-phase flows, that is flows involving substances in different physical states, are found extensively in the natural environment and in the chemical, aerospace, water and transport industries. Multi-phase flows are generally categorized by the physical states of the constituent components and by the topology of the interfaces, Ishii(1975). A two-phase flow can be classified as gas-solid, gas-liquid and liquid-solid combinations or in the case of two immiscible liquids, liquid-liquid. Topologically, the flow can be categorised as separated, dispersed or mixed. Such is the diversity of physical phenomena associated with this range of multi-phase flows that no one method is used universally in simulating them. Some mathematical descriptions lend themselves in a more straightforward and economical fashion than others to a given flow field. Hence, part of the task of simulating settling tank performance is choosing the most appropriate mathematical model.

In this chapter we look at two mathematical descriptions of two-phase flow. The first examined, section 3.1, is the Lagrangian approach which tracks each discrete particle separately with its trajectory being governed by its own

equation of motion within the continuous phase. The second, the Eulerian approach, section 3.2, treats the phases as inter-penetrating continua and models each phase by averaging the microscopic equations of motion.

Since we are dealing with the same physical phenomena, both models should come down to the same expression i.e. the dispersed phase momentum equation should be the averaged version of the particle equation of motion. However, different quantities are introduced which do not have an exact counterpart in the other model so it is unclear whether both treatments are identical.

A simplification of the two-fluids model, the drift flux model, is then presented in section 3.3. Here, a single momentum equation, formulated around the mixture center of mass, predicts the overall motion of the two phase mixture with the relative motion of the dispersed phase being predicted by a convection-diffusion equation with a prescribed drift velocity.

### 3.1 Lagrangian Approaches

In the Lagrangian approach, the individual particles of the dispersed phase or a statistical sample thereof, are tracked through the flow domain. The conservation equation of momentum for each of the particles is expressed in a co-ordinate frame of reference which follows the trajectory. The resulting equation, which describes the motion of the particle in the continuous medium, relates the rate of change of the particle's velocity to the sum of forces acting upon it.

$$\rho \frac{d\mathbf{u}_d}{dt} = \Sigma \mathbf{F} \quad (3.1)$$

where  $\mathbf{u}_d$  = Velocity of the dispersed phase particle.

$\rho_d$  = Dispersed phase density.

$\mathbf{F}$  = Individual forces acting on the particle.

The nature of the forces acting on the particle in complicated flow fields has been the subject of attention from a number of workers, e.g. Tchen(1947), Auton (1983) and McLaughlin (1991). The equation of particle motion is generally written as, Elghobashi[1993];

$$\begin{aligned} m_p \left( \frac{d\mathbf{u}_d}{dt} \right) &= m_p F_d (\mathbf{u}_c - \mathbf{u}_d) \\ &+ m_f \left( \frac{D\mathbf{u}_c}{Dt} \right) \\ &+ \frac{1}{2} m_f \left( \frac{D\mathbf{u}_c}{Dt} - \frac{d\mathbf{u}_d}{dt} \right) \\ &+ 6r^2(\pi\rho_c\mu)^{\frac{1}{2}} \int_{t_{p_0}}^{t_p} \frac{\frac{d}{d\tau}(\mathbf{u}_c - \mathbf{u}_d)}{(t_p - \tau)^{\frac{1}{2}}} d\tau \\ &+ (m_p - m_f)g \\ &+ \frac{1}{2}(\pi\rho r^2) C_L L V^2 \end{aligned} \quad (3.2)$$

where;

$d/dt$  = Derivative with respect to time following the moving particle.

$D/Dt$  = Total acceleration of the continuous phase as seen by the particle.

$\mathbf{u}_d$  = Velocity of particle.

$\mathbf{u}_c$  = Velocity of continuous phase.

$g$  = Acceleration due to gravity.

$m_p$  = Mass of particle.  $m_f$  = Mass of fluid displaced by Particle.

$r$  = Radius of Particle.  $F_d$  = Drag force on particle due to relative motion.

$\mu$  = Dynamic viscosity of the continuous phase.

$\rho_d$  = Density of dispersed phase.

$\rho_c$  = Density of continuous phase.

$t_p$  = Particle response time.

$C_L$  = Lift Coefficient evaluated by Saffman.

$L$  = Direction cosines.

$V$  = Magnitude of the relative velocity vector.

The term on the left hand side of equation 3.2 is the inertia force acting on the particle due to its acceleration. The terms on the right hand side are respectively, forces due to viscous and pressure drag, the force due to the fluid pressure gradient and viscous stresses, the inertia force of added mass, the viscous force due to unsteady relative motion ( the Basset force ), the buoyancy force and the Saffman lift force due to shear in the carrier flow.

The strategy of a Lagrangian analysis of two-phase flow is usually to follow a statistically sufficient number of particles individually through the flow domain by solving the above equation for each one. The calculated trajectories are then used to obtain information regarding the average nature of the flow. The continuous phase is usually described using an Eulerian framework, where the flow parameters are related to a fixed co-ordinate reference frame.

This method is of limited use in settling tanks as the number of dispersed phase particles, generally greater than  $10^6$  per ml, Patry(1992), would require a large number of equations to begin to approximate the flow field. This approach has been successfully applied to fluid-gas dispersed flows such as found in fuel injection systems, Kralj(1993).

### 3.2 Eulerian Methods in Two Phase Flow

In the two-fluids approach the particulate phase is considered as a continuum having conservation equations similar to those of the carrier fluid. The instantaneous equations describing the conservation of mass and momentum for each phase are, Elghobashi (1994);

$$\frac{\partial \alpha_k \rho_k}{\partial t} + \nabla \cdot (\alpha_k \rho_k \mathbf{u}_k) = 0 \quad (3.3)$$

$$\frac{\partial \alpha_k \rho_k \mathbf{u}_k}{\partial t} + \nabla \cdot (\alpha_k \rho_k \mathbf{u}_k \mathbf{u}_k) = +\nabla \cdot (\alpha \tau_k) + \alpha_k \rho_k \mathbf{g} + (-1)_k \mathbf{F} \quad (3.4)$$

In the above equations, the subscript  $k$  is the phase index.  $\tau_k$  is the stress tensor which includes the pressure and viscous stresses for each phase,  $\mathbf{g}$  is the acceleration due to gravity, and  $\mathbf{F}$  is the two-way coupling force per unit volume, i.e. the term containing  $\mathbf{F}$  has opposite signs for the two phases.

It can be seen that the momentum equation for a multi-phase system is almost identical to that of the single-phase system except with slight differences in the body force term and the addition of the inter-phase momentum term  $\mathbf{F}$ .

The solution to the foregoing instantaneous equations fully describes the flow field found in internal and external flows. However, high spatial and temporal resolution of the domain of interest would be required for turbulent flows where the motion is characterised as random and irregular with a broad range of length scales. In order to obtain solutions by solving three-dimensional, time dependent problems, very large computational resources would be required. Hence, a statistical averaging procedure is applied to bypass this requirement. From the point of view of physics, the difficulties which are encountered in drawing the field and constitutive equations appropriate to multi-phase flow systems stem from the presence of an interface between the two phases. It is necessary to describe first the local properties of the flow and then obtain a macroscopic description by means of appropriate averaging procedures, which will be done in the next section.

### 3.2.1 Averaging.

According to Hinze (1955), there are three averaging methods, whose applications depends on the characteristics of the turbulent flow:

1. Time averaging for a stationary turbulence;
2. Space averaging for a homogeneous turbulence;
3. Ensemble averaging for a series of identical experiments.

It has become widely recognised that ensemble, or statistical, averaging is

more fundamental than time and volume averaging, Serizawa (1992). Indeed, time and volume averages are regarded as special cases of ensemble averaging. Ensemble averaging is mathematically rigorous and does not impose any time or space resolution restrictions on the final equations and is adopted here.

Many workers, e.g. Politis(1989), Oliveira (1992), derive the two-fluid equations by averaging the microscopic equations twice. The first average, usually a volume average, is applied to the instantaneous equations which are then time averaged to obtain an equation set which is smooth in both space and time. In order to prevent the proliferation of complex terms involving fluctuating volume fractions, fluctuating phase velocities and other flow quantities such as pressure, many workers define phase weighted quantities such as velocity and pressure in a manner akin to Favre (1969) density weighted decomposition employed in compressible flows. This method is an extension of Reynolds, or unweighted, decomposition. However, this method still presents difficulties in accurate modelling and the physical interpretation of the extra terms which are generated in the conservation equations.

More recently, workers in this field have adopted single, usually ensemble averaging, Kataoka (1992), Drew and Wallis (1992). They argue that this is more fundamental than both the time and volume average and does not introduce any spatial or temporal restrictions into the final equations. They also argue that a single averaging procedure suffices because it captures both the two phase and the turbulence effects at the same time. In addition, the number of extra terms introduced in the conservation equations is smaller and their physical significance is more apparent. The ensemble average of a quantity  $\phi$  is given by;

$$\bar{\phi} = \lim N \frac{1}{N} \sum \phi \quad (3.5)$$

Here,  $N$  is the total number of realisations. This single averaging procedure has been further developed with the ‘conditioning’ of the local equations so that contributions to the averaged conservation equation of one phase come

only from regions which contain that particular phase, Hill (1998). Here, conditioning is provided by multiplying the single phase conservation equations by a phase indicator function,  $\chi$ , which is defined as follows;

$$\chi_k(\mathbf{x}, t) = \mathbf{1} \text{ If Phase } k \text{ is present at } (\mathbf{x}, t). \quad (3.6)$$

else

$$\chi_k(\mathbf{x}, t) = \mathbf{0}. \quad (3.7)$$

Mathematically, the phase indicator function may be defined in terms of the Heaviside unit step function operating on an imaginary scalar phase distribution function  $f(x,t)$ . This latter function is defined to be zero at the interface between the phases, positive within phase  $k$  and negative in the other phase. The phase indicator function may be written in terms of the Heaviside unit step function,  $\mathbf{H}\{\}$ , and phase distribution function as;

$$\chi_k = \mathbf{H}\{f_k(x, t)\} \quad (3.8)$$

As the conservation equations contain temporal and spatial derivatives of the dependent variables, conditioning these equations will result in spatial and temporal derivatives of the indicator function. These were defined as follows, Hill (1998), for the spatial derivative of the indicator function;

$$\nabla \chi_k = \delta(f_k) \mathbf{n}_k \quad (3.9)$$

where  $\delta()$  is the Dirac delta function and  $\mathbf{n}_k$  is the unit normal interior to phase  $k$ . The temporal derivative is given by;

$$\frac{\partial \chi_k}{\partial t} = -\mathbf{v}_i \cdot \nabla \chi_k \quad (3.10)$$

where  $\mathbf{v}_i$  is the velocity of the interface. This velocity may be decomposed into the vectorial sum of the velocity of the phase  $k$  at the interface and the surface propagation velocity acting in the direction of the normal to the interface.

For flows with non reacting interfaces with no phase change such as those considered in this work, the surface propagation speed is zero.

Once the local conservation equations have been conditioned, they are ensemble averaged to yield the final forms. This process is applied to the conservation equations for mass and momentum as illustrated below.

### 3.2.2 Two Fluids Model.

#### 3.2.2.1 Conservation of Mass.

The local continuity equations reads;

$$\frac{\partial \rho}{\partial t} + \nabla \cdot (\rho \mathbf{u}) = 0 \quad (3.11)$$

Conditioning the continuity equation with the assumption that the flow is incompressible and without phase change and taking the ensemble average, denoted by an overbar gives;

$$\bar{\chi}_k \frac{\partial \rho}{\partial t} + \bar{\chi}_k \nabla \cdot (\rho \mathbf{u}) = 0 \quad (3.12)$$

Rearranging and substituting equation 3.10 and equation 3.9 with the weighing function;

$$\bar{\phi} = \frac{\bar{\chi}_k \bar{\Phi}}{\alpha_k} \quad (3.13)$$

where  $\alpha_k$  is the phase fraction and  $\phi$  is the quantity under consideration, yields the continuity equation for each phase;

$$\frac{\partial \alpha_k \rho_k}{\partial t} + \nabla \cdot (\alpha_k \rho_k \mathbf{u}) = 0 \quad (3.14)$$

Here, the overbar for the averaged quantity has been omitted.

#### 3.2.2.2 Conservation of Momentum.

The following local single phase conservation equation for linear momentum is used as the starting point in the derivation of the multi-phase conditionally

averaged momentum equations;

$$\frac{\partial \rho \mathbf{u}}{\partial t} + \nabla \cdot (\rho \mathbf{u} \mathbf{u}) = \nabla \cdot \sigma + \rho \mathbf{g} \quad (3.15)$$

Here  $\rho$  is the fluid density and  $\sigma$  is the total stress tensor. This equation is averaged in a similar manner to the continuity equation i.e the conditionally averaged form of the equation is derived, the phase conditional averages are substituted into this equation and the interfacial velocity is decomposed into its component parts. The components of the two phase mixture are again taken as none reacting and hence the interface propagation velocity is zero. The phasic velocities are then decomposed into an unweighted mean plus a fluctuating part, i.e. Reynolds decomposition, whereupon the inertial term gives rise to the Reynolds stresses;  $\tau_k^t$  where  $\tau_k^t = -\rho u_k' u_k'$ . With the averaging over-bar omitted, the resulting equation has the form;

$$\frac{\partial \alpha_k \rho_k \mathbf{u}_k}{\partial t} + \nabla \cdot (\alpha_k \rho_k \mathbf{u}_k \mathbf{u}_k) = -\alpha_k \nabla p_k + \nabla \cdot \alpha_k [\tau_k + \tau_k^t] + \alpha_k \rho_k \mathbf{g} + \mathbf{M} \quad (3.16)$$

In the above it has been assumed that the same pressure acts on both phases and that the inter-facial averaged values of pressure and viscous stress equal the corresponding bulk phase values.

The turbulent stress is assessed to be given by a Newtonian like expression, Launder and Spalding (1974);

$$\tau_k^t = \mu_k^t (\nabla \mathbf{u}_k + \nabla \mathbf{u}_k^T) - \frac{2}{3} (\mu_k^t \nabla \cdot \mathbf{u}_k + \rho_k k_k) \delta \quad (3.17)$$

The eddy viscosity,  $\mu_k^t$ , in the above is obtained from a turbulence model, similar to the practice in single phase flow, and detailed in Chapter 4. The additional term,  $\mathbf{M}$ , represents the transfer of momentum from one phase to the other by phenomena such as drag, virtual mass or lift and needs to be expressed in terms of known quantities in order to obtain a closed equation set.

Two-fluid models can give a very detailed and accurate predictions of a two-phase flow field, see for instance Hill(1998) on bubbly two phase flow; however,

the approach does have some drawbacks. There are some inherent difficulties in modelling the inter-facial momentum transfer terms,  $\mathbf{M}$  in equation 3.16, which couple the two phases together, Hill (1998). Further, these terms can create numerical stability problems in the solution procedure, Olivera (1994).

The physical information needed to make the best use of the two-fluids model, such as detailed information on the shape of sludge flocs, the deformation behaviour of sludge flocs in high velocity gradients and reliable information on sludge rheology, is not available for sewage sludges. Additionally, for simulating the flow field in secondary settling tanks, the two-fluids model may be over elaborate i.e. it may resolve far more detail than necessary to make design decisions. In settling tanks, the main forces shaping the flow field are buoyancy, the settling velocity of the dispersed phase and the rheology of the mixture. The phases involved are isothermal, incompressible and without phase change. More significantly, however, the density ratio between phases is low, generally around 2:1, and the drag between the phases is high, section 2.4.1, hence the two phases respond largely as one to pressure gradients in the settling tank. Such behaviour is known as ‘close coupling’. The slip or drift between the phases is largely due to the gravitational settling of the dispersed phase. Under such circumstances, it is not necessary to solve two continuity equations and two momentum equations to simulate the flow field. In the next section we look at a simpler model, derived from the two-fluids model, which is more applicable to settling tank predictions.

### 3.3 Diffusion (Mixture) Model Field Equations.

The basic concept of the diffusion model is to consider the mixture as a whole rather than the two phases separately. This approach was first proposed by Wallis (1969) and developed to the form presented here by Ishii (1975). It is derived, as shown in Appendix A, by the addition of the two continuity

equations from the two-fluids model resulting in a single mixture continuity equation and by adding the two momentum equations of the two fluids model together to give a single mixture momentum equation based on the mixture centre of mass. In order to predict the distribution of the dispersed phase within the mixture, a convection diffusion equation is derived from the continuity equation of the dispersed phase.

The above operations reduce the total number of equations from four to three. In addition, the inter-phase momentum transfer terms are eliminated; the momentum transferred from one phase is gained by the other, being equal and opposite they cancel when the momentum equations are added with the total momentum of the mixture being conserved. Numerical instabilities associated with these terms are thus eliminated producing a far more robust equation set in which the computational resources needed to solve the system are much reduced from the two-fluids model.

However, the diffusion model requires some drastic constitutive assumptions and with them some of the detail of the motion between the two phases is lost. The relative motion between the phases needs to be expressed by additional constitutive equations i.e. the dynamic interaction relations are replaced by the constitutive laws. In the case of settling tanks, the main source of slip between the phases is the gravitational settling of the dispersed phase which is proscribed in the model by an experimentally derived settling velocity. In the horizontal direction, it is assumed that the two phases act as one in response to accelerations and decelerations in the mixture. In regions of high velocity gradients such as near the wall or settled bed, in shear layers or in recirculation zones, the approach dictates that one phase is not preferentially subject to an unbalanced force which may result in concentration changes of that phase i.e. the Basset and Saffman lift force are considered not to act. Also, it is important that the model is formulated on the mixture center of mass in order to preserve the additive characteristics of the extensive variables.

Using these principles, the general formulation of the mixture model will be now be developed, following this and using the properties of the activated sludge mixture found in settling tanks, a more specific form suitable for the modelling settling tank performance will be presented.

### 3.3.1 Equations of State and Mixture Properties

For the phase fractions we clearly have;

$$\alpha_1 + \alpha_2 = 1 \quad (3.18)$$

For the Mixture density;

$$\rho_m = \alpha_1 \rho_1 + \alpha_2 \rho_2 \quad (3.19)$$

The mixture pressure can be related to the phase pressures by;

$$P_m = \alpha_1 P_1 + \alpha_2 P_2 \quad (3.20)$$

We can define the center of mass mixture velocity  $v_m$  as;

$$v_m = \frac{\alpha_1 \rho_1 v_1 + \alpha_2 \rho_2 v_2}{\rho_m} \quad (3.21)$$

### 3.3.2 Kinematic Constitutive Equations.

As previously explained, it is necessary to supply a constitutive equation for the relative motion of the phases. Since in the diffusion model formulation one momentum equation is eliminated, the kinematic constitutive equation stands as a relative equation of motion.

Firstly, consider the relationship of  $v_{km}$ , the velocity of each phase relative to the mixture center of mass velocity,  $v_m$ , and the phase velocities,  $v_k$  - in this case  $k = 1$  or  $2$ . This relationship is illustrated in Figure 3.1 which shows the streamlines of each phase with the various phase velocities. The relative

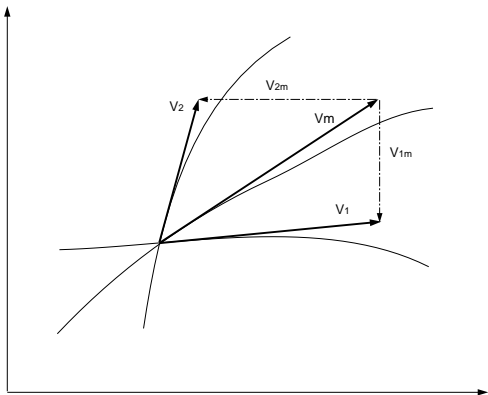


Figure 3.1: Streamline and Velocity Vector Relationship in Two-Phase Flow.  
Ishii (1975).

velocity is given by;

$$v_r = v_1 - v_2 \quad (3.22)$$

The diffusion velocities of each phase, i.e. the velocity with respect to the mass centre of the mixture, are defined by;

$$v_{km} = v_k - v_m \quad (3.23)$$

By substituting equations 3.19 and 3.23 into the equation for the mixture centre of mass velocity, equation 3.21, it can be shown that the diffusion velocity of the phases are related by the identity;

$$\alpha_1 \rho_1 v_{1m} + \alpha_2 \rho_2 v_{2m} = 0 \quad (3.24)$$

We need to supply only one diffusion velocity  $v_{km}$  by a kinematic constitutive equation. This velocity can be related to the relative velocity between phases or, as will be shown in section 3.3.4, to the drift velocity. The diffusion velocity is defined as;

$$v_{2m} = -\frac{\alpha_1 \rho_1}{\alpha_2 \rho_2} v_{1m} = -\frac{\alpha_1 \rho_1}{\rho_m} (v_1 - v_2) \quad (3.25)$$

### 3.3.3 Diffusion Model Field Equations

From the relationships shown in section 3.3.2 and 3.3.1, we can now derive the equations of continuity, diffusion and momentum for the drift model. Details of the derivation are given in Appendix A.2.

The Mixture Continuity Equation is given by;

$$\frac{\partial \rho_m}{\partial t} + \nabla \cdot (\rho_m v_m) = 0 \quad (3.26)$$

The Diffusion Equation or Dispersed Phase Continuity Equation, derived from the continuity equation of the dispersed phase is given by;

$$\frac{\partial \alpha_2 \rho_2}{\partial t} + \nabla \cdot (\alpha_2 \rho_2 v_m) = -\nabla \cdot (\alpha_2 \rho_2 v_{2m}) \quad (3.27)$$

The Mixture Momentum Equation is;

$$\begin{aligned} \frac{\partial \rho_m v_m}{\partial t} + \nabla \cdot (\rho_m v_m v_m) &= \\ -\nabla \cdot P_m + \nabla \cdot [\tau + \tau^t - \Sigma \alpha_k \rho_k v_{km} v_{km}] &+ \rho_m g + M_m \end{aligned} \quad (3.28)$$

The last term on the right hand side,  $M_m$ , is the capillary force which takes into account the surface tension effects and can be considered as a momentum source or sink. The second term on the right hand side, the mixture stress tensor, is composed of three tensor fluxes. They are;

the viscous stress;

$$\tau = \Sigma \alpha_k \tau_k \quad (3.29)$$

the turbulent stress;

$$\tau^t = \Sigma \alpha_k \rho_k v'_k v'_k \quad (3.30)$$

and the diffusion stress;

$$\Sigma \alpha_k \rho_k v_{km} v_{km} \quad (3.31)$$

The derivation of this latter term is shown in Appendix A.2, it represents the momentum ‘diffusion’ due to the relative motion between the two phases.

The mixture turbulent stress tensor, equation 3.30, is modelled in the same way as the turbulent stress tensor for each of the individual phases, equation 3.17 above, i.e. using the ‘eddy viscosity’ concept of Boussinesq(1887). Here, however, the Reynolds stress is related to the mean shear rate of the mixture as a whole using the mixture eddy viscosity  $\mu_t$  which is obtained from turbulence modelling, shown in Chapter 4.

It can be observed that the mixture continuity and momentum equations are similar to those for a single phase flow. The former equation is identical to that for a continuum without internal discontinuities. The mixture momentum equation, however, has two additional terms which do not appear in the single phase equation. In this report the capillary force term  $M_m$  is taken to be zero as data on the magnitude of the forces associated with coalescences, disintegrations and distortions of the dispersed phase is unavailable.

### 3.3.4 Drift Flux Model Field Equations

In a two phase flow system, the drift velocities of each phase, i.e. the velocities with respect to the center of volume of the mixture, are important because the constitutive equations for these velocities in the mixture formulation are relatively simple and accessible. The drift velocity, or in this case the settling velocity, derived from batch settling tests, section 2.4.2, is measured in this way and hence can be used directly in the drift flux formulation. However, the flow field in these tests is laminar. In order to take into account the effects of turbulent diffusion on the dispersed phase we can again use the Boussinesq hypothesis in which the turbulent diffusion of a scalar property is modelled in

analogy with the molecular diffusion. Thus,

$$-\rho u' \phi' = \rho \Gamma \nabla \phi \quad (3.32)$$

where  $\Gamma$ , the turbulent diffusion coefficient, is made equal to the eddy diffusivity, Stamou et al. (1989).

The relative velocity between the phases is defined in equation 3.22 from which we can define the volumetric fluxes of each phase as;

$$\mathbf{j}_k = \alpha_k v_k \quad (3.33)$$

Hence the total volumetric flux is;

$$\mathbf{j} = \Sigma \alpha_k v_k \quad (3.34)$$

The mixture center of mass velocity,  $v_m$ , and the total volumetric flux  $\mathbf{j}$  are not the same because of the difference of the densities of the two phases.

In terms of relative velocity the drift velocity of the phases can be given by;

$$v_{1j} = -\alpha_2 v_r \quad (3.35)$$

and

$$v_{2j} = \alpha_1 v_r \quad (3.36)$$

However, of most significance is the relationship between the diffusion velocity  $v_{km}$  and the drift velocities  $v_{kj}$  which can be defined as;

$$v_{2m} = \frac{\rho_1}{\rho_m} v_{2j} = -\frac{\alpha_1 \rho_1}{\alpha_2 \rho_m} v_{1j} \quad (3.37)$$

The model can now be formulated in terms of the void fraction of the dispersed phase,  $\alpha_d$ , and its drift velocity  $v_{dj}$ , as shown in Appendix A.3. In addition, if we consider the phases to be incompressible and without phase changes, the final form of the equations used in this study can be derived;

Mixture Continuity Equation.

$$\frac{\partial \rho_m}{\partial t} + \nabla \cdot (\rho_m v_m) = 0 \quad (3.38)$$

Drift Equation.

$$\frac{\partial \alpha_d}{\partial t} + \nabla \cdot (\alpha_d v_m) = -\nabla \cdot \left( \frac{\alpha_d \rho_c}{\rho_m} v_{dj} \right) + \nabla \cdot \Gamma \nabla \alpha_d \quad (3.39)$$

Mixture Momentum Equation.

$$\begin{aligned} \frac{\partial \rho_m v_m}{\partial t} + \nabla \cdot (\rho_m v_m v_m) &= \\ -\nabla \cdot P_m + \nabla \cdot [\tau + \tau^t] - \nabla \cdot \left( \frac{\alpha_d \rho_c \rho_d}{1 - \alpha_d} v_{dj} v_{dj} \right) &+ \rho_m g + M_m \end{aligned} \quad (3.40)$$

This model has been used to simulate a number of two phase flow fields with diverse physical properties. Hermann et al (1994) used it in conjunction with a buoyancy modified k- $\epsilon$  model to simulate the front velocity of a density-driven currents of brine, polyester and quartz powder in fresh water. The results compared well with experimental data. These flow fields exhibit the classical features of density-driven currents such as the turn up of the leading edge and the entrainment of air along the upper and lateral surfaces.

### 3.3.5 Closure

In this chapter alternative ways of modelling the two-phase flow field found within settling tanks have been presented. The Lagrangian approach was considered to be unsuitable because of the large computational requirements solving for very high particle number densities found in settling tanks.

The Eulerian approach of treating the phases as inter-penetrating continua is more viable from a computational and physical modelling perspective. There has been considerable debate within the multi-phase modelling community over the most appropriate form of averaging to use for the derivation of the two fluids model. The conditioned-ensemble technique is outlined here where the

equations are first conditioned by a phase indicator function and then ensemble averaged once only. This method avoids excessive and complex correlation terms found in other averaging techniques.

However, the physical properties of activated sludge, primarily the close coupling of the two phases, lend themselves to a simpler Eulerian treatment, namely the Drift Flux model, which is derived from the two-fluids model. With this approach the continuity equations for each phase are added together to yield a mixture continuity equation and the momentum equations are added to yield a single mixture continuity equation. The distribution of the dispersed phase within the mixture is modelled by a convection diffusion equation derived from the dispersed phase continuity equation. Some of the detailed behaviour of the phases is lost, however, and constitutive relationships, generally derived from experiment, must be provided to account for this loss of detail. The assumption is made that the main source of slip between the phases is gravitational settling which is proscribed in the model by an experimentally derived settling velocity. In the horizontal direction, it is assumed that the two phases act as one in response to accelerations and decelerations in the mixture. It is also assumed that in regions of high velocity gradients such as near the wall or settled bed, in shear layers or in recirculation zones, one phase is not preferentially subject to an unbalanced force which would result in concentration changes of that phase. Although it is possible to include the effects on the mixture momentum of disintegrations and coalescences, they are assumed not to take place in this case. The effects of turbulence are modelled using the eddy viscosity hypothesis where the eddy viscosity is obtained from a turbulence model, which is the subject of the next chapter.

# Chapter 4

## Turbulence Modelling.

### 4.1 Introduction.

The averaging procedures outlined in section 3.2.1 produces additional terms in the transport equations involving correlations of the fluctuating components. Modelling these terms is known as turbulence closure. In this study the Boussinesq turbulent or eddy viscosity hypothesis is used in which the turbulent stresses and turbulent scalar fluxes are expressed by equations 3.17 and 3.32 respectively. Hence, the key to completing the numerical model is in the calculation of the eddy viscosity. Following on from other workers, Rodi(1992), Dahl(1993), the buoyancy modified k- $\epsilon$  model, Rodi(1993), is used in this study. These studies have shown it to be accurate, stable and computationally economical in comparison to other models such as the algebraic stress model or the Reynolds stress model.

The standard k- $\epsilon$  model is based on the assumption that the eddy viscosity is isotropic, i.e that it is the same for all Reynolds stresses,  $u_i' u_j'$ . However, two phases are present in settling tanks and it is necessary to examine the effects of the dispersed phase on turbulent quantities, this is done in sections 4.2 and 4.3. The k- $\epsilon$  equations used in this study are presented in section 4.4

and a comparison calculation in which the standard and buoyancy modified k- $\epsilon$  equations are applied to a test case, Dahl (1993), is shown in section 4.5.

### 4.2 General Effects of The Dispersed Phase.

The flow field found in settling tanks should be turbulent with  $Re$  in the range 8,000 to 45,000 because of the large length scales, section 2.3, however, the presence of a solid dispersed phase affects the production, dissipation and transport of turbulence. Over the years considerable effort has been extended in the numerical simulation of turbulence in such flows, Danon (1976), Elghobashi(1994), Olivera (1994), Hill (1998). There are two main challenges in this field, Elghobashi(1994);

(i) There is a very wide spectrum of important length and time scales. These scales are associated with the microscopic physics of the dispersed phase in addition to those of the fine and large structures of turbulence. Simply, it is not possible to simultaneously resolve the large scale motion and the flow around all the individual dispersed particles.

(ii) Despite the numerous efforts devoted to the study of turbulence in single phase flows the understanding of the physics of turbulence remains incomplete, this sets an upper limit on the current understanding of the more complex particle-laden turbulent flows.

The effect on turbulence of a particulate dispersed phase can be classified by the dispersed phase concentration  $\alpha$ , which gives an indication of the type of interaction between the particles and turbulence. For  $\alpha < 10^{-6}$  the particles have a negligible effect on turbulence and the interaction between the particles and turbulence is termed as one-way coupling. This means that the particle

dispersion in this regime depends on the state of turbulence, but due to the low concentration of particles the momentum transfer from the particles to the turbulence is negligible. For  $10^{-6} < \alpha < 10^{-3}$  the momentum transfer from the particles is large enough to alter turbulence structure. This interaction is called two-way coupling. In this regime and for any given value of  $\alpha$ , lowering the particle response time,  $\tau_p$ , which for Stokes flow is given by;

$$\tau_p = \frac{\rho_p d^2}{18\rho_f \mu} \quad (4.1)$$

increases the dissipation rate of turbulence. On the other hand, as  $\tau_p$  increases for the same  $\alpha$ , the particle Reynolds number,  $Re_p$ , increases and at values of  $Re_p > 400$  vortex shedding takes place resulting in enhanced production of turbulence energy. The two regimes above are referred to as dilute suspensions. The third regime,  $\alpha > 10^{-3}$ , is referred to as a dense suspension. Here, in addition to the two-way coupling between the particles and turbulence, particle/particle collision takes place resulting in four-way coupling.

All three regimes are found in settling tanks. Under good operating conditions the flow field near the surface exhibits one-way coupling, as concentration increases towards the tank floor the two-way and then the four-way coupling regimes are found. It can be observed that the dispersed phase acts to dissipate turbulence in the settling tank flow field. In the two-way coupling regime, the dispersed phase enhances dissipation as  $Re_p << 400$ , section 2.4. Similarly, in the density current with high concentrations of  $\alpha$ , the four way coupling regime, even greater dissipation of turbulence occurs.

Turbulence models with widely different levels of sophistication have been developed to predict these flows. However, there is a limit to the degree of sophistication that can be applied in this case. Firstly, using the Drift Flux model some of the detailed behaviour of the motion of the phases is lost by considering only an overall mixture momentum equation, kinematic constitutive relationships, section 3.3.2, being used to complete the description of the phase

behaviour. Secondly, the experimental measurements of turbulence and turbulent particle interactions in full scale tanks is practically non-existent and this limits the degree of sophistication of any model used to simulate turbulence in settling tanks.

However, one of the major effects of the dispersed phase on turbulence can be accounted for by considering the changes in mixture buoyancy brought about by concentration changes. Buoyancy is a major force in shaping the flow field of the settling tanks as through flow velocities are generally low and the ratio of buoyancy to inertial forces, characterised by the densimetric Froude number - section 2.3, is less than unity.

### 4.3 Buoyancy Effects.

When buoyancy forces are present, there is an exchange between potential energy of the mean flow and turbulent kinetic energy. In stable stratification, where the lighter fluid overlays a more dense fluid, turbulence is damped and the eddy viscosity and diffusivity are reduced Rodi (1979). In unstable stratification, turbulent energy is produced. In this study the well known  $k-\epsilon$  turbulence model of Rodi (1993) is used with a buoyancy modification term in the  $k$  equation to account for density stratification, brought about by the unequal distribution of the dispersed phase in the settling tank. This buoyancy term is modelled in the same way as other turbulent fluxes, equation 3.32, from the expression in the exact  $k$  equation  $-g\rho'v'/\rho$ . It has the form;

$$G_k = g_i \frac{\mu_t}{\rho \sigma_t} \frac{\partial \rho}{\partial x_i} \quad (4.2)$$

## 4.4 Buoyancy Modified $k-\epsilon$ equations

The turbulent kinetic energy,  $k$ , is given by;

$$k = \frac{1}{2} (u'^2 + v'^2 + w'^2) \quad (4.3)$$

The Eddy Viscosity is given by;

$$\mu_t = C_\mu \rho \frac{k^2}{\epsilon} \quad (4.4)$$

The buoyancy modified  $k-\epsilon$  model has the following form;

Turbulent Kinetic Energy.

$$\frac{\partial \rho k}{\partial t} + \nabla \cdot (\rho \mathbf{v} k) = \nabla \cdot \left( \frac{\mu_t}{\sigma_t} \nabla k \right) + P_k + G_k - \rho \epsilon \quad (4.5)$$

Dissipation Rate;

$$\frac{\partial \rho \epsilon}{\partial t} + \nabla \cdot (\mathbf{v} \rho \epsilon) = \nabla \cdot \left( \frac{\mu_t}{\sigma_t} \nabla \epsilon \right) + C_{1\epsilon} \rho \frac{\epsilon}{k} (P_k + G_k - C_{3\epsilon} G_k) - C_{2\epsilon} \rho \frac{\epsilon^2}{k} \quad (4.6)$$

A single value of  $C_{3\epsilon}$  can not be used because the contribution of the buoyancy term in the  $\epsilon$  equation in vertically buoyant shear layers, i.e. the kind of shear layer found in the density waterfall at the inlet to a settling tank, is different from the contribution in horizontal shear layers as found in the density current. It has intermediate values depending on the angle of orientation of the shear layer to the vertical.

Zhou and McCorquodale (1992) omitted the buoyancy correction terms in the  $k-\epsilon$  as a first approximation. Lyn et al. (1992), did not include the buoyancy term in the  $\epsilon$  equation on the basis of work done by Simonin et al. (1989), but did include it in the  $k$  equation, such an approach has been adopted in this study. Lakehal et al. (1999) demonstrated that when  $C_{3\epsilon} = 0$ ,

in equation 4.6, i.e. when the full value of the production term is included in the  $\epsilon$  equation, turbulent diffusivity increases and the density current dissipates more quickly than when the term is absent from this equation, i.e. when  $C_{3\epsilon} = 1$ .

The constants used in the equations are;  $C_\mu = 0.09$ ,  $C_{1\epsilon} = 1.44$ ,  $C_{2\epsilon} = 1.92$ ,  $\sigma_t = 1.0$ ,  $\sigma_\epsilon = 1.2$

## 4.5 The Effects of Buoyancy Modification on the flow field.

At the densimetric Froude numbers found in settling tanks, the buoyancy modifications in the  $k-\epsilon$  equations bring about profound changes not only in the generation and distribution of  $k$  and  $\epsilon$  but also in the velocity field via  $\mu_t$  in the momentum equation.

A calculation using the Drift Flux model of Chapter 3 has been carried out comparing the standard  $k-\epsilon$  model, the buoyancy modified  $k-\epsilon$  model and a laminar flow field for a non-cohesive sediment. The case chosen was from the Dahl series of model scale experiments with a flow rate of 19.1l/s, a detailed description of the experiment with the results from the full simulation is given in section 6.4. For this case, a uniform inlet velocity of 0.0191m/s was proscribed with a uniform solids fraction of 0.001, the dispersed phase density is  $2000\text{kg/m}^3$  and water is the continuous phase, turbulent intensity at the inlet was set to  $u' = 10\%$ . Bingham plastic effects are not modelled in the following simulation.

It can be observed from vector plots of velocity, Figures 4.1, 4.2 and 4.3, that the flow field characteristics, namely the distinctive velocity profile associated with the density current, are very quickly lost with the standard  $k-\epsilon$  model. However, the vector field from the Buoyancy modified  $k-\epsilon$  model and

the laminar flow preserve this feature and are similar to each other. The laminar and buoyancy modified velocity fields bear closer comparison to the experimental measurements in terms of the shape, depth and maximum velocity of the density current than the velocity field generated with the standard  $k-\epsilon$  model. This is reinforced in graphical comparisons of the horizontal component of velocity shown in Figure 4.8, all the plots in this figure were taken through a vertical section at the mid point of the tank.

Figures 4.4 and 4.5 show a clear and identifiable stratification of effective viscosity has taken place with the buoyancy modification, steep gradients of effective viscosity are found at the top of the density current whilst the values at its core are relatively constant, resulting in a very different distribution of  $\mu_{eff}$  to that found in the standard model. This effect can also be observed in the contour plots of turbulent intensity, Figures 4.6 and 4.7. Graph plots, Figure 4.8, show that the overall level of  $k$  is less with the buoyancy modification, the maximum value being less than half the maximum of the standard model. Turbulence is generated at the top of the density current, mainly within the ambient fluid in the tank, and at the bottom on the tank floor, the core value being fairly constant. On the plot the core value of  $k$  appears to be zero, this is not the case, the core value is in fact very close to the inlet value but this does not register on the scale used in the plot.

Hence, despite the fact that velocity gradients within the density current are higher than in the the ambient fluid, turbulent production is damped in the density current by the density stratification, this reduces turbulent viscosity and the transfer of momentum out of the density current by mixing. Density current spreading rate, which can be considered as an analogous process to jet spreading rate is thus reduced preserving the high velocity gradients within the density currents and maintaining its similarity to the laminar condition. Numerical studies have shown that the overall depth and spreading rate of the density current is unaffected by inlet values of turbulent intensity within the

range  $1\% < u' < 30\%$ .

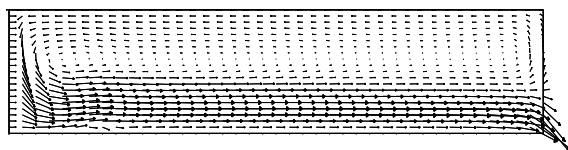
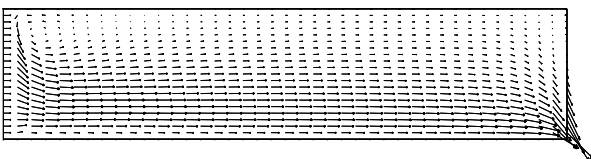
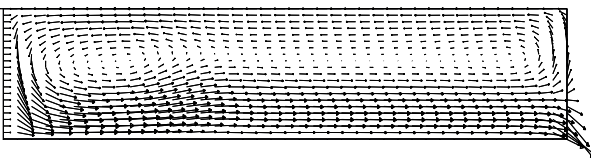
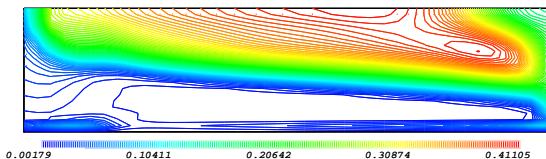
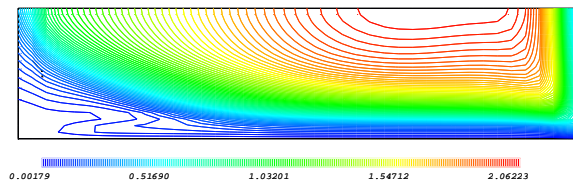
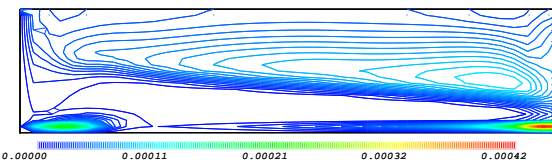
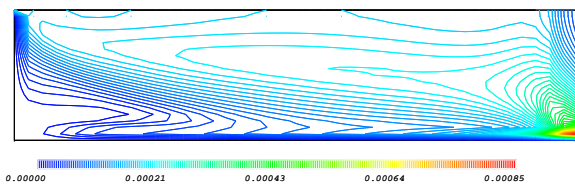
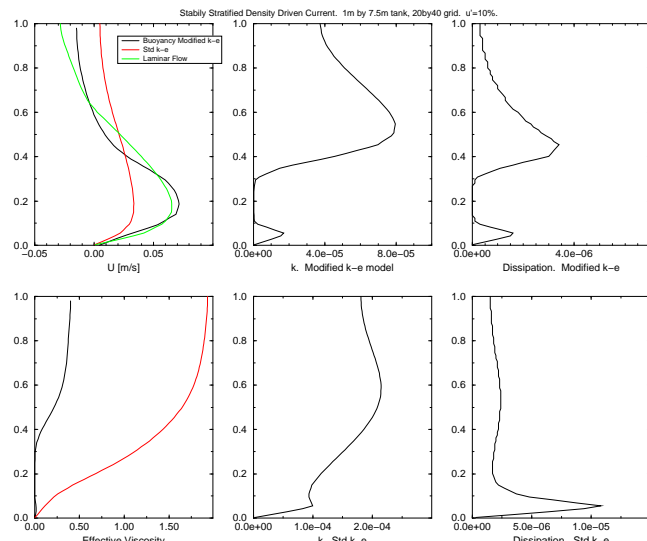
Figure 4.1: Buoyancy Modified  $k-\epsilon$  Model, Velocity Field.Figure 4.2: Standard  $k-\epsilon$  Model, Velocity Field.

Figure 4.3: Laminar Flow, Velocity Field.

Figure 4.4: Buoyancy Modified  $k-\epsilon$  Model, Effective Viscosity.Figure 4.5: Standard  $k-\epsilon$  Model, Effective Viscosity.

Figure 4.6: Buoyancy Modified  $k-\epsilon$  Model, Turbulent Intensity.Figure 4.7: Standard  $k-\epsilon$  Model, Turbulent Intensity.Figure 4.8: Comparisons of Laminar Flow, Standard and Buoyancy Modified  $k-\epsilon$  Models.

## 4.6 Closure

In this chapter the final part of the mathematical model has been put into place. Here, the Reynolds stresses brought about by turbulent fluctuations are related to the mean shear rate by an eddy viscosity, the eddy viscosity is calculated by the well known and extensively tested  $k-\epsilon$  turbulence model. However, the presence of a dispersed phase produces large scale alterations in the structure of turbulence, the overall nature of these changes in relation to the solids fraction concentration has been discussed. Modelling the overall effects of the dispersed phase by the inclusion of a relatively straightforward buoyancy modification term was shown to produce large scale changes in the generation and distribution of  $\mu_t$ , altering the overall flow field and, as will be shown in chapter 6, improving the predictive accuracy of the simulations.

# Chapter 5

## Numerical Solution Procedure.

### 5.1 Introduction.

This Chapter describes the procedure by which the Drift Flux and Turbulence equations, presented in Chapters 3 and 4 respectively, are solved numerically. The procedure is an implicit iterative method based on a finite volume discretisation technique using the PISO (Pressure Implicit with Splitting of Operators) , Issa (1986), pressure correction algorithm. A co-located mesh is used in which the solution variables are stored at cell centres. Special consideration is given to modifications of the Rhie and Chow (1983) interpolation technique such that buoyancy dominated problems can be solved to a greater degree of accuracy on co-located meshes.

The solution procedure is generally regarded as having three stages. The first stage involves the discretisation of the solution domain into a number of tessellating polyhedral cells over which each of the governing equations are integrated, this results in a set of linear algebraic equations which are then solved using the appropriate solver. The discretisation of the solution domain and governing equations are discussed in sections 5.2 and sections 5.3 respectively, the application of the boundary conditions is discussed in sections 5.2.

The second stage concerns the two-phase numerical solution procedure, whose purpose is to maintain the coupling between the equations and impose continuity and boundedness constraints on the system as a whole. The third stage is post processing where the results of the calculation are displayed in the computational domain either as contour or vector plots.

### 5.2 Discretisation of the Solution Domain.

The flow space under consideration is subdivided into many tessellating polyhedral sub-volumes or cells. The co-located variable arrangement used in this study defines the primitive variables such as pressure, velocity, etc, at the cell centres, Perić (1985). This arrangement simplifies the computer programming and minimises the amount of geometrical information required about the grid. The general layout and notation used by Jasak (1996) and Ubbink (1997) is also used in this study.

Figure 5.1 represents a typical control volume with an arbitrary number of faces. The computational point  $P$  is in the centre of the control volume. The vector  $\mathbf{d} = PN$  connects the computational point  $P$  with its neighbour  $N$  and  $\mathbf{A}$  is the outward-pointing face area vector normal to the face. The mesh is

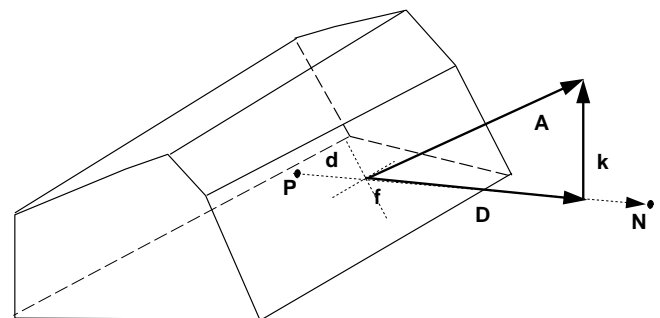


Figure 5.1: Control Volume.

defined as being non-orthogonal if the angle between the vectors  $\mathbf{A}$  and  $\mathbf{d}$  is not zero. The vectors  $\mathbf{D}$  and  $\mathbf{k}$  are then introduced to account for the orthogonal and non-orthogonal contributions to gradients at cell faces respectively. Jasak (1996) describes three different approaches for splitting of the non-orthogonal contribution  $\mathbf{k}$  from the orthogonal component  $\mathbf{D}$ . The so called over relaxed approach has shown to be the superior of the three approaches and will be used in this study for the discretisation of the momentum and pressure equation. The vectors  $\mathbf{D}$  and  $\mathbf{k}$  for the over relaxed approach are defined as;

$$\mathbf{D} = \frac{\mathbf{d}}{\mathbf{d} \cdot \mathbf{A}} |\mathbf{A}|^2 \quad (5.1)$$

$$\mathbf{k} = \mathbf{A} - \mathbf{D} \quad (5.2)$$

### 5.3 Discretisation of the Governing Differential Equations.

Once the solution domain has been defined, the governing equations are discretised by integrating them over each cell and applying Gauss' theorem which translates a volume integral to a surface integral, Perić (1985). The values of the primitive variables on the cell faces are then rewritten in terms of neighbouring cell centre values yielding an algebraic equation for that cell. The result is a set of linear algebraic equations, one for each discretised equation, written in terms of the mesh cell centre values, Hill (1997).

In order to facilitate this process, the governing differential equations are written in terms of a general differential equation, equation 5.3, the individual terms being grouped into convection, diffusion or source terms. The discretisation of each group of terms is the same for all equations. The generic form of the transport equation for any scalar or vector quantity  $\phi$  is written as;

$$\frac{\partial \rho\phi}{\partial t} + \nabla \cdot \rho \mathbf{u}\phi = \nabla \cdot \rho \Gamma_\phi \nabla \phi + S_\phi \quad (5.3)$$

where  $\rho$  is the density,  $\mathbf{u}$  is the velocity and  $\Gamma_\phi$  is the diffusion coefficient. The source term,  $S_\phi$ , may also include additional fluxes or stress components. The corresponding values for  $\Phi$ ,  $\Gamma_\phi$  and  $S_\phi$  for the mass, momentum and convection diffusion equations of the Drift Flux model are summarised in Table 5.1. A similar break down for the turbulent kinetic energy and dissipation rate equations can be found in Lixing (1993).

Equation	$\Phi$	$\Gamma_\phi$	$S_\phi$
Continuity Equation	1	0	0
Mixture Momentum	$\mathbf{u}_m$	$\mu_{eff}$	$-\nabla P_m + \nabla \cdot (\tau + \tau^t) - \nabla \cdot \left( \frac{\alpha_d}{1-\alpha_d} \frac{\rho_c \rho_d}{\rho_m} v_{dj} v_{dj} \right) + \rho_m g$
Solids Fraction	$\alpha$	$\frac{\mu_t}{\sigma}$	$\nabla \Gamma_\phi \nabla \alpha$

Table 5.1: Generic Form of The Drift Flux Model.

The generalised form of Gauss' theorem is used frequently and is defined below for various spatial derivatives of a vector or scalar quantity  $\Phi$ ;

$$\int_V \nabla \cdot \Phi dV = \int_{\delta S} \Phi \cdot d\mathbf{S} \quad (5.4)$$

$$\int_V \nabla \Phi dV = \int_{\delta S} \Phi d\mathbf{S} \quad (5.5)$$

$$\int_V \nabla \otimes \Phi dV = \int_{\delta S} d\mathbf{S} \otimes \Phi \quad (5.6)$$

where  $d\mathbf{S}$  is the surface area vector and  $\delta S$  is the closed bounding surface of the cell.

The control volume is bounded by a series of flat faces and hence the surface integrals can be written in terms of a sum of integrals over each face, for example;

$$\begin{aligned}\int_V \nabla \cdot \Phi dV &= \int_{\delta S} \Phi \cdot d\mathbf{S} \\ &= \sum_{f=1}^n \left( \int_f \Phi \cdot d\mathbf{S} \right) \\ &\approx \sum_{f=1}^n \mathbf{A}_f \cdot \Phi_f\end{aligned}\quad (5.7)$$

where  $f$  is the centre of the cell face,  $\mathbf{A}_f$  is the face area vector and  $n$  is the number of faces in a control volume. Similarly, the volume integrals shown in equations 5.5 and 5.6 can be cast in terms of the face area vector of the computational cells;

$$\int_V \nabla \Phi dV = \sum_{f=1}^n \mathbf{A}_f \Phi_f \quad (5.8)$$

$$\int_V \nabla \otimes \Phi dV = \sum_{f=1}^n \mathbf{A}_f \otimes \Phi_f \quad (5.9)$$

Unless otherwise stated, the face values are obtained by linear interpolation;

$$\Phi_f = L_p \Phi_P + (1 - L_p) \Phi_N \quad (5.10)$$

The interpolation of a vector is the interpolation of each of the components and the interpolation factor  $L_p$  is defined as the ratio of the distances  $fN$  and  $PN$ :

$$L_p = \frac{|fN|}{|PN|} \quad (5.11)$$

### 5.3.1 Convection Terms.

The finite volume discretisation of the convection term yields;

$$\begin{aligned}\int_{\Delta V} \nabla \cdot \rho \mathbf{u} \phi dV &= \sum_f \mathbf{A}_f \cdot (\rho \mathbf{u} \phi)_f \\ &= \sum_f \mathbf{A}_f \cdot (\rho \mathbf{u})_f \phi_f \\ &= \sum_f \mathbf{F}_f \phi_f\end{aligned}\quad (5.12)$$

Where  $\mathbf{F}_f$  is the face mass flux given by;

$$\mathbf{F}_f = \mathbf{S}_f \cdot (\rho \mathbf{u})_f \quad (5.13)$$

The cell face flux is an important quantity and is calculated directly by the solution algorithm, as shown in section 5.3.5, rather than from cell face values for the velocity, density etc. For convective fluxes, the flow field variable in question is effectively transported across the cell face into or out of the cell by the cell face flux. The cell face average value,  $\phi_f$ , is determined from the cell nodal values via the ‘differencing scheme’. A number of differencing schemes exist with each scheme having its own advantages and disadvantages. The issues surrounding the choice of differencing scheme are the boundedness of the solution, the stability and overall accuracy of the scheme and the computational resources required for its implementation. These considerations are discussed in detail by Jasak (1996).

Convective fluxes are determined in this work either by upwind differencing, Patankar(1980), or by the Gamma scheme of Jasak (1996). This later scheme guarantees a bounded solution whilst minimising the numerical diffusion of sharp changes in gradient of the variable. The upwind scheme determines the value of  $\phi$  at the cell face by considering the direction of the flow normal the cell face. The value at the cell face is set equal to the value of the cell node from the upwind direction, thus;

$$\mathbf{F}_f \phi_f = \phi_p \max[\mathbf{F}, 0] - \phi_n \max[-\mathbf{F}, 0] \quad (5.14)$$

where the subscripts p and n indicate the current and neighbouring cell values respectively and the operator  $\max[a,b]$  indicates the maximum value of a and b.

The Gamma scheme, Jasak (1996), is a High Resolution (HR) second order convection-diffusion differencing scheme based on the Normalised Variable Diagram (NVD) (Leonard (1991)), specially developed for unstructured meshes. The face value of u the magnitude of the velocity vector  $\mathbf{u}$  is defined as;

$$u_f = \begin{cases} u_D & \text{for } \tilde{u}_D \leq 0 \text{ or } \tilde{u}_D \geq 1. \\ \frac{1}{2}(u_D + u_A) & \text{for } k \leq \tilde{u}_D < 1. \\ \left(1 - \frac{\tilde{u}_D}{2k}\right)u_D + \frac{\tilde{u}_D}{2k}u_A & \text{for } 0 < \tilde{u}_D < k. \end{cases} \quad (5.15)$$

where k is a prescribed constant with a value between 0 and 0.5. The recommended value is  $k = 0.1$ . The subscripts D and A are determined by the direction of the flow:

$$F_f \geq 0 \Rightarrow D = P \& A = N \text{ or } F_f < 0 \Rightarrow D = N \& A = P \quad (5.16)$$

The decision factor  $\tilde{u}_D$  is defined as;

$$\tilde{u}_D = 1 - \frac{u_A - u_D}{2(\nabla u)_D \cdot \mathbf{d}} \quad (5.17)$$

and

$$(\nabla u)_D = \frac{1}{V_D} \sum_{f=1}^n \mathbf{A}_f u_f \quad (5.18)$$

### 5.3.2 Diffusion Terms.

The finite volume discretisation of the diffusion term using Gauss' theorem has the form;

$$\begin{aligned} \int_{\Delta V} \nabla \cdot \rho \Gamma \phi \nabla \phi &= \sum_{f=1}^n \mathbf{S}_f \cdot (\rho \Gamma \nabla \phi)_f \\ &= \sum_{f=1}^n (\rho \Gamma)_f \mathbf{S}_f \cdot (\nabla \phi)_f \end{aligned} \quad (5.19)$$

where the viscosity at the face  $\mu_f$  is calculated by linear interpolation with  $L_p$  calculated from equation 5.11;

$$\mu_f = L_p \mu_p - (1 - L_p) \mu_n \quad (5.20)$$

For an orthogonal mesh, the calculation of the gradient at the cell face is relatively straight forward using the nodal values straddling the cell face;

$$\mathbf{A}_f \cdot (\nabla \phi)_f = |\mathbf{A}_f| \frac{\phi_n - \phi_p}{\mathbf{d}} \quad (5.21)$$

where the vector  $\mathbf{d}$  connects the current and neighbouring cell nodes. If the mesh is non-orthogonal it is necessary to introduce an additional term to account for the fact that the face area vector is no longer co-linear with the vector  $\mathbf{d}$ . This is done by using  $\mathbf{A}_f = \mathbf{D}_f + \mathbf{k}_f$ , the over relaxed non-orthogonal decompositions of the face area vector, Jasak (1996), i.e;

$$\mathbf{A}_f \cdot (\nabla \phi)_f = |\mathbf{D}_f| \frac{\phi_n - \phi_p}{\mathbf{d}} + |\mathbf{k}_f| \frac{\phi_n - \phi_p}{\mathbf{d}} \quad (5.22)$$

In this case the non-orthogonal correction is treated explicitly.

### 5.3.3 Source Terms.

Terms in the general transport equation which can not be treated as convective or diffusive terms are included as source terms. In this case, it includes the

extra stress term,  $\left(\frac{\alpha_d}{1-\alpha_d} \frac{\rho_c \rho_d}{\rho_m} v_{dj} v_{d\bar{j}}\right)$ , in the drift flux momentum equation. The treatment of these terms follows that of Patankar (1980) in which the source terms are linearised and take the form;

$$S = S_u + S_p \phi_p \quad (5.23)$$

Integration of equation 5.23 over the control volume gives;

$$\int_{\delta V} S_\phi dV = S_u \Delta V + S_p \phi_p \Delta V \quad (5.24)$$

The coefficient  $S_u$  is added directly to any existing source term. If the coefficient  $S_p$  is negative it can be added to the central coefficient of the solution matrix increasing its diagonal dominance and enhancing the stability of the solution, however, if it is positive then it is solved explicitly. The buoyancy term, equation 4.2, in the turbulent kinetic energy equation is treated in such a fashion with the sign of the density gradient being used as the discriminant.

The time dependent term of the general equation is also discretised as a source term, it has the form;

$$\begin{aligned} \int_t^{t+\delta t} \frac{\partial}{\partial t} \left( \int_V \phi dV \right) dt &= \int_t^{t+\delta t} \frac{\partial}{\partial t} (\phi_p \Delta V) dt \\ &= (\phi_p^{t+\delta t} - \phi_p^t) \Delta V \end{aligned} \quad (5.25)$$

#### 5.3.4 Final Form of the Discretised Equation.

The discretisation of the generic transport equation yields an equation for  $\phi$  in each cell written in terms of the values of  $\phi$  in the neighbouring cells, Hill (1998). Grouping the coefficients of the cell under consideration and its neighbours, results in the following equation;

$$a_P \phi_P^{t+\delta t} = \sum_{f=1}^{nb} a_{nb} \phi_{nb}^{t+\delta t} + S_u \quad (5.26)$$

where the sum is over all neighbouring cells and  $a_P$  and  $a_{nb}$  represents the central and neighbouring coefficients respectively. The central coefficient is given by;

$$a_P = \sum_{f=1}^{nb} a_{nb} - S_P \quad (5.27)$$

#### 5.3.5 Pressure Equation.

A well known problem associated with the calculation of pressure on co-located meshes is one of ‘checkerboarding’ in which velocity and pressure become decoupled, Patankar(1980). This may result in a physically unrealistic pressure field prediction being made from a correct solution to the momentum and continuity equations. This problem can be solved by interpolating the discretised form of the momentum equation onto the cell faces and applying the continuity constraint to the cell face velocities. From these two equations a pressure correction equation is generated, Rhie and Chow (1983), with the pressure gradient at the cell face being calculated from the nodal values either side of it. This is physically realistic as changes in momentum are generally brought about by the static pressure gradient and the Rhie and Chow method works well on co-located meshes under circumstances where the static pressure is the major driving force.

However, with decreasing densimetric Froude number, typically those values found in settling tanks, the Rhie and Chow interpolation becomes increasingly inaccurate in calculating the hydrostatic pressure gradient at the cell face. Hence, in this study, a special treatment, developed by Weller (1997),

was introduced to compliment the standard method of assembling the pressure correction equation. Here, the hydrostatic pressure is extracted from the piezometric pressure and treated separately. The density gradient across the cell face, required for this treatment, is then calculated from the nodes either side of it - in a similar fashion to the standard treatment of pressure. This method introduces a degree of physical realism into the calculation of hydrostatic pressure and enables buoyancy forces to drive changes in momentum. In the following derivation the subscript  $m$ , used to denote mixture properties in the momentum equation, is dropped from all terms for convenience.

The pressure equation is derived from the continuity constraint, equation 3.39 and the discretised momentum equation. The discretised continuity equation has the form;

$$\int_V \nabla \cdot \rho \mathbf{u} dV = \sum_{f=1}^n \mathbf{A}_f \cdot \rho \mathbf{u} = 0 \quad (5.28)$$

Conventionally, the standard form of the discretised momentum equation, 5.26, is modified by extracting the pressure;

$$a_P \mathbf{u}_P^{t+\delta t} = \sum_{nb=1}^n a_{nb} \mathbf{u}_{nb}^{t+\delta t} + S u_P - (\nabla P)_P \quad (5.29)$$

However, in buoyancy dominated problems the hydrostatic part of the pressure needs to be extracted and treated separately;

$$P = P'' + \rho \mathbf{g} \cdot \mathbf{h} \quad (5.30)$$

where  $P''$  is that part of the piezometric pressure remaining after the hydrostatic pressure has been removed,  $\mathbf{g}$  is the gravity vector and  $\mathbf{h}$  is the height from a given datum in the vertical direction. It can be seen that the buoyancy term is zero in the horizontal direction where  $\mathbf{g}$  is zero. The divergence of the

pressure becomes;

$$\begin{aligned} \nabla P &= \nabla P'' + \mathbf{g} \cdot \nabla \rho \mathbf{h} \\ &= \nabla P'' + \mathbf{g} \cdot (\rho \nabla \mathbf{h}) + \mathbf{g} \cdot \mathbf{h} \nabla \rho \\ &= \nabla P'' + \rho \mathbf{g} + \mathbf{g} \cdot \mathbf{h} \nabla \rho \end{aligned} \quad (5.31)$$

Substitution of equation 5.31 into equation 5.29 gives;

$$a_P \mathbf{u}_P^{t+\delta t} = \sum_{nb=1}^n a_{nb} \mathbf{u}_{nb}^{t+\delta t} + S u_P - (\nabla P'' + \mathbf{g} \cdot \mathbf{h} \nabla \rho)_P \quad (5.32)$$

where the  $\rho \mathbf{g}$  term derived from the hydrostatic pressure gradient and the buoyancy term in the momentum equation cancel out. The pressure correction is obtained by rearranging equation 5.32 to give;

$$\mathbf{u}_P^{t+\delta t} = \frac{\mathbf{H}(\mathbf{u})_P}{a_P} - \frac{1}{a_P} (\nabla P'' + \mathbf{g} \cdot \mathbf{h} \nabla \rho)_P \quad (5.33)$$

where

$$\mathbf{H}(\mathbf{u})_P = \sum_{nb=1}^n a_{nb} \mathbf{u}_{nb}^{t+\delta t} + S u_P \quad (5.34)$$

Equation 5.33 is used to predict the face value of the velocity by isolating the contributions of pressure and density - from the hydrostatic term - when interpolating to the cell face. The contribution of the pressure and density gradients at the face are then added explicitly to  $\mathbf{u}_f$  by calculating them directly from values at the nodes sharing the face. For simplicity the superscript  $t + \delta t$  can be dropped, the face value of velocity is then defined as;

$$\mathbf{u}_f = \left( \frac{\mathbf{H}(\mathbf{u})}{a_P} \right)_f - \left( \frac{1}{a_P} \right)_f (\nabla P'' + \mathbf{g} \cdot \mathbf{h} \nabla \rho)_f \quad (5.35)$$

where the face values other than the pressure and density gradients are calculated by using linear interpolation;

$$\left( \frac{\mathbf{H}(\mathbf{u})}{a_P} \right)_f = L_P \left( \frac{\mathbf{H}(\mathbf{u})}{a_P} \right)_P + (1 - L_P) \left( \frac{\mathbf{H}(\mathbf{u})}{a_P} \right)_N \quad (5.36)$$

$$\left(\frac{1}{a_P}\right)_f = L_P \left(\frac{1}{a_P}\right)_P + (1 - L_P) \left(\frac{1}{a_P}\right)_N \quad (5.37)$$

Substitution of  $\mathbf{u}_f$  from equation 5.35 into equation 5.28 gives;

$$\sum_{f=1}^n \left(\frac{1}{a_P}\right)_f \rho_f \mathbf{A}_f \cdot (\nabla P'' + \mathbf{g} \cdot \mathbf{h} \nabla \rho)_f = \sum_{f=1}^n \rho_f A_f \cdot \left(\frac{\mathbf{H}(\mathbf{u})}{a_P}\right)_f \quad (5.38)$$

The terms containing the pressure and density gradients need to take into account the orthogonal and non-orthogonal contributions of the neighbours. This is done by using the over relaxed non-orthogonal decomposition of the face area vector;

$$\begin{aligned} \mathbf{A}_f \cdot (\nabla P'' + \mathbf{g} \cdot \mathbf{h} \nabla \rho)_f &= \mathbf{D}_f \cdot (\nabla P'' + \mathbf{g} \cdot \mathbf{h} \nabla \rho)_f \\ &+ \mathbf{k}_f \cdot (\nabla P'' + \mathbf{g} \cdot \mathbf{h} \nabla \rho)_f \end{aligned} \quad (5.39)$$

The orthogonal contribution for pressure is given by;

$$\mathbf{D}_f \cdot (\nabla P)_f = |\mathbf{D}_f| \frac{P_N - P_P}{|\mathbf{d}_f|} \quad (5.40)$$

and similarly the orthogonal contribution for density is given by;

$$\mathbf{D}_f \cdot (\nabla \rho)_f = |\mathbf{D}_f| \frac{\rho_N - \rho_P}{|\mathbf{d}_f|} \quad (5.41)$$

The non-orthogonal correction for pressure is given by;

$$\mathbf{k}_f \cdot (\nabla P'')_f = \mathbf{k}_f \cdot \left( L_p \left( \frac{1}{V_p} \sum_{f=1}^n \mathbf{A}_f P''_f \right)_P + (1 - L_p) \left( \frac{1}{V_N} \sum_{f=1}^n \mathbf{A}_f P''_f \right)_N \right) \quad (5.42)$$

and the non-orthogonal correction for density is;

$$\mathbf{k}_f \cdot (\nabla \rho)_f = \mathbf{k}_f \cdot \left( L_p \left( \frac{1}{V_p} \sum_{f=1}^n \mathbf{A}_f \rho_f \right)_P + (1 - L_p) \left( \frac{1}{V_N} \sum_{f=1}^n \mathbf{A}_f \rho_f \right)_N \right) \quad (5.43)$$

The non-orthogonal correction is treated explicitly by adding it to the source term to give the required pressure equation;

$$S_P = \sum_{f=1}^n \left(\frac{1}{a_P}\right)_f \mathbf{D}_f \cdot (\nabla P'' + \rho \mathbf{g})_f \quad (5.44)$$

where;

$$S_P = \sum_{f=1}^n \mathbf{A}_f \cdot \left(\frac{\mathbf{H}(\mathbf{u})}{a_P}\right)_f - \sum_{f=1}^n \left(\frac{1}{a_P}\right) \mathbf{k}_f \cdot (P'' + \rho \mathbf{g})_f \quad (5.45)$$

The pressures in equation 5.44 are now defined in terms of a cell and its nearest neighbours and it is now possible to formulate the pressure equation in terms of these values;

$$a_P P_P = \sum_{f=1}^n a_{nb} P_{nb} + S_p \quad (5.46)$$

The velocity at the cell face given by equation 5.35 can be used for the calculation of the conservative mass fluxes,  $\mathbf{F}_f$ ;

$$\mathbf{F}_f = \rho \mathbf{A}_f \cdot \left( \left(\frac{\mathbf{H}(\mathbf{u})}{a_P}\right)_f - \left(\frac{1}{a_P}\right)_f (P'' + \rho \mathbf{g})_f \right) \quad (5.47)$$

## 5.4 Boundary Conditions.

In this section the discrete implementation of the wall, inlet, outlet and symmetry plane boundaries is defined. Figure 5.2 shows a typical control volume

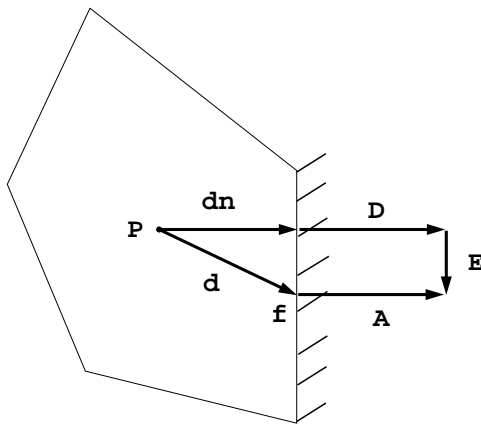


Figure 5.2: Control Volume with Boundary Face.

at a boundary. The outward pointing face area vector  $\mathbf{A}$  is at the centre of the face and  $\mathbf{d}$  is the vector from the cell centre to the centre of the boundary face. The vector  $\mathbf{d}_n$  is the vector from the centre of the cell normal to the boundary face and is given by;

$$\mathbf{d}_n = \frac{\mathbf{d} \cdot \mathbf{A}}{|\mathbf{A}|^2} \mathbf{A} \quad (5.48)$$

#### 5.4.1 Fixed Value Boundary Conditions

This type of boundary is generally used at the inlet where the value of  $\phi_b$  is known and can be used directly in the solution. For example, the discretised convection term in a cell adjacent to a fixed value boundary is;

$$\int_{\Delta V} \nabla \rho u \phi = \sum_{f \neq b} \mathbf{F}_f + \mathbf{F}_b \phi_b \quad (5.49)$$

where  $\mathbf{F}_f$  is the cell face flux. The last term in the above equation may be calculated explicitly and is added to the source term. For the diffusion terms;

$$\int_{\Delta V} \nabla \cdot \rho \Gamma \nabla \phi dV = \sum_f (\rho \Gamma)_f D_f \cdot (\nabla \phi)_f \quad (5.50)$$

For the face boundary, the face gradient is calculated from;

$$\mathbf{D}_f \cdot (\nabla \phi)_f = |\mathbf{D}_f| \frac{\phi_b - \phi_P}{|\mathbf{d}_n|} \quad (5.51)$$

which may be split into an implicit and explicit part.

$$|\mathbf{D}_f| \frac{\phi_b - \phi_P}{|\mathbf{d}_n|} = |\mathbf{D}_f| \frac{\phi_b}{|\mathbf{d}_n|} - |\mathbf{D}_f| \frac{\phi_P}{|\mathbf{d}_n|} \quad (5.52)$$

#### 5.4.2 Fixed Gradient Boundary Conditions

With a fixed gradient boundary condition, the component of the gradient of  $\phi$  normal to the cell face is known. The value of  $\phi$  at the boundary can be obtained from;

$$\phi_b = \phi_P + \frac{\mathbf{d}_n}{|\mathbf{d}_n|} (\nabla \phi)_b \quad (5.53)$$

where  $(\nabla \phi)_b$  is the specified gradient.

For the diffusion term the term containing the gradient at the boundary face reduces to;

$$\mathbf{D}_f = |\mathbf{D}_f| (\nabla \phi)_b \quad (5.54)$$

#### 5.4.3 Wall Boundary Conditions

The treatment of the no-slip condition, i.e the condition where velocity at the wall is zero, at wall boundaries depends on whether the flow is laminar or

turbulent. In laminar flow the velocity at the wall is set to zero and the wall shear stress, included in the momentum equation as a source term, is calculated from the straightforward assumption that the velocity varies linearly from the wall to the nearest cell node;

$$\tau_w = \mu \frac{\mathbf{u}_p}{\Delta y} \quad (5.55)$$

where  $\tau_w$  is the wall shear stress and  $\mu$  is the dynamic viscosity and  $\Delta y = |\mathbf{d}_n|$  the normal distance of the cell node from the wall.

In a turbulent flow field, the high Reynolds number k- $\epsilon$  model can not reproduce the near wall boundary layer behaviour accurately. The turbulent boundary layer velocity gradient near the wall is far steeper than found in the laminar condition and the wall shear stress correspondingly higher, a laminar velocity profile will not reproduce the magnitude of this wall stress. In addition, the boundary layer structure is more complicated, immediately adjacent to the wall there is a thin laminar sub-layer followed by the buffer layer and the fully turbulent region. The number of cells needed to fully resolve this layer is large, however, such detail is not necessary in order to simulate the near wall flow field found in settling tanks. In this study wall functions are used to bridge the region from the nearest node to the wall with the turbulent boundary layer simulated as two layers at the expense of the buffer layer. The cells adjacent to the wall are treated according to whether the cell node is in the laminar or turbulent region of the boundary layer. This is determined from the local value of the dimensionless distance from the wall  $y^+$  which is defined as;

$$y^+ = \frac{\Delta y \rho}{\mu} \sqrt{\frac{\tau_w}{\rho}} \quad (5.56)$$

where  $\Delta y$  is the normal distance of the cell node from the wall, and  $\tau_w$  is the wall shear stress. The log-law of the wall is given by;

$$u^+ = \frac{1}{\kappa} \ln E y^+ \quad (5.57)$$

where  $\kappa$  is the Von Karman's constant with a value of 0.4187, and  $E$  is dependent on the wall roughness which for smooth walls has a value of 9.793. In the above equation, the intersection between the laminar sub-layer and the turbulent region of the boundary layer is generally taken to occur at  $y^+ = 11.63$ . If  $y^+ \leq 11.63$  then the near wall cell node is in the laminar region and the wall shear stress is given by equation 5.55. For  $y^+ > 11.63$  then the cell node is in the turbulent region and the shear stress is given by;

$$\tau_w = \frac{C_\mu^{1/4} k_p^{1/2} \mathbf{u}_p \kappa}{\ln E y^+} \quad (5.58)$$

where  $k_p$  is the turbulent kinetic energy at the cell node. The shear force on the wall is given by;

$$F = \tau_w A \quad (5.59)$$

where  $A$  is the area of the cell wall.

Wall boundary conditions also need to be imposed on the  $k$  and  $\epsilon$  equations. For the  $k$  equation the sink term  $\rho \epsilon$  is replaced by;

$$\rho \frac{C_\mu^{3/4} k_p^{3/2} u^+}{\Delta y} \quad (5.60)$$

The wall boundary condition for  $\epsilon$  follows the assumption that turbulence production equals dissipation which implies that the value of  $\epsilon$  is given by;

$$\epsilon = \frac{C_\mu^{3/4} k_p^{3/2}}{\kappa \Delta y} \quad (5.61)$$

## 5.5 Solution Algorithm.

The equations of motion and state are solved by the segregated approach, where the equations are solved sequentially by iterating over them. The velocity and pressure are coupled by the PISO algorithm which was specially developed for the computation of unsteady compressible flows, detailed descriptions of its implementation can be found in Verteeg and Malalasekera (1995) and Ferziger and Perić (1996). A concise summary of the method was presented by Ubbink (1997) and is reproduced here;

- **Momentum Prediction:** The momentum equation 5.29 is solved firstly with a guessed pressure field  $P^*$ , normally the pressure field of the previous time step. The solution of the momentum equation gives a new velocity field  $\mathbf{u}^*$  which does not satisfy the continuity condition.

- **Pressure Solution:** The predicted velocities  $\mathbf{u}^*$  are used to assemble  $\mathbf{H}(\mathbf{u}^*)$ , equation 5.34, which is needed for the pressure equation (5.46). The solution of the pressure equation gives rise to a new pressure field,  $P^{**}$ . For non-orthogonal meshes the source term, equation 5.45, is updated and a more accurate solution of the pressure equation is obtained. If necessary, an iteration over the explicit non-orthogonal terms can be repeated until a pre-defined tolerance is reached.

- **Explicit velocity correction:** Equation 5.47 gives a new set of conservative mass fluxes consistent with the new pressure field. The new pressure field is used to give an explicit velocity correction. The new velocity  $\mathbf{u}^{**}$  is now consistent with the new pressure field.

The cell centre velocity is given by equation 5.33 so that the velocity depends not only on the pressure gradient but also on  $\mathbf{H}(\mathbf{u})$ , which includes contributions from neighbouring cells. The PISO algorithm uses  $\mathbf{u}^{**}$  to calculate  $\mathbf{H}(\mathbf{u}^{**})$ . This gives rise to  $P^{***}$  which in turn is used to calculate  $\mathbf{u}^{***}$ . This iteration over the last two steps continues until a pre-defined tolerance is

met.

## 5.6 Conclusions

The finite volume discretisation of the governing equations given in Chapters 3 and 4 has been presented in this chapter. The discretisation of convective, diffusive and source terms on an unstructured mesh with an arbitrary number of cell faces has been shown together with the two differencing schemes for the convective fluxes - both of which are used in the settling tank simulations shown in latter chapters.

In buoyancy dominated problems the standard procedure used to calculate pressure on a co-located mesh leads to inaccuracies in the pressure and velocity fields. A modification to the standard procedure used for assembling the pressure equation has been shown. This procedure involves a separate treatment for the hydrostatic pressure which is extracted from the piezometric pressure. The density gradient at the cell face, needed in the calculation of the hydrostatic pressure, is then evaluated from the nodal values either side of it.

The validity of this approach in predicting the pressure is demonstrated in the next Chapters where the numerical model is applied to a number of model scale and full scale simulations and the results compared with experimental results.

# Chapter 6

## Model Scale Simulations.

In the next two Chapters the drift flux model, with shear thinning rheology and the buoyancy modified  $k-\epsilon$  turbulence model described in Chapters 3, 2 and 4 respectively are applied to a number of test cases. In Chapter 6 comparisons are made with the velocity history of a dense incursion, gathered from a lock exchange experiment by Larsen(1977). Later in this chapter comparison is made with velocity and concentration data gathered in a model scale settling tank by Dahl(1993). In Chapter 7, simulations of a full scale settling tank are carried out and compared with velocity and concentration data gathered by Ueberl(1995). Conclusions regarding the predictive accuracy of the methodology are also presented in this chapter.

### 6.1 The Lock Exchange Experiment.

This section deals with the 2D simulation of a lock exchange experiment carried out by Larsen(1977), in order to determine the density of activated sludge in suspension. Density differences as small as one part in 1,000 can be determined to better than five percent accuracy by this method, Witherage and Wilkinson (1989). It is particularly useful for evaluating the negative buoyancy of particle and floc suspensions whose densities are difficult to determine to

similar accuracy by direct weighing.

In the experiment, the speed of the density current or dense incursion was measured for different concentrations of activated sludge. From the speed of the incursion it is possible to calculate the density from equation 6.2.

In the numerical simulation, the experimentally determined density and concentration of the dispersed phase were used as initial conditions for the activated sludge mixture. The speed of the incursion generated by this excess density was then determined and compared with the experimental results.

It is also possible to gain qualitative insight from the calculations into the effects of Bingham plastic rheology and turbulence on the speed and dissipation rate of the incursion. Similarly, the effects of carrying out the simulation in two or three dimensions can be compared.

### 6.2 Experimental Procedure.

In the experiment a perspex flume 4m long, 0.3m wide and 0.25m deep was divided by a partition, Figure 6.1. One side of the tank was filled with activated sludge from an aeration tank, the other side was filled to the same level with clear effluent from the corresponding settling tank.

Upon removal of the partition, the top and bottom fronts accelerate to their maximum velocity. As the front progresses, its speed is gradually reduced due to settling and frictional effects. The latter can be characterised by the densimetric Reynolds number, Witherridge and Wilkinson (1989), given by;

$$R_d = \frac{\left(\frac{\Delta\rho}{\rho}gH^3\right)^{0.5}}{\nu} \quad (6.1)$$

Here  $R_d$  is the densimetric Reynolds number,  $H$  is the depth of the fluid in the tank,  $\Delta\rho$  is the difference in relative densities of the fluids either side of the partition,  $g$  is the gravitational acceleration and  $\nu$  is the kinematic viscosity of the mixture.

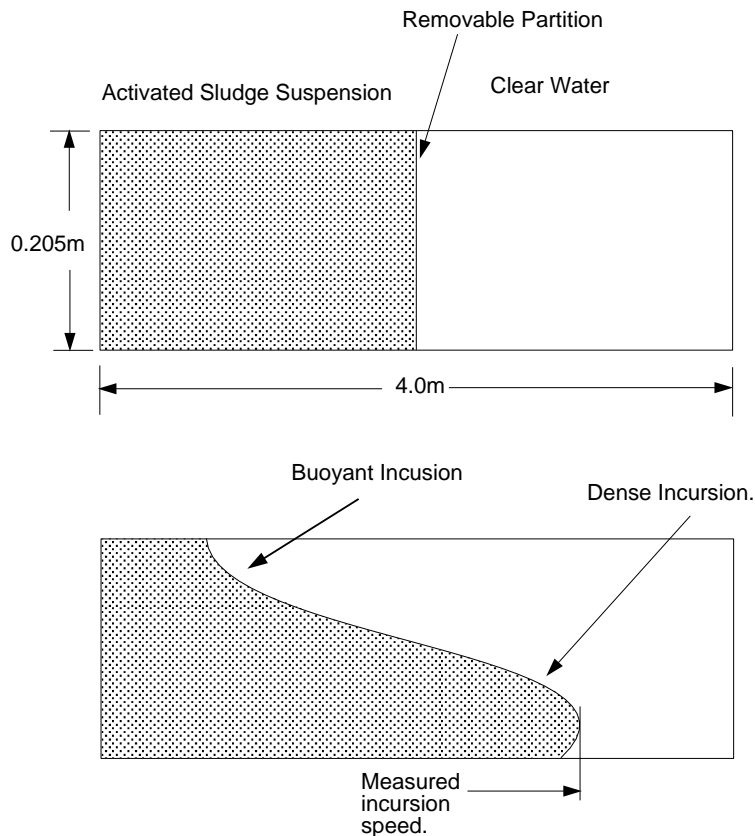


Figure 6.1: Schematic of Lock exchange Experiment.

It was found, Barr (1963), that the effects of friction on the speed of the intrusion are most pronounced at  $R_d$  below 500. With both the experiment and the later simulations,  $R_d$  is not constant due to changes in viscosity of the mixture brought about by settling and shear thinning. However, for the purposes of determining the excess density of the activated sludge mixture the maximum velocity is used because this is achieved before viscous effects become dominant.

Another limitation of the technique is that the evaluation of the dispersed phase density using equation 6.2 is only valid when the effects of settling on the mixture are negligible, i.e. when the terminal velocity of the particles is some orders of magnitude less than the incursion velocity, so that particles remain in suspension during the course of the experiment. In this particular case the settling velocity is at least an order of magnitude less than the maximum incursion velocity from which the density is evaluated. The relationship between density difference and incursion speed is given by Larsen (1977);

$$U = 0.5 \sqrt{\frac{\Delta\rho}{\rho} gh} \quad (6.2)$$

In the experiment wave speed was found by measuring the time taken for the front to travel between equidistant marks.

Fourteen experiments using different concentrations of activated sludge were carried out. In the case considered here the depth of fluid in the tank was 0.205m with an activated sludge density of  $1450\text{kg/m}^3$ , as calculated by equation 6.2, and a measured initial solids fraction of 0.0033 was used.

### 6.3 Numerical Simulation.

A 200 by 50 grid was used for the 2D simulation, and a 200 by 50 by 10 grid for the 3D case. In the latter, half the tank width was modelled, with a symmetry

plane placed at the center of the tank.

For the turbulent cases, an initial turbulent intensity of 3% was assumed in both parts of the tank. This initial turbulence can be considered to have been generated by stirring before the removal of the dividing partition.

The Gamma spatial discretisation scheme of Jasak (1996), section 5.3.1, was used for the convective terms in both the mixture momentum equation 3.40 and the solids fraction equation 3.39 for the dispersed phase, in order to reduce the numerical diffusion at the interface between the activated sludge mixture and the lighter fluid. In the numerical simulation the incursion speed was found by measuring the distance traveled in a given time by the dense front. Its position was taken to be at the median value of the solids fraction, i.e 0.0016.

### 6.3.1 The Physical Properties of Activated Sludge.

In section 2.5 it was shown that sewage sludge exhibits Bingham Plastic behaviour. Two quantities need to be specified in order to characterise this rheology, namely the yield stress,  $\tau_y$ , and the plastic viscosity,  $\eta$ . A constitutive relationship for settling velocity, section 2.4, is also needed in order to carry out numerical simulations with the Drift Flux model.

Yield stress and plastic viscosity vary with concentration. Various authors as reviewed by Casey(1983), have formulated exponential relationships for these quantities. They have the general form;

$$\Phi = aC^{b\alpha} \quad (6.3)$$

where  $\Phi$  is the physical property in question,  $\alpha$  is the solids fraction and  $a$  and  $b$  are constants. The exponentstet,  $C$ , is generally the natural logarithm base e, or the base 10 which is used in this study.

In the experiments selected for analysis in this thesis, only Dahl (1993), as described later in section 6.4, measured settling velocity. Yield stress and

plastic viscosity were not measured. Dahl used equation 6.3 to calculate these quantities in his numerical simulation of the experimental settling tank. It was shown that the exponents used in this relationship varied with the inlet concentration of activated sludge: however, the reason for this is not known.

In the lock exchange experiment, Larsen (1977), and the full scale settling tank experiment, Uberl (1995) Chapter 7, settling velocity, yield stress and plastic viscosity were not measured. For the purposes of the present numerical simulation, equation (6.3) has been used to estimate these unmeasured physical properties in these latter two experiments, in a similar fashion to Dahl.

The values of  $a$  and  $b$  used in the simulation of the Dahl case with an inlet void fraction of 0.002, section 6.6.8, were used to calculate the physical properties for the Larsen (1977) and Uberl (1995) numerical simulations. In the latter two cases the exponent,  $b$ , used in the general formulae was multiplied by the ratio of inlet concentration of the Dahl case,  $\alpha = 0.002$ , to the inlet or initial concentration of the case being studied,  $\alpha_{in}$ . The the resulting formulae has the form;

$$\Phi = aC^{\frac{\alpha_{in}=0.002}{\alpha_{in}}b\alpha} \quad (6.4)$$

The exponent from the experimentally derived settling velocity was also adjusted in this way. This essentially scales the physical properties of the sludge used in the Dahl(1993) case for the other two experiments. The results are summarised in Table 6.1

Property $\Phi$	Coefficient a	Exponent b
Yield Stress	5.5469E-5 kg/(m.s <sup>2</sup> )	573.04
Bingham Viscosity	2.3143E-4 kg/ms	107.98
Settling Velocity	-2.1980E-3 m/s	172.19

Table 6.1: Coefficients of Equation 6.3 used for Sludge Property Estimation for the Larsen Experiment.

### 6.3.2 Results.

Four numerical simulations were carried out as follows;

- a) 2D Laminar flow with settling only and constant laminar viscosity.
- b) 2D Laminar flow with settling and Bingham plastic rheology.
- c) 2D Turbulent flow with settling and Bingham plastic rheology.
- d) 3D Turbulent flow with settling and Bingham plastic rheology, as (c) above.

The predicted incursion speeds for each of the four cases are compared with the data in Figure 6.2. The irregularity of the numerical simulation curves is due to slight inaccuracies in determining the exact position of the interface at a given time.

The experimental results indicate that the dense incursion reaches a maximum velocity at about 7 seconds which it maintains for about 15 seconds. Thereafter, the velocity falls in an almost linear fashion until about 65 seconds after which it levels out to a low but constant value. It can be observed that the maximum velocity is reasonably well reproduced in all cases but with errors of up to 8% in **case b)** and **c)**.

For **case a)**, (settling only), the velocity decays slightly from the maximum at about 20s but does not fall further during the course of the experiment. This behaviour is similar to the result obtained by Witherridge and Wilkinson

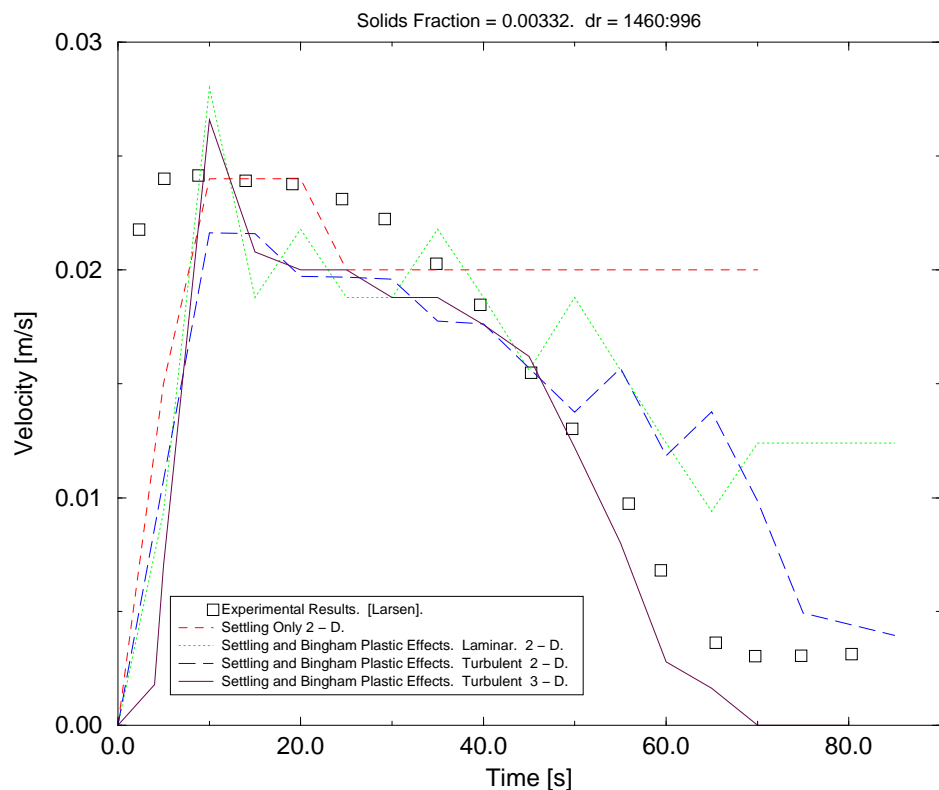


Figure 6.2: Interface Velocity - Lock Exchange Experiment.

(1989) for a non-settling dispersed phase: in their case a brine solution was used on one side of the tank and fresh water on the other. They found that starting transients dissipated by the time the incursion had traveled a distance equal to the depth of the tank and thereafter the velocity of the incursion remained constant.

The results of the simulation indicate that for the given activated sludge settling velocity, settling alone will not cause a substantial reduction in the speed of the density current.

Introducing Bingham Plastic effects into the rheology of activated sludge suspension, **case b**), reduces the velocity of the density current through the course of the simulation. Introducing the effects of turbulence, **case c**), produces further reduction as the experiment proceeds.

In the 3D simulation, **case d**), all features of the model are operational and this simulation produces a velocity history of the density current most closely resembling the measurements. The peak velocity is over predicted by about 10% with the final nearly constant calculated level is around 10 - 15% less than that found in the experiment. The best agreement occurs in the decay phase at a round 45 - 55 seconds. In the simulation the velocity decays to zero at 70 seconds whereas the experiment shows the current to continue past the 80 second point.

Velocity vector plots taken from the 3D simulation at 10s, 35s and 50s are shown in Figures 6.3 to 6.5. The corresponding solids fraction distributions are illustrated in Figures 6.6 to 6.8. The plots illustrate a 1m section of the tank which extends from the location of the partition wall, i.e the center of the tank. Figure 6.4 shows that the velocity of the density current near the floor of the tank is reduced to zero by the high viscosity of the settled sludge layer. As the front moves along the tank the velocity of the fluid in the main body of the current is reduced. As this reduction in velocity continues, most of the new material is carried to the leading edge of the incursion by the higher

velocity fluid at the interface between the dense incursion and the ambient fluid - i.e the fluid at the top of the dense incursion. These effects are most clearly illustrated in Figure 6.5.

Another feature illustrated in Figure 6.5, is the development of a vortex at the leading edge of the density current. This is a well-known transient effect associated with many buoyant and wall jet type flows. Material from the leading edge is thus picked up and deposited back into the density current. This is illustrated in the solids fraction plot, Figure 6.8.

Vector plots for transverse sections across the tank at 0.80m, 0.83m and 0.85m from the location of the partition wall are shown in Figures 6.9 to 6.11. The sections where all taken at  $t = 50$ s and they all pass through the vortex. It can be observed that secondary flows are present, but no distinct structure or pattern can be discerned. Transverse flows are absent in the fully developed section of the dense incursion upstream of these locations.

An isosurface of the median value of solids fraction (i.e  $\alpha = 0.00166$ ) at  $t = 50$ s, together with iso-contours of solids fraction is illustrated in Figure 6.12, which shows a section of the tank extending 1m either side of the location of the partition. Both the dense and buoyant incursions can be seen and the leading edge of each incursion is different. The neutrally buoyant incursion does not have the leading edge vortex and is smoother in appearance. It can also be observed that the near side wall of the tank has produced a distinct kink in the leading edge vortex. This is due to frictional effects slowing down the density current near the wall.

### 6.3.3 Conclusion.

The results demonstrate that the present model can adequately reproduce the velocity history of a dense incursion in a lock exchange experiment.

The region of peak velocity is governed mainly by buoyancy forces, generated in this experiment by the density difference between the fluids on either

side of the partition. The model can reproduce the velocity generated by this buoyancy force to a good degree of accuracy. It was observed that settling alone did not contribute significantly to the decay of the density driven current. The ratio of the momentum of the dispersed phase to the momentum of the continuous phase per unit volume is very low, about 0.004:1, hence, when the dispersed phase settles little momentum is actually transferred out of the density current.

Bingham plastic rheology and turbulence have very significant effects in causing the decay of the density current. Three dimensional effects also significantly affect the decay of the density current. These effects will be discussed more fully in Chapter 7. The Bingham viscosity, yield stress and settling velocity were not measured in the experiment so a general expression with coefficients scaled by the initial void fraction was used for these variables in the simulation, see Table 6.1. It is reasonable to assume that had values of these variables been measured from the sludge used in the lock exchange experiment, closer agreement between the simulation and the experiment would have been found.

In the next section the model is further assessed using data from a large scale, more detailed experiment with conditions similar to those found in a full scale settling tank.

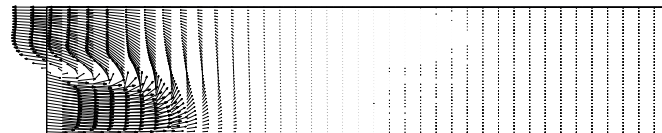


Figure 6.3: Mixture Velocity, Vector Field. 10s

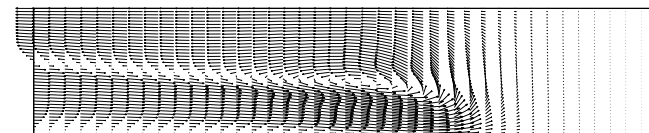


Figure 6.4: Mixture Velocity, Vector Field. 35s

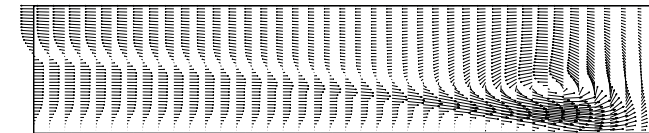


Figure 6.5: Mixture Velocity, Vector Field. 50s

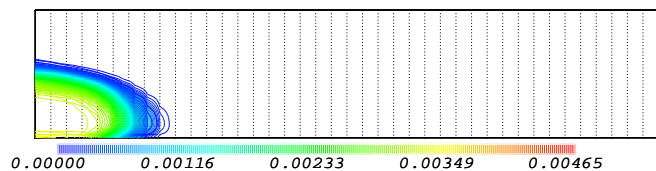


Figure 6.6: Solids Fraction.10s

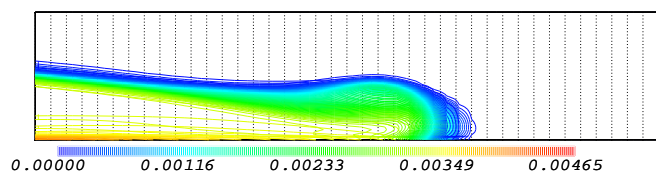


Figure 6.7: Solids Fraction.35s

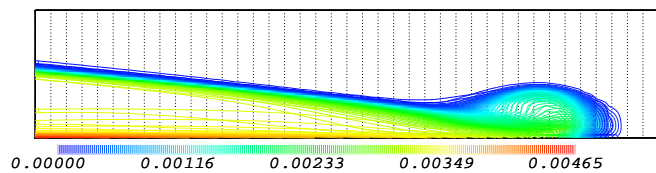
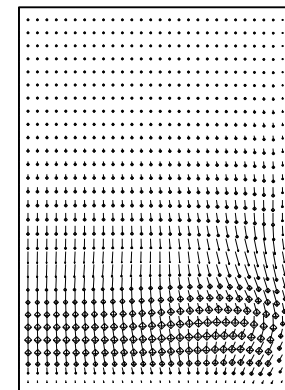
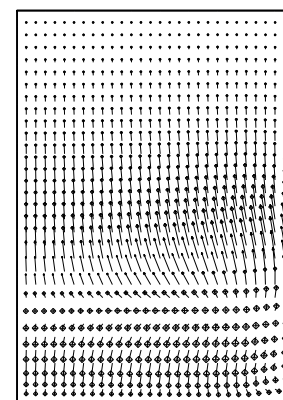
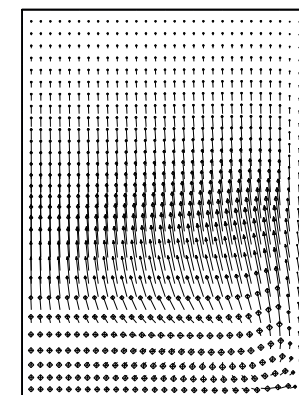


Figure 6.8: Solids Fraction.50s

Figure 6.9: Secondary Flow 0.80m.  
t = 50s.Figure 6.10: Secondary Flow 0.85m.  
t = 50s.Figure 6.11: Secondary Flow 0.87m.  
t = 50s.

## 6.4 The Dahl Experiment.

In this section the present method is applied to simulate a large experimental settling tank constructed at the Aalborg wastewater treatment plant in Denmark, Dahl (1993). It was set up to produce similar flow field conditions, in terms of inlet velocities and concentrations and through-flow velocities and concentrations, to those found in a full scale tank.

In the experiments, mixture velocity and solids concentration were measured in the free stream and in the sludge blanket. The measurements were taken at three measuring stations along the tank test section and at two distinct time periods; the first period of around 1000s, whilst the sludge blanket was accumulating and the second period, of around 7000s, when the sludge blanket had reached an approximately equilibrium height. The experiment was designed to produce a 2D flow field and the simulations presented here are 2D. However, integration of the experimental velocity profiles demonstrates that the volumetric flow rate is not constant, this may be caused by 3D effects or variations of inlet flow rate with time or both. Two inlet geometries, each with two different inlet velocities and concentrations, were studied.

There are advantages in carrying out experiments on a tank of this kind. The influent volumetric flow rate and dispersed phase concentration can generally be controlled more accurately than in a full scale tank. Similarly, velocity and concentration profiles can be measured with more accuracy, simply by virtue of the fact that the test section is of a more manageable scale.

Comparison with these experimental data allow all the features of the model, most obviously the ability to predict the velocity of the density driven current and the concentration of the dispersed phase in both the settled sludge layer and the free stream, to be tested. Other features of the model, such as the rheological behaviour, can be assessed indirectly by comparing the depth and rate of deposition or erosion of the sludge blanket with the experimental

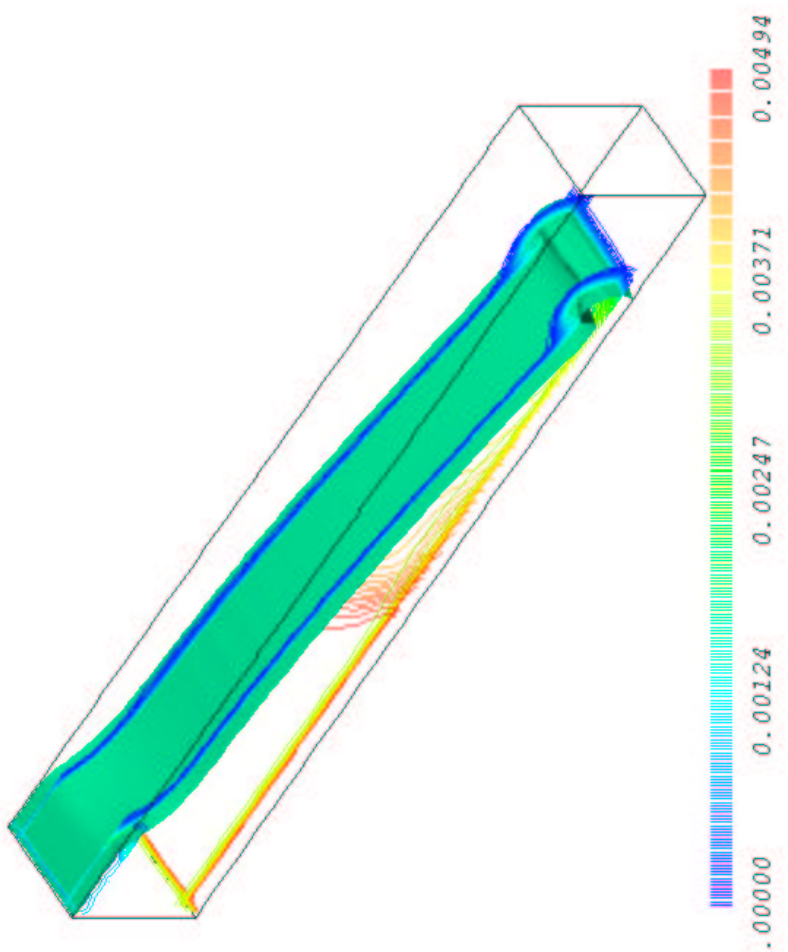


Figure 6.12: Isosurface of Median Value of Solids Fraction.  $t = 50\text{sec}$ .

results.

The tank is a less accurate representation of the flow field in a full scale tank in respect of the ratio of the depth of the settled sludge layer to the depth of the tank. In the experiment, this ratio is generally much larger than found in full scale tanks, reaching over 50% in some experiments. A sludge blanket of this depth is a severe test of both the accuracy of the model and its numerical stability because there are large, stagnant, highly viscous areas in the test section for practically the entire duration of the experiment. As will be shown, the model acquires itself well under these conditions.

#### 6.4.1 Physical Properties of Activated Sludge

The physical properties of yield stress and plastic viscosity which characterise the Bingham Plastic rheology of activated sludge were not measured, so an empirical relationship, equation 6.3, was used to calculate these properties from the solids fraction. The exponents so deduced for each void fraction are given in Table 6.2

Property $\Phi$	Constant a Both Cases	Exponent b	
		$\alpha_{in} = 0.001$	$\alpha_{in} = 0.002$
Yield Stress	5.5469E-5 kg/(m.s <sup>2</sup> )	1050.80	951.25
Bingham Viscosity	2.3143E-4 kg/ms	179.26	179.26
Settling Velocity	-2.198E-3 m/s	285.84	285.84

Table 6.2: Coefficients of Equation 6.3 used for Sludge Property Estimation for the Dahl Experiment.

## 6.5 Experimental Apparatus.

The experimental settling tank has a test section 7.5 to 7.9m long, 1m wide and 1m deep as illustrated in Figure 6.13. The activated sludge solution is

fed to the inlet by a siphon conduit system and flow rate is controlled by feed valves.

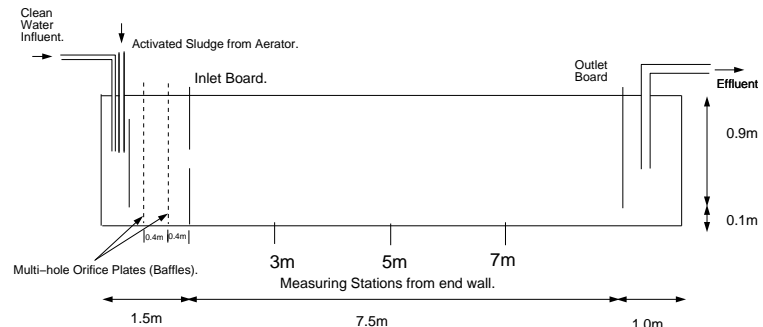


Figure 6.13: Schematic of Albourg Settling Tank.

The suspended sludge concentration of the influent was controlled by mixing clean effluent water from the wastewater treatment plant with the sludge solution upstream of the inlet, Dahl (1993). Two perforated plates produced mixing and established a uniform flow field before the mixture enters the test section.

Two inlet designs were used in the experiment. In the first, the mixture was allowed directly into the test section from the second perforated plate. The other design had an inlet board located 0.4m downstream of the last perforated plate. This had a slot 0.15m in depth running the full width of the tank. The bottom edge of the slot is situated at half of the depth of the tank.

The outlet to the test section was a full width slot 0.1m high at the bottom of the outlet board, from there the effluent was pumped back to the aeration tank. The effluent flow rate was controlled by a valve and adjusted to match the desired influent flow in order to keep the water depth constant during the experiment.

### 6.5.1 Experimental Procedure

Measurements of velocity and dispersed phase concentration were taken along the center plane of the test section at distances of 3.0m, 5.0m and 7.0m from the inlet end wall. Integration of the velocity profiles to give the volumetric flux through each station at the experimentally recorded times shows variation from the claimed influent volume. This indicates the existence of a time varying volumetric flow rate, or three dimensional effects, or both.

The mixture velocity was measured by an electro-magnetic induction sensor and the suspended sludge concentration was measured by an optical turbidity meter.

Experimental data for the following four sets of conditions were chosen for comparison with the computational model;

- i) No inlet board, influent flow rate 19.1 l/s and solids fraction 0.001.
- ii) As i) but with a flow rate of 5.4 l/s and solids fraction of 0.00215.
- iii) With the inlet board in place and a flow rate of 5.2 l/s, solids fraction 0.001.
- iv) As iii) but with a flow rate of 12.0 l/s and solids fraction of 0.002.

## 6.6 Numerical Simulation.

In each of the simulations, the computational domain was initialised with a uniform solids fraction concentration equal to the influent value and the velocity field was initialised to the mean tank through flow velocity. All the simulations were carried out as transient calculations with upwind differencing used on all convective terms in the model.

Turbulent intensity at the inlet was not measured in the experiment. Numerical experiments indicated that the flow field within the tank is largely independent of the influent turbulent intensity within the range 1 to 20%, a nominal 10% inlet turbulent intensity was imposed.

The development of the flow field for all four numerical simulations followed broadly similar lines. A sludge blanket is formed almost immediately as settling increases the concentration of activated sludge on the tank floor, the nominal tank through flow velocity being too low to scour this sediment. No buoyancy effects are observed initially at the inlet because the influent and the fluid in the tank have the same density. Fluid moves from the inlet to the outlet with the mean through flow velocity, except near the floor.

As time goes by material settling out from the bulk of the fluid causes this bulk fluid to become less dense than the influent. There is then a ‘collapse’ of the front between the heavier fluid at the inlet and the lighter fluid in the tank. The flow behaviour near the inlet is similar to that found in the lock exchange experiment. A density current develops from the inlet, becoming more pronounced as settling from the main body of the fluid continues.

This density current becomes the dominant flow feature and has approximately the same depth throughout the experiment for all cases. The core value of the solids fraction within the density current is about the same as the solids fraction of the inlet. The viscosity of the settled bed is high enough for the density current to flow over it, depositing more material as it does so and so increasing the depth of the bed.

In the early stages of the experiment, whilst the settled bed is low, large regions of the upper part of the tank above the density current are occupied by one or more recirculation zones. As the settled bed rises the depth of these zones is reduced and they become elongated. The solids fraction in the flow field above the density current is very low, Bingham plastic effects are minimal and the rheology is essentially Newtonian. From these general flow field features we can now look at the each experiments in detail.

### 6.6.1 Cases (i) and (ii) Full Depth Inlet

In this setup the influent emerges directly into the test section from the second perforated plate, giving an essentially uniform velocity profile just downstream.

Successive grid refinement for this case indicated that the solution was changed little for grids finer than 40 by 200 nodes. The results presented in the next section are from this grid.

The boundary conditions are shown in Figure 6.14. A uniform **inlet** velocity profile was specified through the depth of the tank with a uniform solids fraction distribution. A zero gradient outlet boundary was imposed at the **outlet** of the tank. The free surface and sides of the tank were represented symmetry planes - effectively slip surfaces.

The simulation was carried out in the first instance as a single phase calculation with water as the working fluid. The calculation showed that the velocity field was essentially that of open channel flow for most of the tank length, no recirculation zones were present.

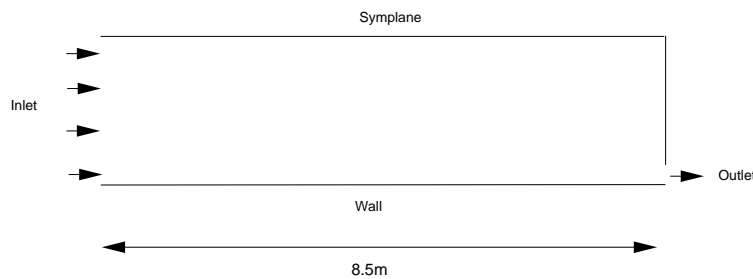


Figure 6.14: Boundary Conditions. Full Depth Inlet.

### 6.6.2 Results Influent Flow Rate 19.1 l/s

In this section the results for an influent flow rate of 19.1 l/s are presented. Table 6.3 shows the times at which the velocity and solids fraction data were

measured. The table also shows the volumetric flow rate obtained by integrating the velocity data. The integration shows significant variation in the volumetric flow rate.

	St 1 (3.0m)		St2 (5.0m)		St3 (7.0m)	
	Velocity	Solids	Velocity	Solids	Velocity	Solids
time t1	900s	600s	2100s	1680s	3180s	3000s
Flow rate	15.25 l/s		21.5 l/s		21.75 l/s	
time t2	7380s	7080s	8400s	8100s	9360s	9060s
Flow rate	15.5 l/s		13.25 l/s		19.0 l/s	

Table 6.3: Experimental Conditions. No Slot Geometry. Flow rate = 19.1l/s. Solids Fraction = 0.001.

The results are presented in the following way; **graphical comparisons** with velocity and solids fraction data at the recorded experimental times are shown in Figures 6.15 and 6.16. These graphs are followed by plots of the **vector field** and contour plots of **solids fraction** presented at times as close to the experimental measurement times as possible. Finally, for this experiment, contour plots of turbulent and laminar viscosity are presented at a time from the later part of the experiment.

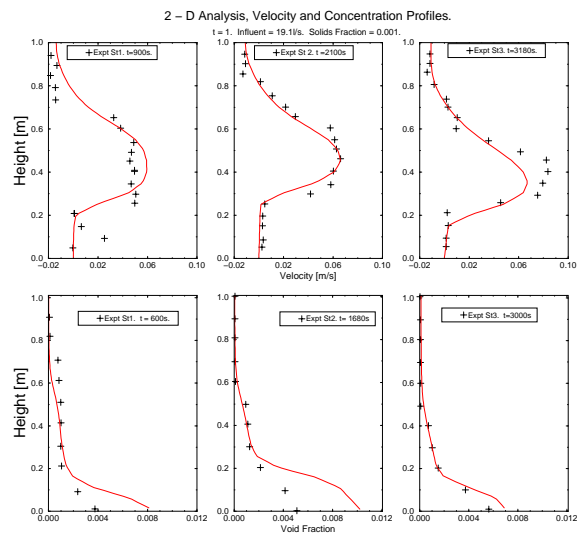


Figure 6.15: Velocity and Solids Fraction Plots, 19.1l/s. Early part of Experiment.

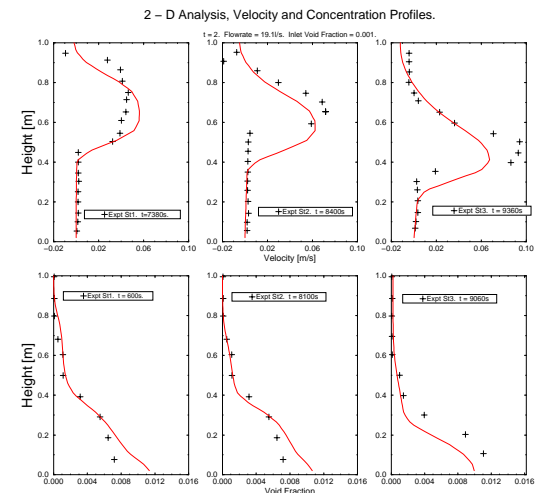


Figure 6.16: Velocity and Solids Fraction Plots, 19.1l/s. Late part of Experiment.

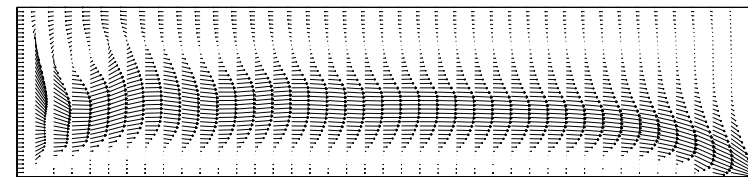


Figure 6.17: Flow rate 19.1l/s. Mixture Velocity, Vector Plot 900s.

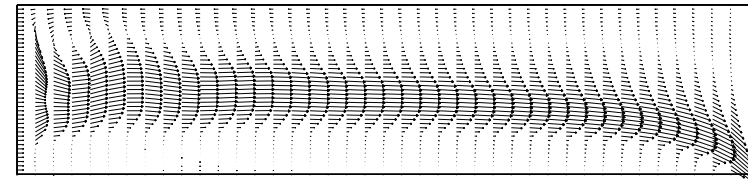


Figure 6.18: Flow rate 19.1l/s. Mixture Velocity, Vector Plot 2100s.

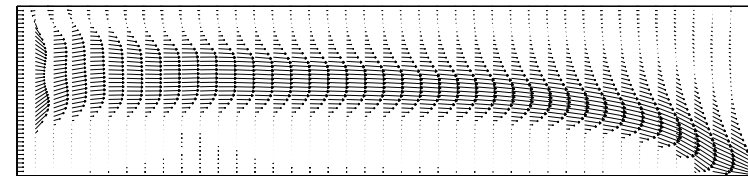


Figure 6.19: Flow rate 19.1l/s. Mixture Velocity,Vector 3200s.

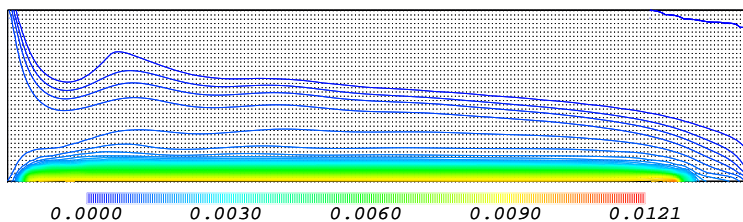


Figure 6.20: Flow rate 19.1l/s. Solids Fraction 600s.

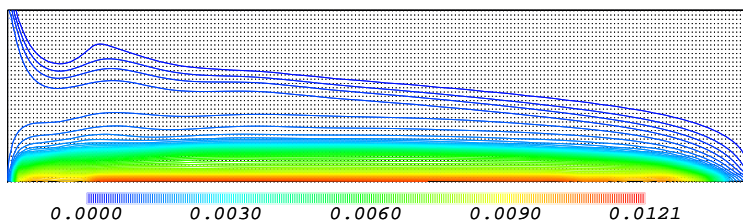


Figure 6.21: Flow rate 19.1l/s. Solids Fraction 1700s.

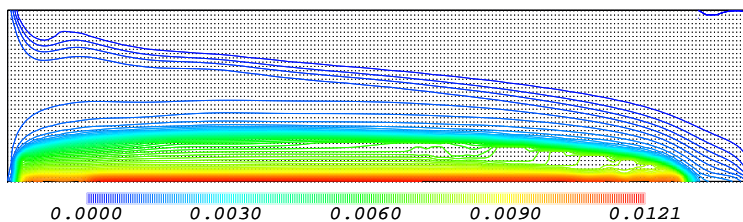


Figure 6.22: Flow rate 19.1l/s. Solids Fraction 3000s.

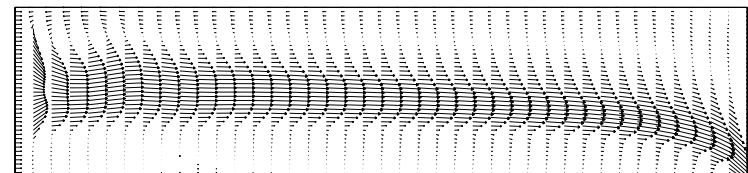


Figure 6.23: Flow rate 19.1l/s. Mixture Velocity, Vector Plot 7400s.

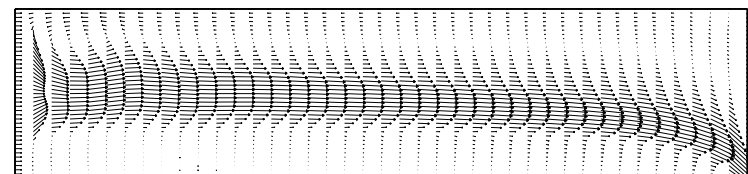


Figure 6.24: Flow rate 19.1l/s. Mixture Velocity, Vector Plot 8400s.

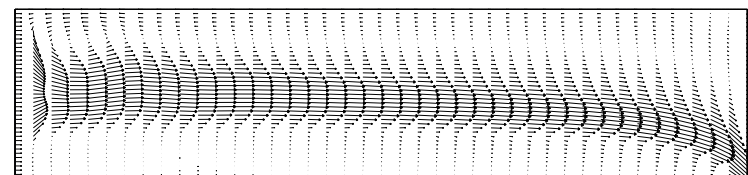


Figure 6.25: Flow rate 19.1l/s. Mixture Velocity, Velocity Vector 9400s.

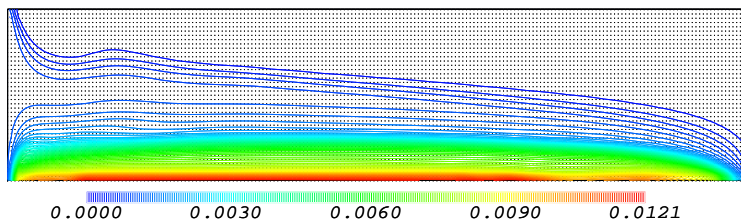


Figure 6.26: Flow rate 19.11/s. Solids Fraction 7100s.

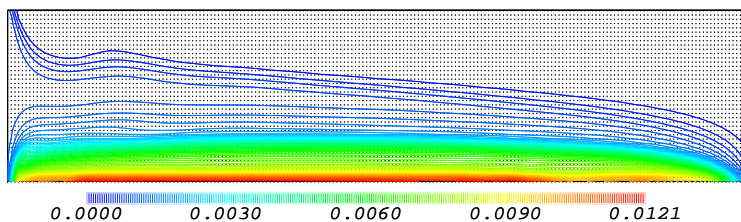


Figure 6.27: Flow rate 19.11/s. Solids Fraction 8100s.

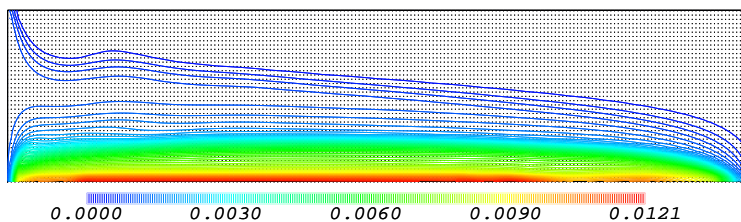


Figure 6.28: Flow rate 19.11/s. Solids Fraction 9100s.

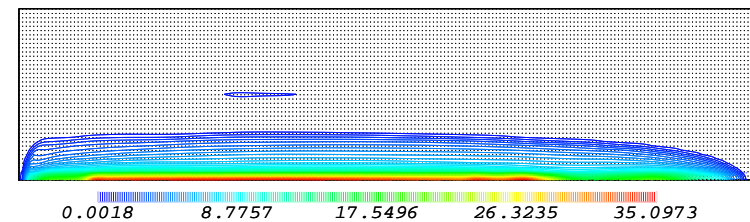


Figure 6.29: Flow rate 19.11/s. Laminar Viscosity 7100s.

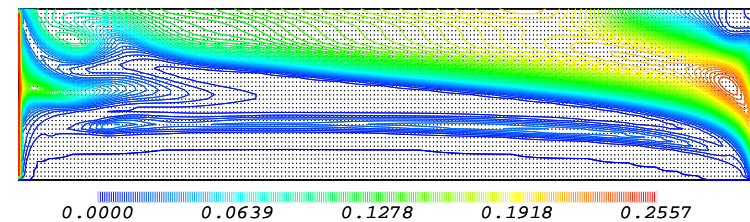


Figure 6.30: Flow rate 19.11/s. Turbulent Viscosity 7100s.

### 6.6.3 Results Influent Flow rate 5.4 l/s

In this experiment with the full-depth inlet, the flow rate is reduced to 5.4 l/s and the influent solids fraction increased to 0.00215. In the calculations a uniform inlet velocity of 0.0054m/s is used with a turbulent intensity of 10%. The flow field in the tank and the solids fraction distribution is very similar to the 19.1 l/s case hence only comparisons of velocity and solids fraction between experimental data and the numerical simulation are presented in Figures 6.31 and 6.32.

	St 1 (3.0m)		St2 (5.0m)		St3 (7.0m)	
	Velocity	Solids	Velocity	Solids	Velocity	Solids
time t1	900s	600s	1860s	1560s	2880s	2580s
Flow rate	4 l/s		3.75 l/s		4.5 l/s	
time t2	7560s	7270s	8460s	8160s	9360s	9060s
Flow rate	4 l/s		4.25 l/s		2.25 l/s	

Table 6.4: Experimental Conditions. No Slot Geometry. Flow rate = 5.4l/s  
Influent Velocity = 0.00541m/s. Solids Fraction = 0.00215.

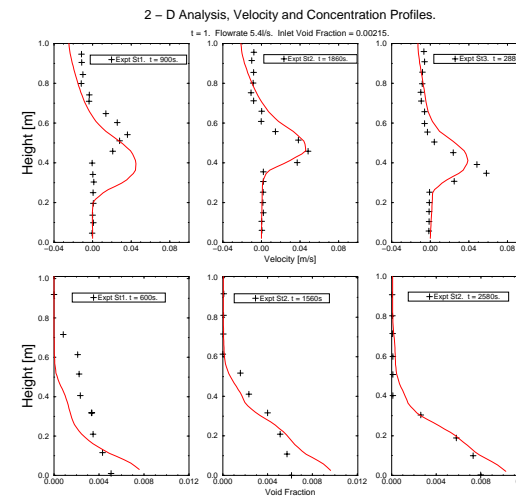


Figure 6.31: Velocity and Solids Fraction Plots, 5.4l/s. Early part of Experiment.

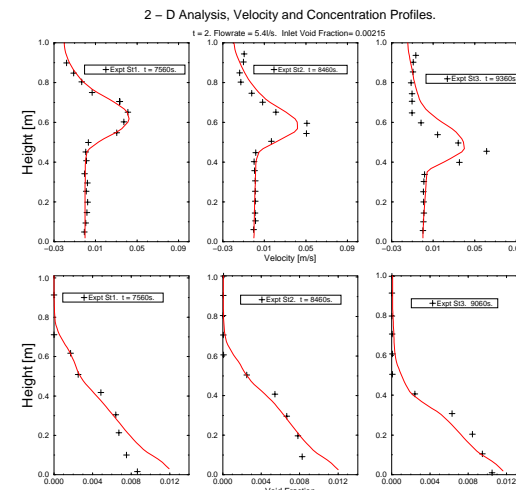


Figure 6.32: Velocity and Solids Fraction Plots, 5.4l/s. Late part of Experiment.

#### 6.6.4 Discussion.

The general shape and velocity of the density current at each station are well predicted with very good agreement at some stations. This is seen in Figures 6.15 and 6.16 for the 19.1 l/s flow rate and Figures 6.31 and 6.32 for the 5.4 l/s flow rate. Where the height of the settled bed at each station is accurately simulated, then the velocities are well predicted. Settled bed height is clearly seen on the velocity profiles: it occupies the transition region from the vertical line of zero velocity to the first recorded measurement in the density current. Maximum velocity in the density current is also well predicted.

In the earlier part of both simulations, the solids fraction in the settled bed tends to be over predicted, particularly near the tank floor. At the later recorded times, the settled bed concentration is more accurately predicted, with good agreement in the mid section of the settled bed region: however, some over prediction is still present at the tank floor. Sudden changes in concentration in the transition region between the settled bed and the density current are well predicted throughout the simulation. This indicates that the consolidation behaviour of the settled bed, predicted using equation (6.1) with coefficients in Table 6.2, is more accurate in the later part of the simulation.

A turbulent viscosity plot taken at 7100s, is shown in Figure 6.30. The plot shows iso-concentration lines in the transition region between the density current and the settled bed. Velocity gradients are high here, and density gradients may not be high enough to completely stifle the generation of turbulence. However, the magnitude of turbulence is very low and whatever is generated here is not convected or diffused into the main body of the density current. (The turbulence behaviour in settling tanks together with the buoyancy modified  $k-\epsilon$  model used in this simulation, was discussed in Chapter 4.)

It can be seen that the initial turbulence is convected into the domain

but is damped at just over 1 inlet depth into the density current. No iso-concentration lines are seen to occupy the core region of the density current itself indicating, from the values either side of this region, that turbulence is uniformly very low here.

At the interface between the density current and the ambient fluid in the settling tank the close spacing of the iso-concentration lines indicates large changes in turbulent intensity gradient above the density current. This is to be expected, as density stratification is reduced in this region whilst velocity gradients are high. A plot of laminar viscosity at 7100s, shown in Figure 6.29, shows that the high levels of laminar viscosity are confined to the settled bed region.

In the next section we look at results from the simulation for two inlet conditions with a slot inlet board geometry.

### 6.6.5 Cases (iii) and (iv) Slot Inlet.

In order to obtain an influent with a more jet like structure, an inlet board with a slot was introduced into the settling tank just downstream of the multi hole orifice plates, see Figure 6.13. With this the test section is reduced in length from 8.65m to 7.5m. The slot is 0.15m in depth and the lower edge is positioned at half the depth of the tank. Two experiments were conducted with this inlet design.

The predicted velocity profiles and solids fraction concentration were seen not to change appreciably with a grid finer than of about 40 by 200 nodes. The 2D computational domain shown for the simulation with a slot inlet, Figure 6.33, is of 23 by 100 nodes.

The boundary conditions are shown in Figure 6.34. A uniform **inlet** velocity profile was specified with a uniform solids fraction distribution. The turbulence intensity was set to 10% at the inlet with the mixing length set to half the height of the inlet slot width.

A zero gradient outlet boundary was used to simulate the **outlet** of the tank. The free surface and sides of the tank were given slip boundary conditions, as with the cases with the open inlet geometry.

### 6.6.6 Slot Inlet - Single Phase Analysis.

A single phase analysis was carried out on this tank using water as the working fluid. A vector plot of the flow field is shown in Figure 6.35. Previously, experimental velocity and turbulence intensity data was obtained from a tank with this type of inlet geometry by Stamou(1988). This tank test section was 0.17m by 2.5m and the experiment was conducted at a Reynolds number of 2018. A numerical simulation of the flow field for this experiment was carried out and the results compared with the measurements.

In the single phase flow regime, both the simulation and the experiment

demonstrated that the inlet region of the tank was dominated by two recirculation zones. The larger of these is near the floor of the tank as shown in Figure 6.35. Two  $k-\epsilon$  turbulence models were compared in the numerical simulation namely the standard model and the RNG variant, Speziale (1991). It was seen that the RNG model is more accurate in predicting the length of the recirculation zones. Both models failed to predict the peak magnitude of turbulent intensity in the shear layer either side of the influent jet. Further downstream, turbulent intensity was well predicted by both models. Velocity was well predicted at all stations.

A single phase analysis does not reproduce the flow field features associated with a negatively buoyant influent into a geometry of this kind. Once buoyancy forces are introduced, the velocity field is radically altered, the jet structure collapses very quickly with the lower recirculation zone being replaced by the density current running along the floor of the tank. Multiple recirculation zones are formed above the density current. As well as this, turbulence is suppressed by density stratification.

In the two phase simulation with a slot, two inlet conditions were examined;

- 1) A volumetric flow rate of 5.2l/s with an influent solids fraction of 0.001.
- 2) A volumetric flow rate of 12.01l/s with an influent solids fraction of 0.0022.

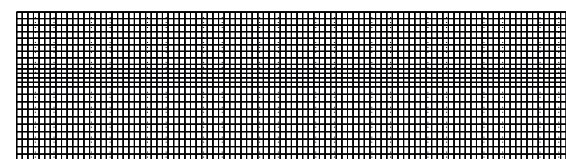


Figure 6.33: Computational Domain. Slot Inlet. Scaled 2x Vertically.

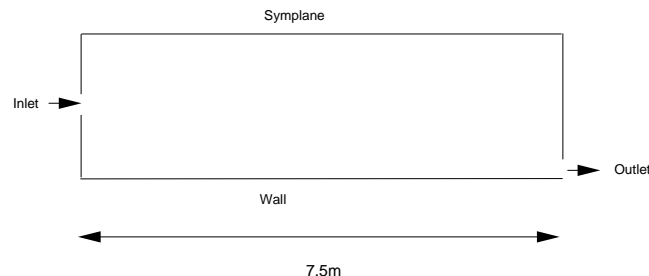


Figure 6.34: Boundary Conditions. Slot Inlet.

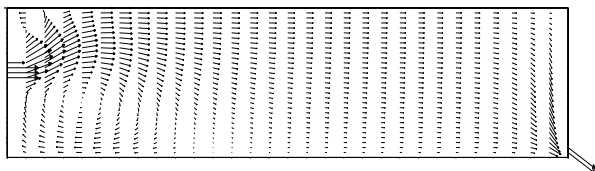


Figure 6.35: Flow rate 5.2l/s. Slot Inlet. Vector Field. Single Phase Flow.

### 6.6.7 Results Influent Flow Rate 5.2 l/s

In this section the results from the simulation at the flow rate of 5.2l/s are presented. Table 6.5 shows the times at which the velocity and solids fraction data were measured. Also in this table is the volumetric flow rate obtained by integrating the measured velocity data. As with other experiments in this set, significant variations in the experimental volumetric flow rate were found over time at each of the stations.

The results are presented with graphical comparisons of velocity and solids fraction data, shown in Figures 6.36 and 6.37. Vector plots and solids fraction contour plots are shown in Figures 6.38 to 6.49. Finally, plots of laminar and turbulent viscosity at 7200s are shown in Figures 6.50 and 6.51

	St 1 (3.0m)		St 2 (5.0m)		St 3 (7.0m)	
	Velocity	Solids	Velocity	Solids	Velocity	Solids
time t1	900	600s	1920s	1620s	2820s	2220s
Flow rate	4 l/s		3.5 l/s		2.67 l/s	
time t2	7020s	5100s	7980s	7680s	8820s	8280s
Flow rate	3.7 l/s		4.0 l/s		3.66 l/s	

Table 6.5: Experimental Conditions. Slot Geometry. Flow rate = 5.2l/s.  
Influent velocity = 0.0346m/s. Solids Fraction = 0.001.

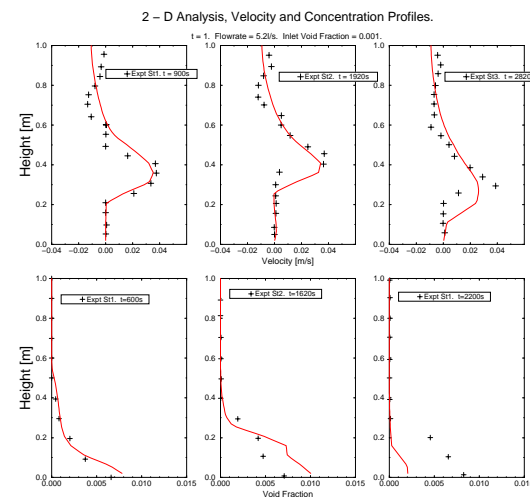


Figure 6.36: Velocity and Solids Fraction Plots, 5.2l/s. Early part of Experiment.

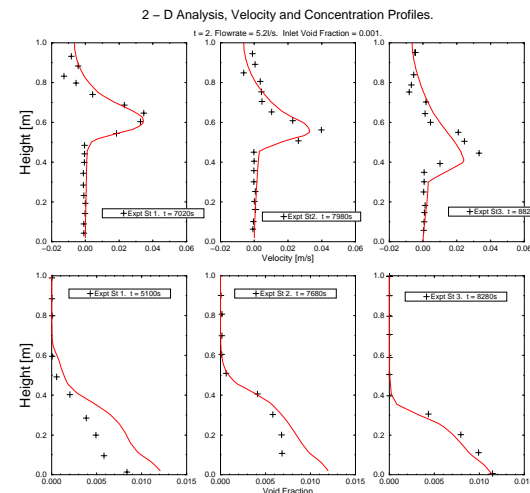


Figure 6.37: Velocity and Solids Fraction Plots, 5.2l/s. Late part of Experiment.

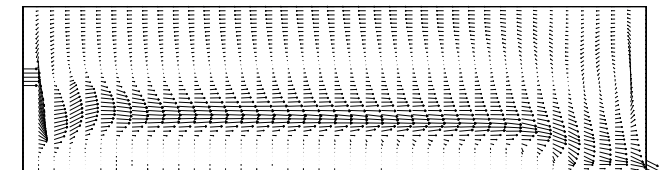


Figure 6.38: Flow rate 5.2l/s. Mixture Velocity. Vector Plot 900s.

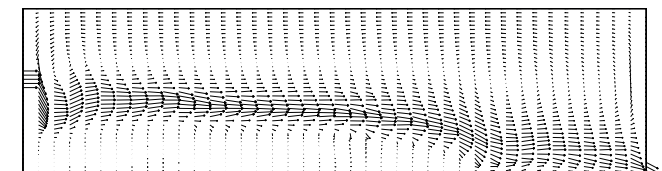


Figure 6.39: Flow rate 5.2l/s. Mixture Velocity. Vector Plot 1920s.

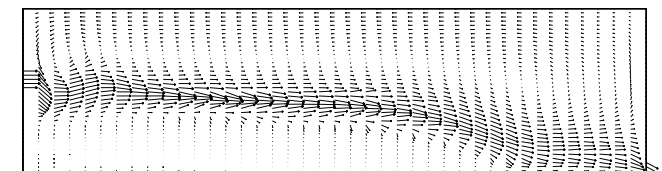


Figure 6.40: Flow rate 5.2l/s. Mixture Velocity. Velocity Vector 2800s.

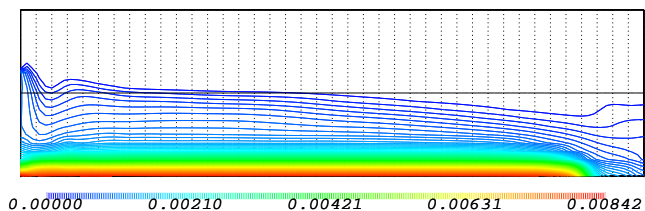


Figure 6.41: Flow rate 5.2l/s. Solids Fraction 600s.

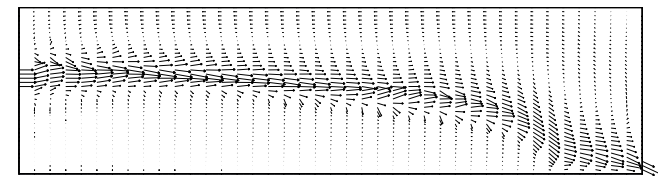


Figure 6.44: Flow rate 5.2l/s. Mixture Velocity. Vector Plot 7000s.

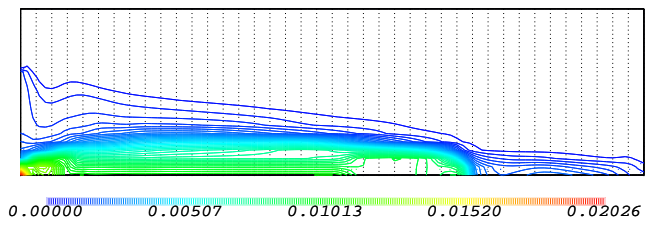


Figure 6.42: Flow rate 5.2l/s. Solids Fraction 1600s.

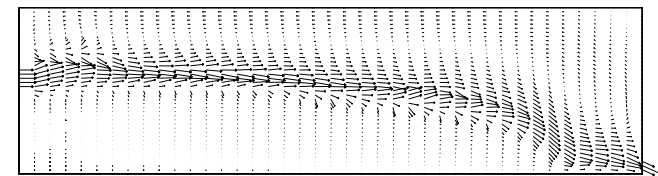


Figure 6.45: Flow rate 5.2l/s. Mixture Velocity. Vector Plot 7900s.

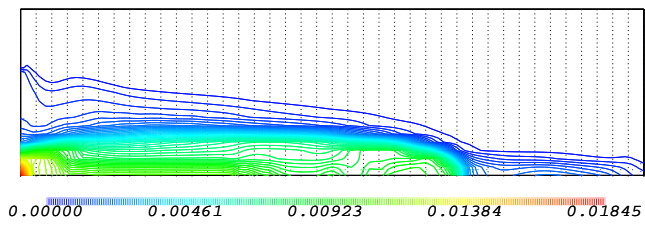


Figure 6.43: Flow rate 5.2l/s. Solids Fraction 2200s.

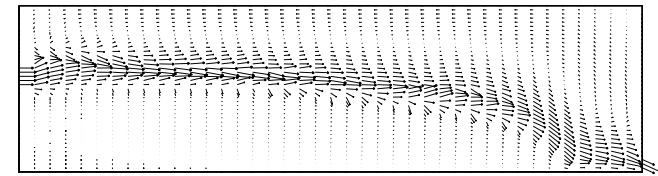


Figure 6.46: Flow rate 5.2l/s. Mixture Velocity. Vector Plot 8800s.

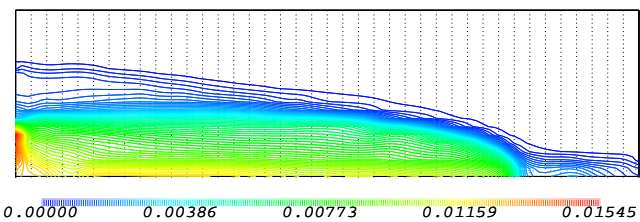


Figure 6.47: Flow rate 5.2l/s. Solids Fraction 5100s.

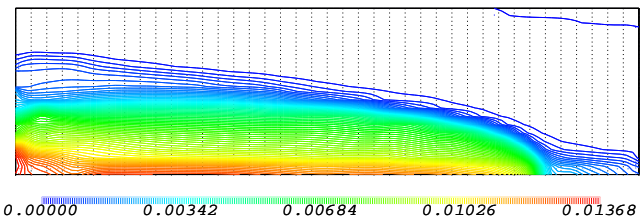


Figure 6.48: Flow rate 5.2l/s. Solids Fraction 7680s.

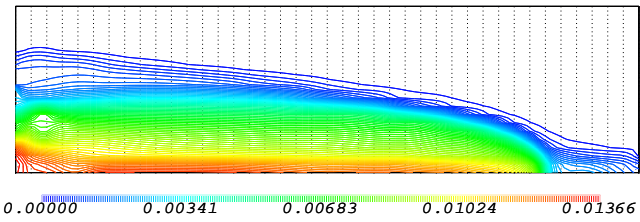


Figure 6.49: Flow rate 5.2l/s. Solids Fraction 8280s.

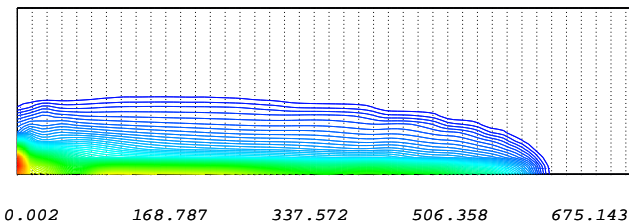


Figure 6.50: Flow rate 5.2l/s. Laminar Viscosity 7200s.

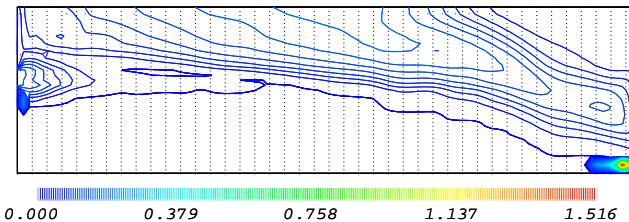


Figure 6.51: Flow rate 5.2l/s. Turbulent Viscosity 7200s.

### 6.6.8 Results Influent Flow Rate 12.0 l/s

Results are presented here for the flow rate of 12.0 l/s. and influent solids fraction of 0.0022. A uniform velocity with a uniform solids fraction distribution was specified at the inlet. Table 6.6 shows measurement times. Also on this table is the volumetric flow rate obtained by integrating the velocity measurements.

Figures 6.52 and 6.53 compare the predicted velocity and solids fraction with the experimental data.

	St 1 ( 3.0m)		St2 (5.0m)		St3 (7.0m)	
	Velocity	Solids	Velocity	Solids	Velocity	Solids
time t1	360s	600s	1380s	1080s	2220s	1680s
Flow rate	12.5 l/s		11.5 l/s		13.0 l/s	
time t2	6180s	7560s	7560s	7260s	8580s	7860s
Flow rate	17.5 l/s		12.5 l/s		14.5 l/s	

Table 6.6: Experimental Conditions. Slot Geometry. Flow rate = 12.0l/s. Solids Fraction = 0.0022. Inlet Velocity 0.08m/s.

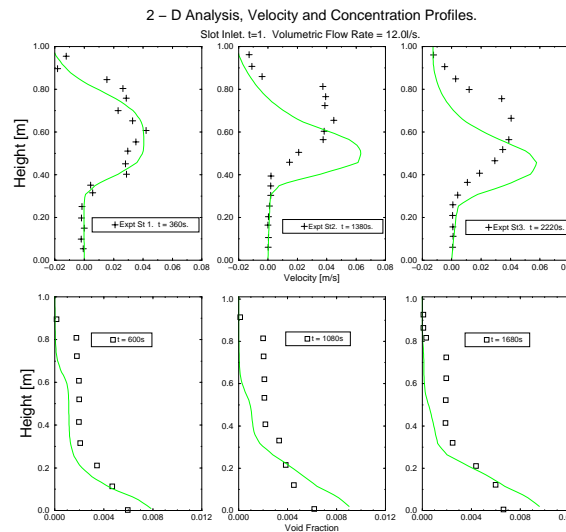


Figure 6.52: Velocity and Solids Fraction Plots, 12.0l/s. Early part of Experiment.

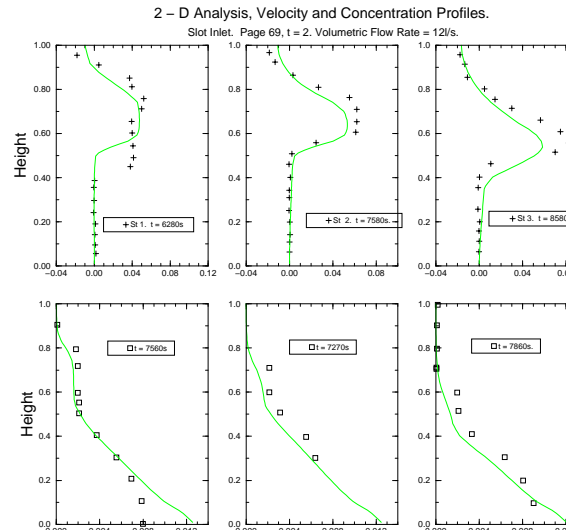


Figure 6.53: Velocity and Solids Fraction Plots, 12.0l/s. Late part of Experiment.

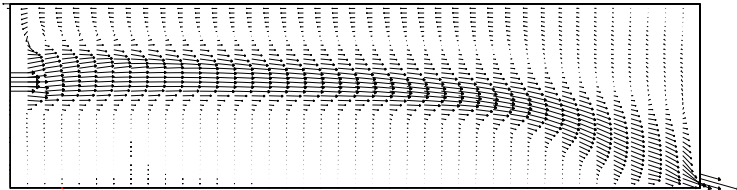


Figure 6.54: Flow rate 12.01l/s. Vector Field 2550s. Deposition of Settled Bed.

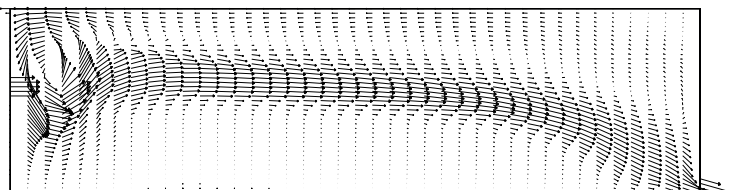


Figure 6.55: Flow rate 12.01l/s. Vector Field 2700s. Erosion of Settled Bed.

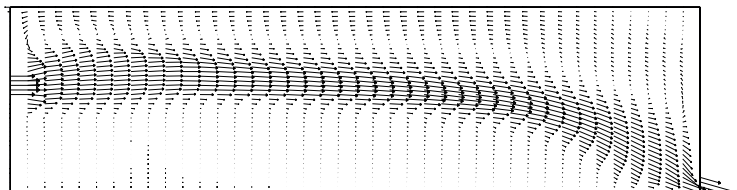


Figure 6.56: Flow rate 12.01l/s. Vector Field 2850s. Re-deposition of Settled Bed.

## 6.7 Discussion.

The simulations with the slot inlet board exhibit similar trends in the flow field to those with no inlet board. The earlier observations about the predictive accuracy are also applicable here. However, there are some differences.

With the slot inlet the influent plunges immediately to the tank floor, showing no plane jet like structure as found in the single phase simulation. Thereafter, the density current runs over the settled sludge layer along the length of the tank to the outlet.

Although the velocity profiles are generally well predicted, there are some anomalies at some stations. One is shown in Figure 6.36, for the flow rate of 5.2l/s. The predicted density current at the last station of this plot is very close to the tank floor, with correspondingly low values of solids fraction in the settled bed region.

Initially a uniform settled sludge layer is deposited along the length of the tank as can be seen on the vector plot of Figure 6.38, and the solids fraction plot, Figure 6.41. However, because of high shear levels at the outlet the settled sludge layer near the outlet suddenly fails and is swept out of the tank, Figures 6.39 and 6.42, reducing the overall length of the sludge layer. Sludge slowly starts to be redeposited in this cleared end section as the rest of the settled bed builds up height. At 2820s, when the predicted and measured velocity are first compared at this station, redeposition is just underway and the bed height and concentration here are low. At 8820s, however, redeposition of the settled bed at this station is complete, with the predicted sludge blanket reaching the experimental height, Figure 6.37.

The plot of the laminar viscosity distribution for a flow rate of 5.2l/s at 7200s in Figure 6.50 shows that very high values of viscosity are essentially confined to the settled bed region. A plot of turbulent viscosity for this 5.2l/s case and time is shown in Figure 6.51. The stratification here is less clearly

defined than on the corresponding plot for a flow rate of 19.1l/s. This is due in part to the fact that the lower volumetric flow rate produces lower overall velocities and velocity gradients in the tank and around the density current; thus turbulence production is generally lower.

If we consider the simulation for 12.0l/s, it can be observed that the predicted velocity profiles at stations 2 and 3, Figure 6.52, are significantly different from the experimentally recorded shape - although the settled bed height is quite well predicted. The simulation gives much more jet-like velocity profiles at these later two stations, thus over-predicting the maximum velocity. As the influent current height is below that found in experiment at these two stations, the solids fraction values measured through this influent current and in the upper part of the tank are less than found in the experiment. Values of solids fraction in the settled sludge region are well predicted.

In the second half of the experiment, the overall structure of the jet / buoyant plume is well predicted with good agreement with the height of the settled bed at stations 2 and 3, Figure 6.53.

Integration of the experimental velocity profile at station 1, Figure 6.53, shows a flow rate of 17.5 l/s with the simulation giving good agreement in the top section of the velocity profile but missing the profile in the region below.

An interesting feature was observed which may explain the large volumetric flow rate recorded at station 1. Near the slot inlet settled sludge accumulates and starts to block this inlet, Figure 6.54. The shear rate on this sludge then increases until the yield stress is exceeded. At this time the bed shears in a diagonal plane below the settled bed height and the local region near the inlet becomes liquefied, Figure 6.55. Parts of the sludge from the sheared region are swept downstream causing the influent to plunge into this eroded section, producing a noticeable recirculation zone near the inlet. Sludge again settles in this region, see Figure 6.56, until the shear stress induced by the close proximity of the influent jet induces liquefaction and the process is repeated.

Generally, we can say that results are in good agreement with the experimental data on all four of the simulations conducted. The speed and overall shape of the density current were well predicted together with the void fraction in the upper part of the tank and the majority of the settled bed.

From this study we can gain a certain amount of confidence in the predictive accuracy of the model when applied in 3D calculations of full scale settling tanks, which is the subject of the next chapter.

fraction and dispersed phase density was also conducted and this is presented in section 7.4.6. A discussion of the results follows.

# Chapter 7

## Full Scale Simulations.

### 7.1 Introduction.

In this section the numerical model used in the previous chapter is compared with data obtained in a full scale settling tank, Ueberl (1995). In this study, horizontal mean velocity and solids fraction concentration were measured at a number of stations along the length and across the width of the Limmattal settling tank in Sweden. The time taken to gather all the data for one inlet condition was around four hours, so no distinct time was given for the measurements at each station. Because of this, the numerical simulation was compared with the experimental data at a time when the settled sludge layer in the simulation was at approximately the same height as that found in the experiment. At this time, the flow field above the settled sludge layer should be similar in both the experiment and the simulation .

The results of 2D and 3D simulations for a single experimentally recorded inlet condition are presented. The calculations are presented for two different dispersed phase densities for the experimentally given density difference between the inlet and outlet, the reasons for this are given in the section 7.2. For the 3D calculation, an additional simulation using a lower influent solids

### 7.2 The Experimental Investigation of The Limmatatal Settling Tank.

The concrete basin is shown in Figure 7.1, it is 49.85m long, 7.5m wide and has a maximum depth at the hopper of 6.63m. The minimum depth at the tank end wall of is 2.8m. Longitudinal velocity was determined by means of submerged drifters, a method that involves measuring the time taken for a drifter at the measurement depth to traverse a given distance from which the velocity could be calculated. Accuracy is given to +/- 2mm/s, Bretsher et al (1990). Solids concentration was measured by an ultrasound probe. Interference with concentration measurements occurred when the probe was placed within 0.2m of the walls or sludge scraper, hence no readings were taken closer than this distance. Also these measurements were limited to an upper solids fraction of about 0.06, around 1.25 times the inlet solids fraction. As a consequence readings in the high concentration region of the lower part of the density current and in the settled bed region could not be made.

**Tank Inlet.** Each tank is fed by two aeration basins, each of which effectively feeds one side of the tank. This arrangement is shown in Figure 7.2. Four concrete slots 0.08m wide and 2.28m high allow the activated sludge to leave the aeration basin and enter into the settling tank, where it impinges directly onto concrete baffles 0.55m wide and around 3.08m high, with a flow space of 0.2m between each baffle.

**Tank Outlets.** Sludge is withdrawn from the base of the sludge hoppers at 40l/s by an Archimedes screw type pump. The clear water is withdrawn from the tank surface by four effluent outlet weirs located at 16m, 26m, 36m

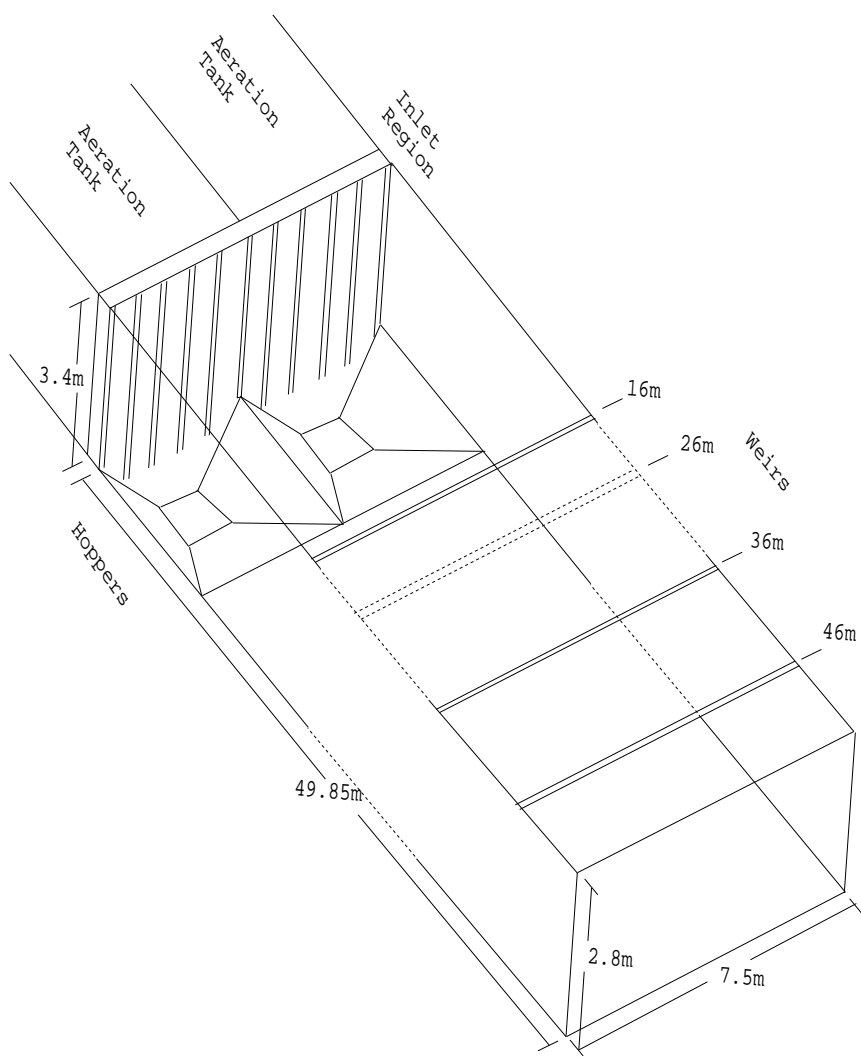


Figure 7.1: Schematic of Limmattal Settling Tank.

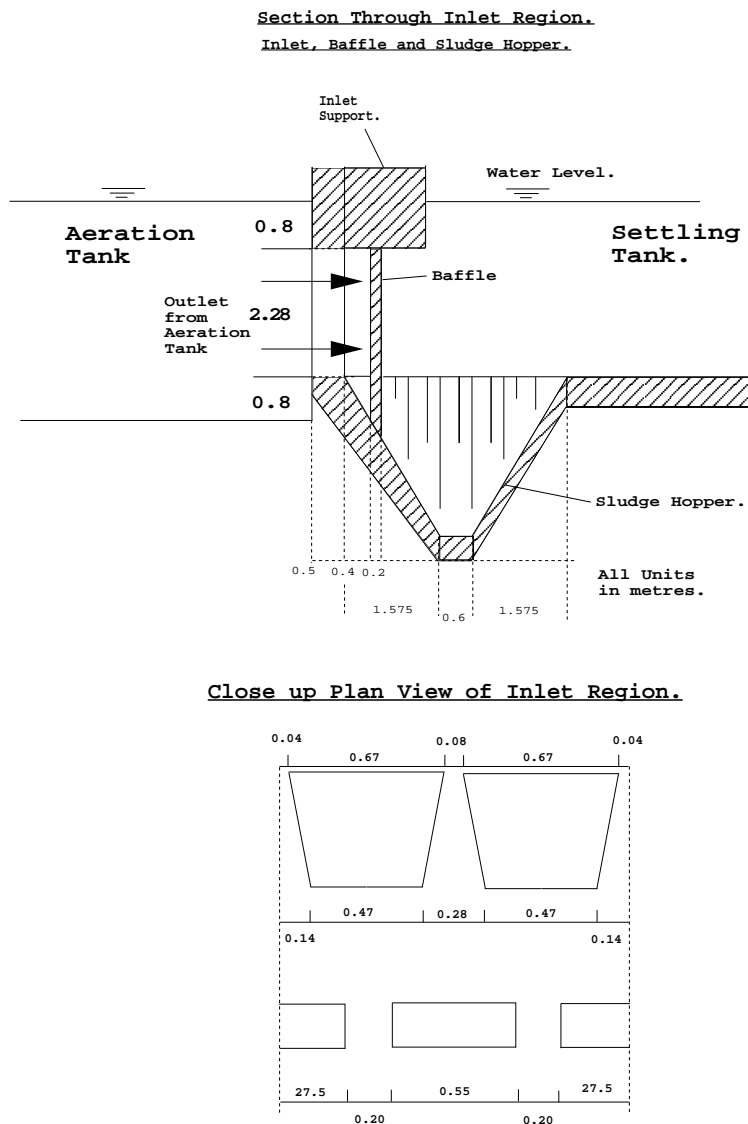


Figure 7.2: Mid-Depth Section through the Inlet Baffles. Limmattal Settling Basin.

and 46m along the length of the tank. The outflow rate was 10 l/s for each weir.

**Sludge Scrapers.** Settled sludge is moved along the floor of the tank towards the sludge hopper by a continuous chain scraper. This scraper moves baffles 0.125m deep at a rate of 0.0015m/s towards the inlet.

**Inlet Conditions.** The total inlet volumetric flow rate was 80 l/s. A natural plane of symmetry exists in the tank dividing it in half along its length and running from the inlet to the end wall over the ridge between hoppers. In order to minimise the cost of the calculation, the computational domain was generated to simulate half the tank up to the plane of symmetry. The case chosen for simulation showed little asymmetry in the velocity profiles either side of the naturally occurring symmetry plane, i.e a case in which each aeration basin is contributing half the influent volumetric flux.

The density difference between inlet and effluent is between 2 - 4  $kg/m^3$  for all the experiments. The sludge density is 1042  $kg/m^3$ , which is the density of the hydrated sludge flocs in suspension, Ueberl(1995). This is low compared to dry sludge densities previously reported between 1300 and 2000  $kg/m^3$ , Larsen (1977) and Dahl (1993), used in the simulations of Chapter 6. For a given density difference of 2  $kg/m^3$  between influent and effluent and a dispersed phase density of 1042  $kg/m^3$  the inlet solids fraction was calculated as 0.0476. This is rather high in comparison to the inlet solids fraction reported in the previous simulations.

Because of this low sludge density and correspondingly high solids fraction, the simulation was also carried out with a sludge density more usually reported in the literature. If the same activated sludge density as found in the Dahl case, 2000  $kg/m^3$ , Chapter 6, is used to simulate the inlet density difference for the Ueberl test case, the inlet solids fraction is calculated as 0.002. This is very close to the inlet solids fraction of 0.00215 found in one of the in Dahl test cases, section 6.6.3, who's exponents and coefficients for  $\tau_y$ ,  $\eta$  and  $V_s$  have been

shown to yield good predictions of the velocity and solids fraction distributions. Hence, the same exponents and coefficients can be used directly in the Ueberl case if this dispersed phase density is used. Given that the density difference of 2  $kg/m^3$  between the influent and effluent is the same for the simulations carried out at the two different dispersed phase densities, densimetric Froude number similarity is preserved between them.

A third condition with a density ratio of 1.3:1 and a mixture density difference of 1  $kg/m^3$  was also simulated as part of an inlet condition sensitivity study to establish what effects these changes would have on the predictions.

#### Physical Properties.

The coefficients and exponents for simulation using an activated sludge density of 2000  $kg/m^3$  were taken directly from the Dahl case and are given in Table 7.2.

For the simulation with a dispersed phase density of 1042  $kg/m^3$  and inlet solids fraction of 0.0476, and for the simulation with a dispersed phase density of 1300  $kg/m^3$  and inlet solids fraction of 0.003, the physical properties of activated sludge were calculated by the method shown in section 6.3.1. That is; the exponent  $b$  in the general formulae, equation 6.4, is multiplied by the ratio of the inlet concentration of the Dahl case,  $\alpha = 0.002$ , to the inlet concentration,  $\alpha_{in}$  of the case being studied. This effectively scales the physical properties of the sludge used in the Dahl simulation onto the low density sludge used in the Limmattal case, the subsequent values are shown in Table 7.2.

Property $\Phi$	Coefficient a		Exponent b	
	All Cases		Density ratio	
	1.042:1		2:1	1.3:1
Yield Stress	5.5469E-5 kg/(m.s <sup>2</sup> )	39.95	951.25	634.16
Bingham Viscosity	2.3143E-4 kg/ms	7.35	179.26	119.50
Settling Velocity	-2.198E-3 m/s	12.97	285.84	190.56

Table 7.1: Coefficients used for the calculation of Sludge Properties from equation 6.4 for the Ueberl Case.

### 7.3 2D Simulation of the Limmattal Tank

The computational domain for the 2D simulations is shown in Figure 7.3 and the boundary conditions are shown in Figure 7.4. Since the tank geometry

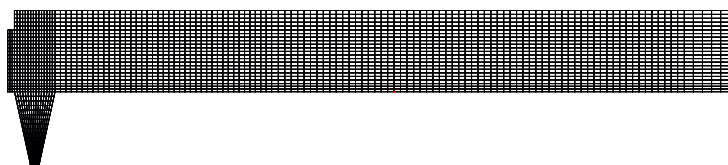


Figure 7.3: Computational Domain. 2D Simulation. Limmattal Settling Basin.

is three dimensional some simplifying assumptions had to be made concerning the tank geometry and the inlet and outlet boundary conditions.

The tank was simulated without inlet baffles. The total effective inlet area was considered to be the area of the inlet slots plus the area of wall separating the inlet slots on the end wall of the aeration basin.

The inlet velocity was obtained by dividing the influent volumetric flux by the new effective inlet area, giving a lower mass flux per unit area at the inlet

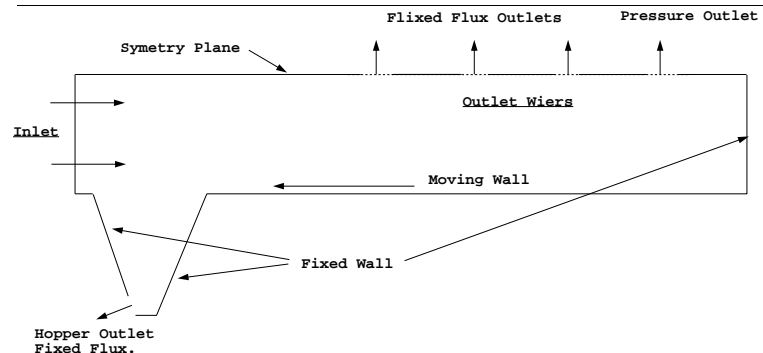


Figure 7.4: Boundary Conditions. 2D Simulation. Limmattal Settling Basin.

than in the 3D simulation. This simplification also produces a lower mean inlet velocity. However, because the solids fraction and hence the density difference between the influent and the effluent are the same in both cases the magnitude of the density current produced should also be the same.

The inlet flow was specified to have a uniform velocity and solids fraction over the inlet area. Turbulent intensity was specified as 10% of the inlet velocity, with the dissipation rate calculated from 0.2 times the shortest inlet dimension. In 2D calculations the hopper is considered to taper towards the base only in the lengthwise direction and to span the width of the tank.

The outlet at the hopper base was also considered to act over the whole width of the tank. This arrangement results in a lower mean outlet velocity than found in the 3D case. This outlet was simulated by a fixed flux outlet boundary.

The outlet conditions at the weirs are the same in both the 2D and 3D simulations, as the weirs extend the full width of the tank. In both simulations, three of the weirs were simulated with a fixed flow outlet boundary with the fourth, nearest the end wall of the tank, simulated as a pressure boundary.

The sludge removal mechanism was simulated by a moving base wall, see

Figure 7.4. The rate of sludge accumulation on the tank floor is determined by the speed of this wall. Over prescription of this velocity tended to disrupt the flow field, while under prescription prevented sludge from returning to the hopper. By trial and error, a condition was arrived at where moderate accumulation was allowed with the sludge blanket rising over the course of the simulation. The calculation was allowed to proceed for 12,500s at which point, although the sludge blanket was still rising, the main features of the flow field were established and in a nearly steady. In fact no real discernible changes in the main features of the flow field in the tank were observable after about 7500s.

### 7.3.1 Results of the 2D Simulation

Densimetric Froude number similarity coupled with appropriately scaled physical properties should give very similar velocity and normalised void fraction fields within the tank and in the two dimensional simulation the results are identical.

Comparisons with experimental velocity data taken at the center plane of the tank for the 1.042:1 density ratio case at times 2500s, 4500s and 6500s are given in Figure 7.5. Figure 7.7 shows the velocity profiles for the simulation with a density ratio of 2:1 plotted against the simulation with a density ratio of 1.042:1 at 4500s. The results are essentially identical.

Considering Figure 7.5 it can be observed that;

- 1) The sludge bed level is rising throughout the simulation. It is at approximately the correct level at 4500s for the first four stations but fails at the later stations to reach the experimental bed height at any time. This indicates that the settling velocity may be too high, causing suspended solids to be deposited in the first half of the main body of the tank.

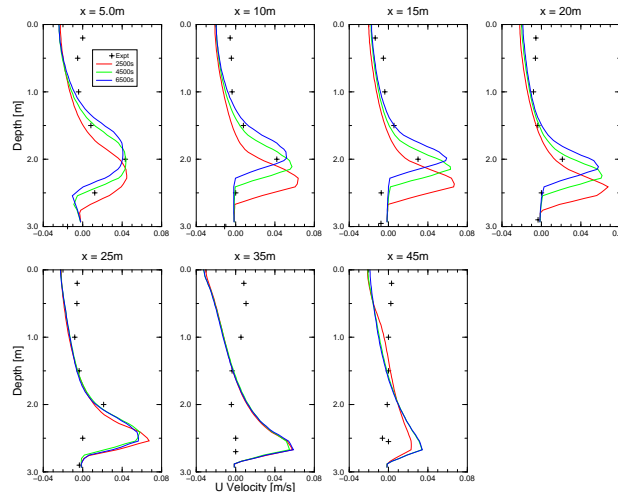


Figure 7.5: Velocity Profiles. Density Ratio 1.042:1. 2D Simulation.

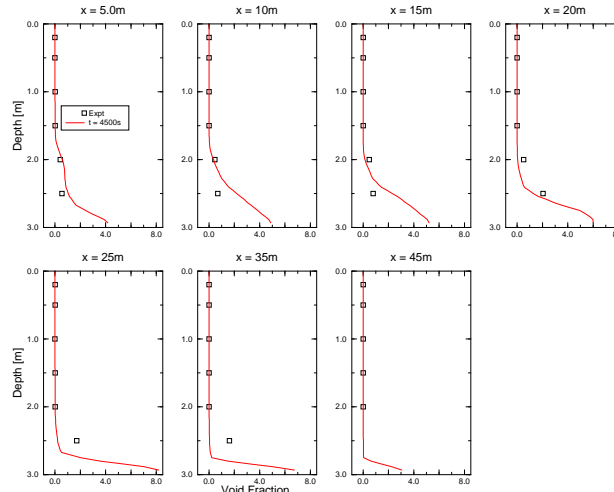


Figure 7.6: Solids Fraction. Density Ratio 1.042:1. 2D Simulation.

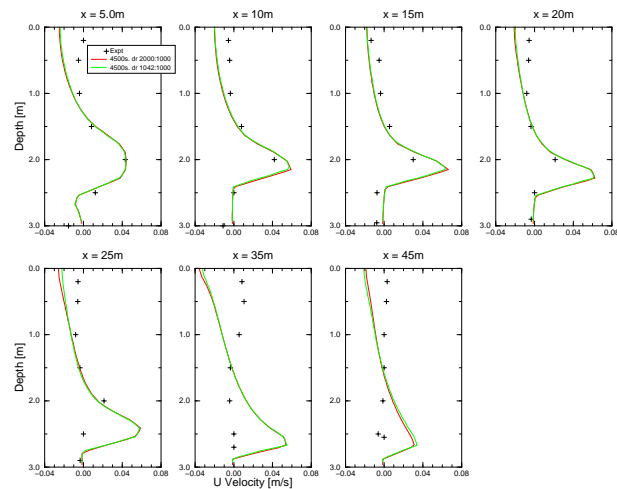


Figure 7.7: Velocity. Comparative Study. Density Ratios 1.042:1 and 2:1. Fr 0.0659. 2D Simulation.

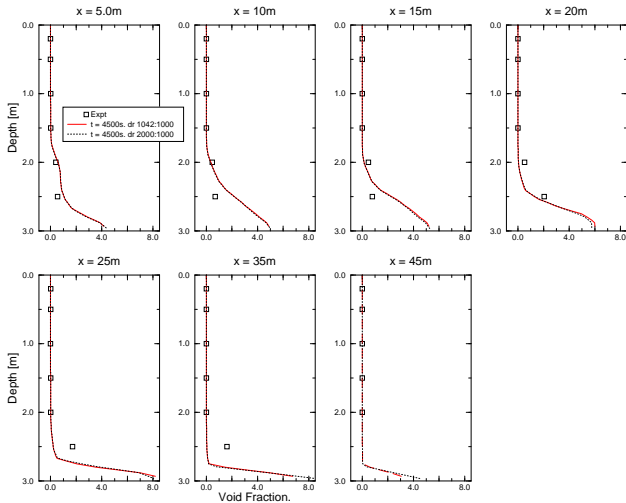


Figure 7.8: Solids Fraction. Comparative Study. Density Ratios 1.042:1 and 2:1. Fr 0.0659. 2D Simulation.

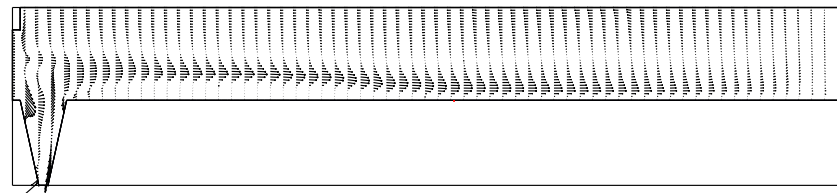


Figure 7.9: Velocity Field. Density Ratio; 1042:1000. t = 4500s. 2D Simulation.

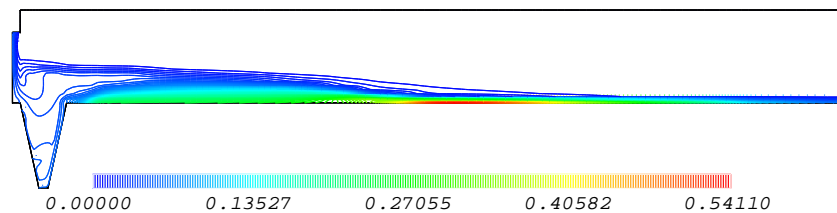


Figure 7.10: Solids Fraction. Density Ratio; 1042:1000. t = 4500s. 2D Simulation.

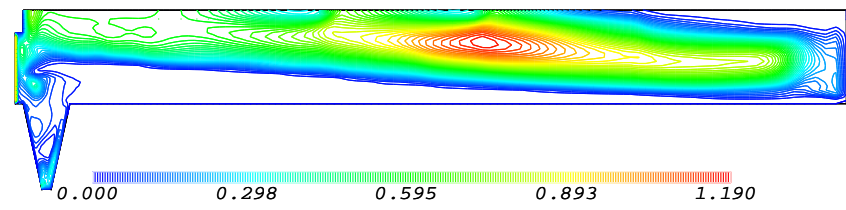


Figure 7.11: Turbulent Viscosity. Density Ratio; 1042:1000. t = 4500s. 2D Simulation.

2) The peak velocity and general shape of the velocity profile, are well predicted at the 5m station. After that, the predicted peak velocity gradually exceeds the experimental results, although the depth of the current is well predicted at the 10m, 15m and 20m stations. At the last two stations, where the experimental velocity indicates the density current had been dissipated, the simulation indicates that it still persists.

Solids fraction plots for a density ratio of 1.042:1, illustrated in Figure 7.6, show good agreement with the experimental results at all stations. Also, the comparison plots of solids fraction at density ratios of 1.042:1 and 2:1, Figure 7.8, are essentially identical to each other. These plots show that the solids fraction within the density current from about 25m onwards is very low, about equal to the ambient level in the tank. Comparison with the iso-concentration line contour plot for solids fraction, Figure 7.10, reinforces this observation of very low void fractions in the latter part of the density current. Despite this, however, velocities in the latter part of the current are over predicted. There are three main reasons why this could be taking place.

i) The 2D solution does not reproduce secondary flow that may help in the mixing and dissolution of the density current after the dispersed phase has been deposited from suspension.

ii) Buoyancy modifications to the  $k$  equation alone may overly inhibit the turbulent mixing of the density current, see for instance Lakehal et al. (1999). This may have a significant effect in the transition from jetting flow to streaming flow which takes place with the termination of the density current. The Dahl solutions demonstrated the buoyancy modifications' ability to suppress turbulence within a density-stratified flow regime such that very good agreement between the numerical simulation and experimental results could be obtained. However, in the Dahl simulation, for all cases, the density current leaves the tank before being dissipated. Essentially the experiment recorded the start and middle sections but not the end of the currents life. The dissip-

tion mechanism may require more mixing than the turbulence model allows.

Figure 7.11 is a plot of turbulent viscosity. The highest values are found at the center of the main recirculation zone. In the settled bed region and the bulk of the density current, the results clearly indicate that the flow field is laminar due to density stratification. They also show that turbulent mixing is taking place in the later half of the density current at stations 25m to 45m. This mixing process may not be rapid enough, however.

iii) The viscosity within the density current may be under predicted, as will be discussed in section 7.5.

### 7.3.2 The Flow Field within The Hopper.

Hoppers in secondary settling tanks have been thought of as storing the settled sludge before it leaves the tank via the hopper outlet. There has been little concrete evidence as to the nature of the flow field within the hopper as measurements of velocity and concentration are not generally taken in this region. Analysis of the 2D solution gives an insight into the development of this flow field. There appear to be five distinct phases.

**1)** For a tank in which a heavier influent entering into a quiescent lighter medium, the influent density current plunges right to the bottom of the hopper, scours the base and runs straight up the other side. At the top, where the hopper abuts onto the main tank wall, there is a point of incipient separation. The density current then runs along the the tank floor towards the end wall. This occurs at approximately 212 seconds from the start of the experiment and is illustrated in Figures 7.12 to 7.14.

**2)** As sludge accumulates on the tank floor and is pushed towards the hopper, it builds up an opposing density current to the influent. Figures 7.15 to 7.17 show a stage were by the **return sludge density current** has driven down under the influent density current on the tank side hopper wall. It is of

insufficient density to reach the bottom of the hopper and the dispersed phase is re-entrained into the up flowing influent density current. A recirculation zone formed on the tank side hopper wall indicates the onset and extinction of the new density current which occurs at 512s.

3) By 2500s, the return sludge density current has broken through to the hopper outlet by running directly underneath the influent current, Figures 7.18 to 7.20. Between the two counter flowing currents a significant amount of turbulence is generated, causing significant re-entrainment of the activated sludge from the return sludge current into the influent density current.

The point of incipient separation at the top of the hopper has now formed a recirculation zone. This zone forms a transition between the settled bed being pushed towards the hopper and the return sludge density current at the top of the hopper. Significant dilution takes place in this zone.

4) At 3500s the return sludge current is well established, a recirculation zone starts to form at the bottom of the hopper between the two counter flowing currents, forcing the influent current to rise, Figures 7.21 to 7.23.

5) The steady state condition appears to have been reached at 7500s. The influent current has been forced practically out of the hopper by the recirculation zone, Figures 7.24 to 7.26. This zone has an unusual shape, being very angular it seems to fit the hopper shape. Further, velocities within the recirculation zone are low, considering the magnitude of the velocities either side of it. The reason for this is that **Non - Newtonian** effects dominate this feature as indicated by the contour plot of laminar viscosity shown in Figure 7.27. The dispersed phase solids fraction within the recirculation zone is quite high but velocity gradients at the center of this feature are low. So, starting from the center and remembering that the laminar viscosity is dependent on the **shear rate** and solids fraction, the flow field becomes more viscous gradually, reducing the overall velocity of this feature. In effect the flow regime in the hopper has gone from being dominated by turbulent viscosity to being

dominated by laminar viscosity.

In this case, most of the dispersed phase at the outlet does not gradually settle through the hopper region but is transported directly from the settled bed region by way of the return sludge density current.

Generally, hoppers in this location are regarded as serving a storage role in secondary settling tanks, with the dispersed phase concentration gradually increasing towards the base by virtue of the dispersed phase settling velocity. In this case, however, the hopper seems to serve more as a device for separating the influent current from the return sludge current in the hopper. It is evident that the flow field within the hopper depends on the hopper outflow rate and the magnitude of the return sludge current.

Figure 7.12: Vector Field 212s.

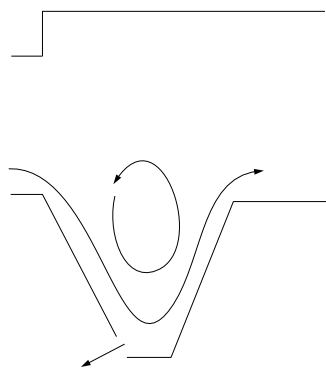
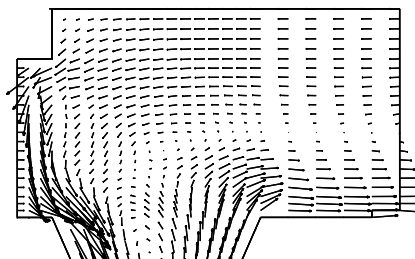


Figure 7.13: Flow Field Schematic.

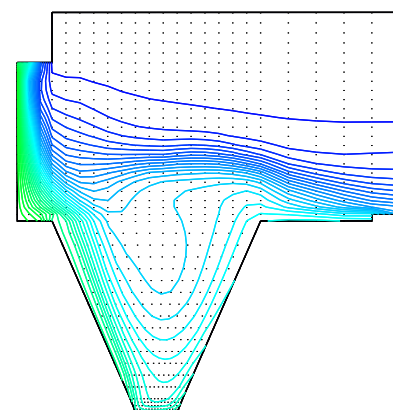


Figure 7.14: Solids Fraction 212s.



Figure 7.15: Vector Field 512s.

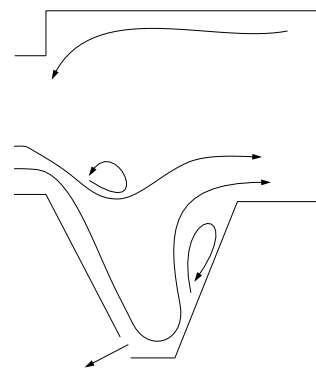
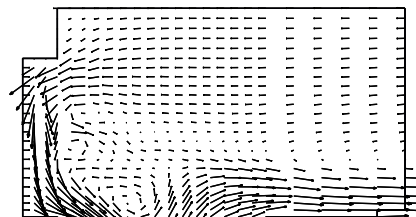


Figure 7.16: Flow Field Schematic.

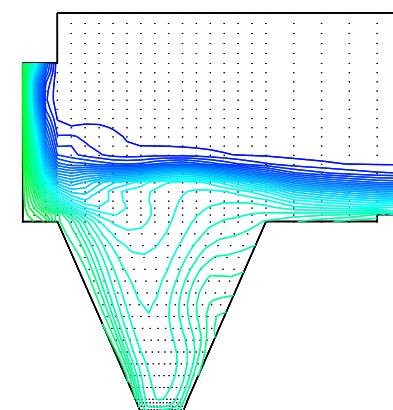


Figure 7.17: Solids Fraction 512s.



Figure 7.18: Vector Field 2500s.

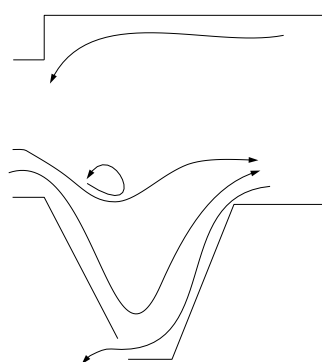
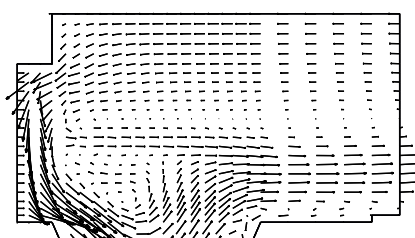


Figure 7.19: Flow Field Schematic.

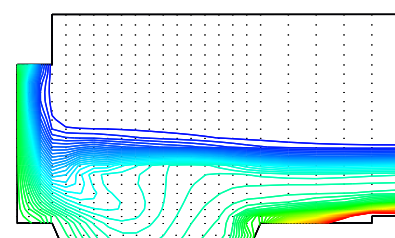


Figure 7.20: Solids Fraction 2500s.

00000 0.02500 0.05000 0.07500 0.10000

Figure 7.21: Vector Field 3500s.

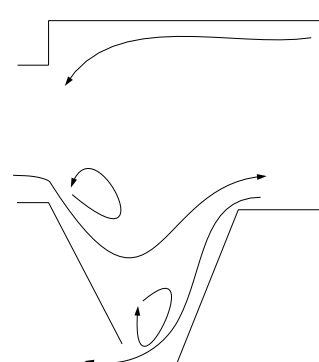
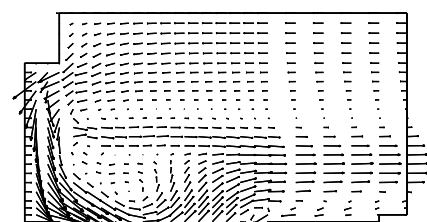


Figure 7.22: Flow Field Schematic.

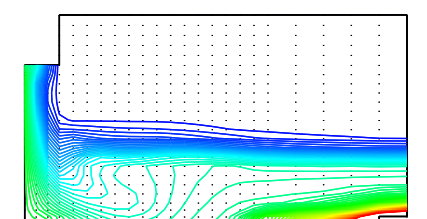


Figure 7.23: Solids Fraction 3500s.

00000 0.02500 0.05000 0.07500 0.10000

Figure 7.24: Vector Field 7500s.

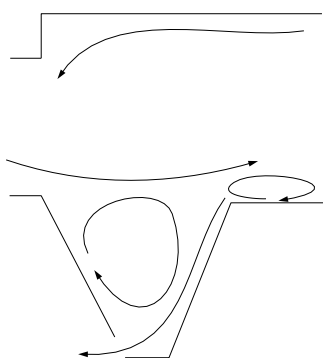
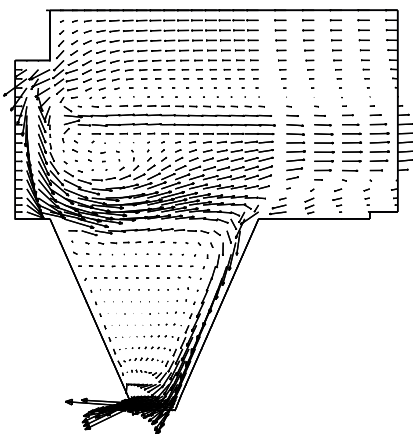


Figure 7.25: Flow Field Schematic.

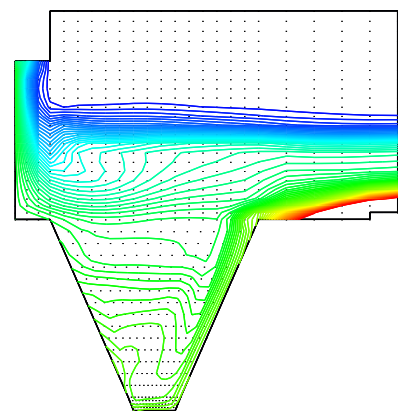


Figure 7.26: Solids Fraction 7500s.

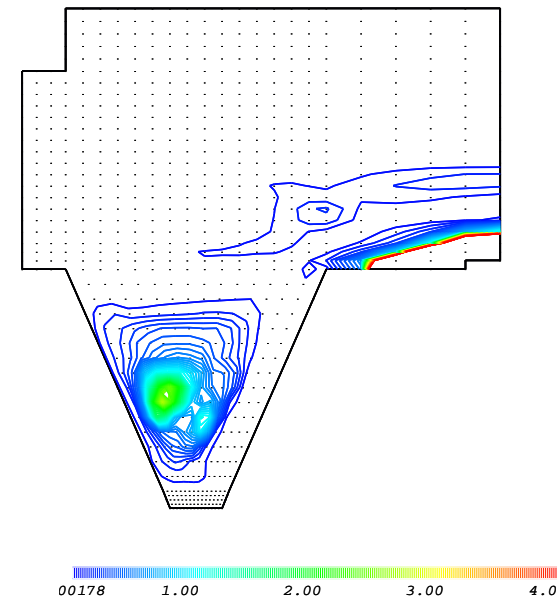


Figure 7.27: Laminar Viscosity 7500s.

## 7.4 3D Simulation of The Limmattal Settling Tank.

A coarse and fine grid of the flow space within the Limmattal Settling Tank were generated, the fine grid was decomposed to run in parallel on a twin processor computer. As with the 2D solution, the two-phase calculation was performed using the ‘settlingFoam’ code.

Firstly, a time marching simulation was carried out on the coarse grid of 18,000 cells. The calculation was allowed to proceed until the start up transients were dissipated. The main transient consisted of a wave set up by the reflection of the density current off the end wall of the tank. This wave traveled back and forth along the length of the tank between the inlet and back wall, gradually becoming weaker until it eventually disappeared. This process took around 2500s. The solution was then mapped to the fine grid of 73,000 cells, Figure 7.28, which has local mesh refinement around the baffles and in the hopper region, Figure 7.29, as well as a more general refinement throughout the domain.

In 2D, the settled bed region showed high concentrations and large gradients of the dispersed phase. Local refinement of this region in the 2D simulations left the maxima and high concentration gradients largely unaltered. Hence, no special refinement was made in this region in the 3D simulation.

Before the two-phase calculations were carried out however, a single phase calculation was performed using the fine grid as described below.

### 7.4.1 Results from a Single Phase Calculation.

A single phase calculation was carried out with water as the working fluid. The tank inlet volumetric flux and other boundary conditions were specified as for the two-phase case, section 7.3, except that a stationary tank floor wall was used.

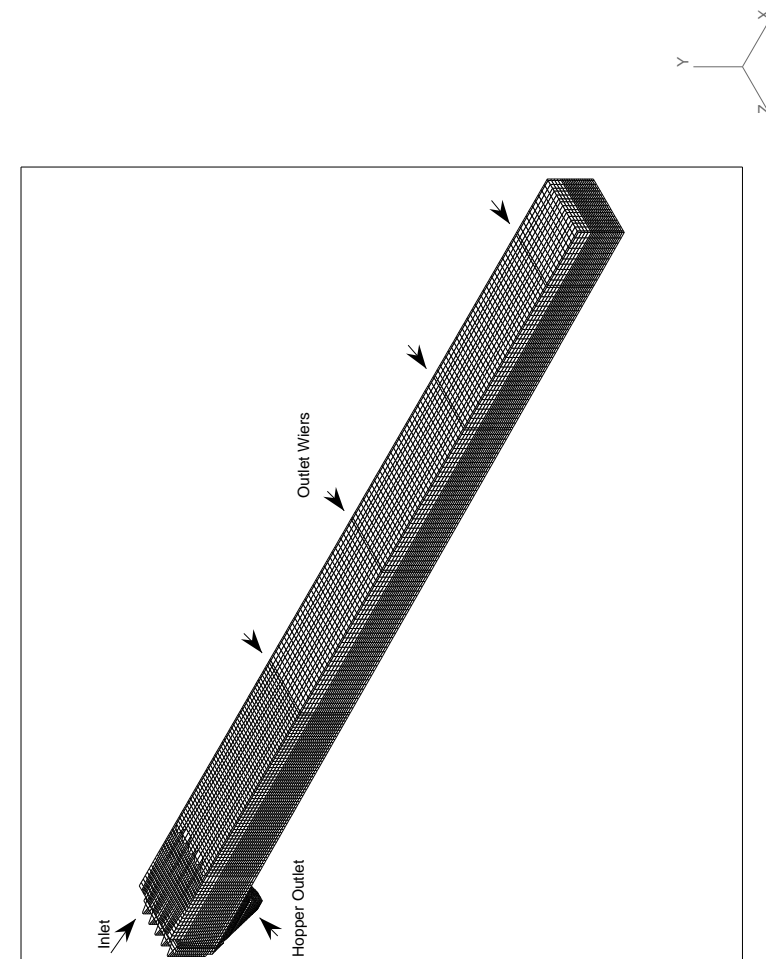


Figure 7.28: Computational Domain

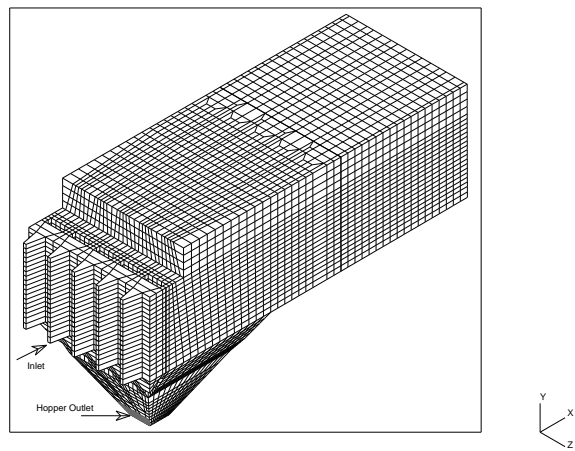


Figure 7.29: Computational Domain, First 10m.

The simulation revealed the flow field had a steady state solution with no shedding from the baffles, nor were there any transient features elsewhere in the domain.

Graphs comparing the velocity profiles of the single phase flow calculation with the two - phase experimental results are shown in Figures 7.30 and 7.31. It can be seen that the calculated velocity is practically uniform through the depth of the tank, as would be expected by a single phase flow in what is essentially an open channel. The peak in velocity associated with the density current is absent from the calculation due to the fact that no buoyancy forces are being brought to bear. This illustrates that single phase calculations can not adequately predict the buoyancy dominated flow field found in settling tanks.

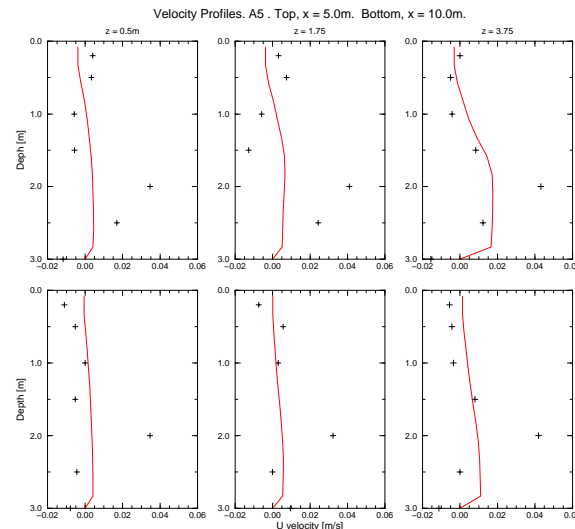


Figure 7.30: Velocity Profiles. Single Phase Flow Regime. 3D Simulation.

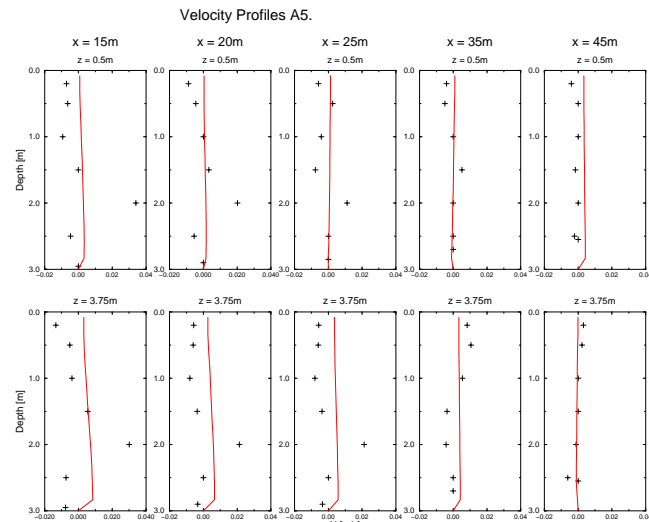


Figure 7.31: Velocity Profiles. Single Phase Flow Regime. 3D Simulation.

#### 7.4.2 Results from The Two Phase Calculations.

As with the 2D geometry, two simulations were performed for the experiment i.e. two different influent dispersed phase densities were used with the same density difference between the influent and the effluent streams.

In the 2D simulation the velocity profiles and normalised solids fraction distribution were seen to be identical for both dispersed phase densities, Figures 7.5 and 7.6. Such similarity has not occurred in the 3D calculation. The reasons for this are not clear.

The main difference between the simulations is in the prediction of the length of the density current and associated peak velocities in the latter half of the settling tank, here the 2:1 density ratio gives closer comparisons with the experimental velocity. However, the flow fields at both density ratios have similar features, these are described in section 7.4.4.

As with the 2D case, vector and contour plots from the 1.042:1 density ratio simulation will be chosen to illustrate the main features of the flow field as this was the measured density ratio. Plots to illustrate the flow field from the 2:1 density ratio simulation will also be shown to illustrate the general features of that calculation.

#### 7.4.3 Simulation with a 1.042:1 density ratio.

Comparisons are made with the experimental data at around 6000s, a time when the settled bed is at a similar height to that found in the experiment. In the 2D calculation this occurs at around 4500s.

The predicted velocity profiles for a dispersed phase density of  $1042 \text{ kg/m}^3$  are compared with the experimental results in Figures 7.32 and 7.33. It can be seen that the maximum velocity of the density current, its general shape and depth, together with the depth of the settled sludge layer are well predicted up to about  $x = 15\text{m}$ . After this there is over prediction of the peak velocity

at all stations up to and including  $x = 45\text{m}$ . The experimental data indicates the extinction of the current after about 25m. The depth of the sludge blanket is reasonably well predicted at all stations.

Solids fraction predictions for a dispersed phase density of  $1042 \text{ kg/m}^3$  are compared against the experimental values in Figure 7.34 and 7.35. These data are normalised with the inlet value, in the case  $\alpha_{in} = 0.0476$ .

It can be observed that in the body of the tank above the density current, the measured solids fraction values are  $O(10^{-5})$ , i.e. effectively zero. The simulation reproduces this at all stations. The results with the solids fraction in the settled bed are less well correlated, the ultra sound method being limited to recording concentrations above 1.25 times the inlet solids fraction, section 7.2. Far higher concentration values are expected in this region.

The simulation predicts very steep concentration gradients at the interface of the settled bed and the density current, with high values in the settled bed itself: for example it indicates a concentration maximum of five times the inlet value at  $x = 10\text{m}$ , see Figure 7.34.

#### 7.4.4 General Description of Flow field.

Velocity plots for the 3D solution with a density ratio of 1.042:1 are illustrated in Figures 7.36 to 7.38. They are for the same planes at which the measurements were taken namely at  $z = 0.5\text{m}$ ,  $1.85\text{m}$  and the center plane of symmetry of the tank,  $3.75\text{m}$ . It can be observed that the flow field is very similar in these three planes, indicating being fairly uniform across the width in the main body of the tank. The features of this field also define the four main regions of the settling tank, which are;

- 1) A settled bed region, on top of which lies;
- 2) A large density current that runs practically the entire length of the tank.
- 3) A number of large recirculation zones occupying the main body of the

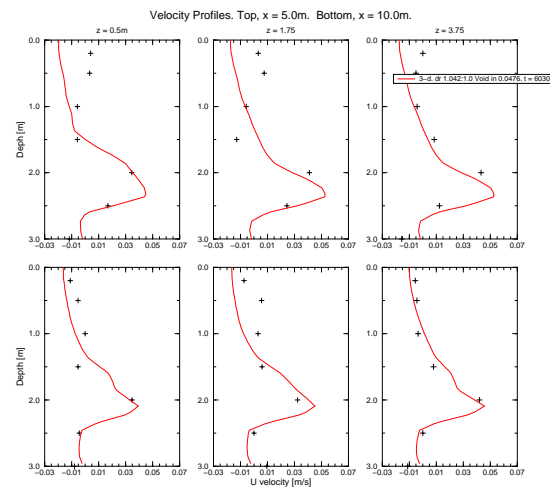


Figure 7.32: Velocity Profiles. Density Ratio 1.042:1. 3D Simulation.

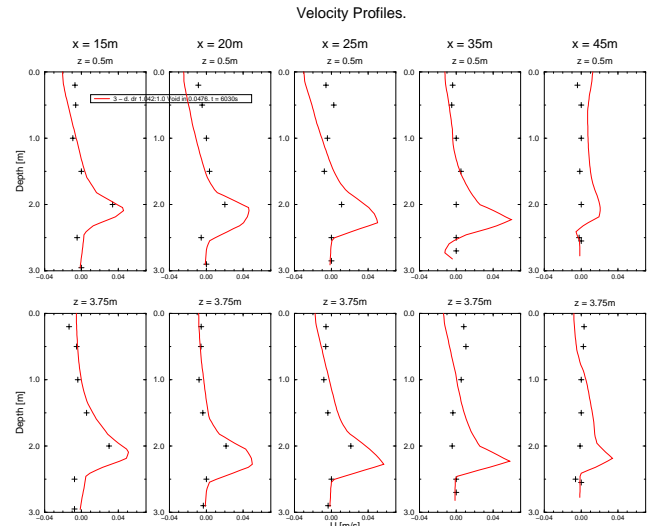


Figure 7.33: Velocity Profiles. Density Ratio 1.042:1. 3D Simulation.

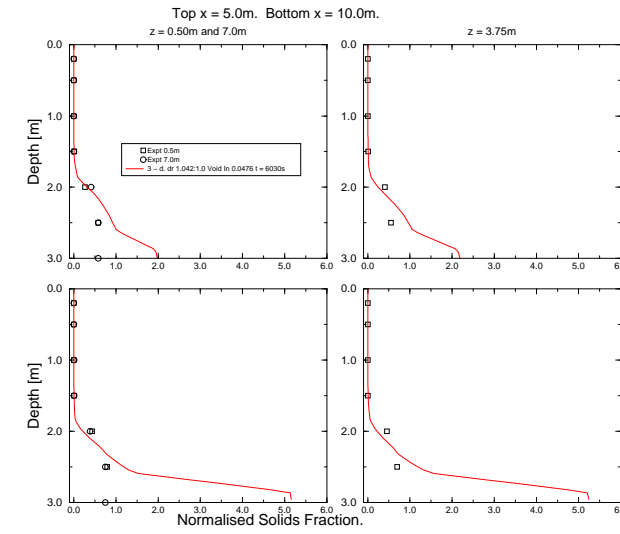


Figure 7.34: Solids Fraction. Density Ratio 1.042:1. 3D. Simulation.

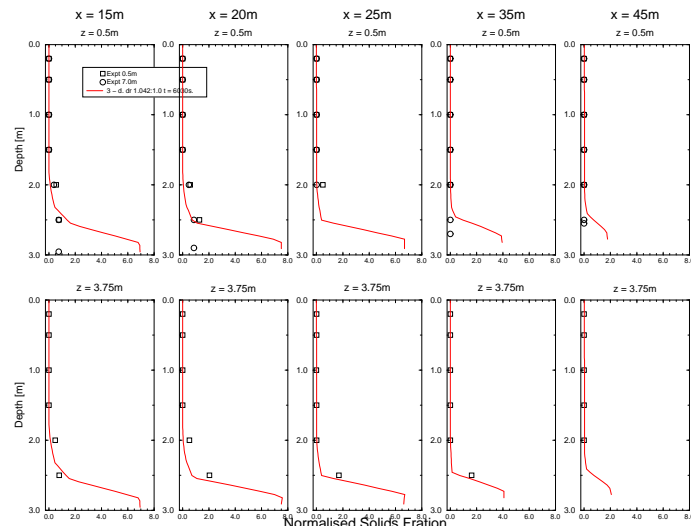


Figure 7.35: Solids Fraction. Density Ratio 1.042:1. 3D Simulation.

ambient fluid above the density current.

- 4) A return surface current at the top of the tank.

A velocity plot in the hopper region is shown in Figure 7.41. It depicts a similar flow field to that described in section 7.3.2. The return sludge density current is well established.

A side view of the solids fraction distribution is shown in Figure 7.39. It can be seen that the solids fraction distribution follows the path of the density current, with the highest values found at the bottom of the settled bed. Above the path of the density current, in the main body of the tank very low values of solids fraction exist, as illustrated in the earlier comparisons with experimental data.

Solids fraction values in the inlet region are similar to the inlet value itself. Stratification has taken place within the hopper with a high value of solids fraction in the return sludge density current and a relatively low value in the main body of the hopper.

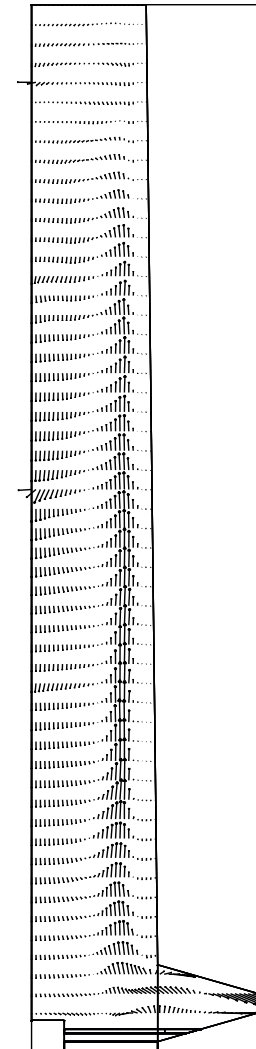
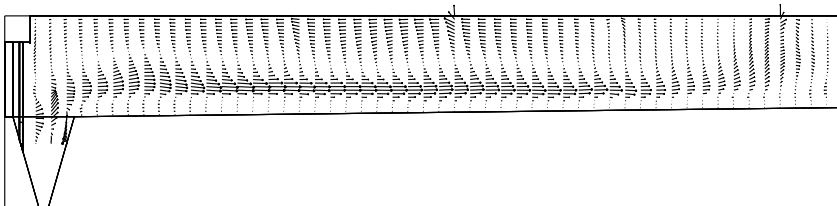
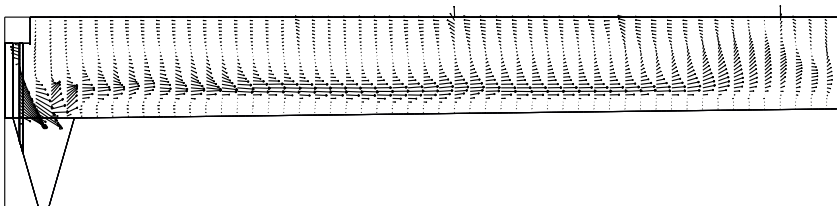
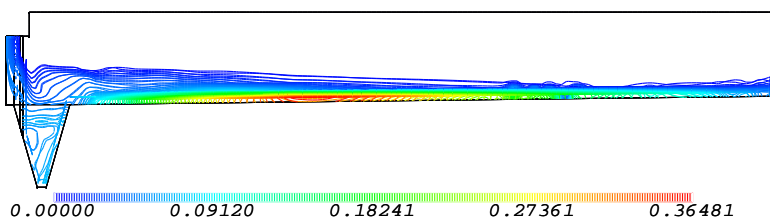
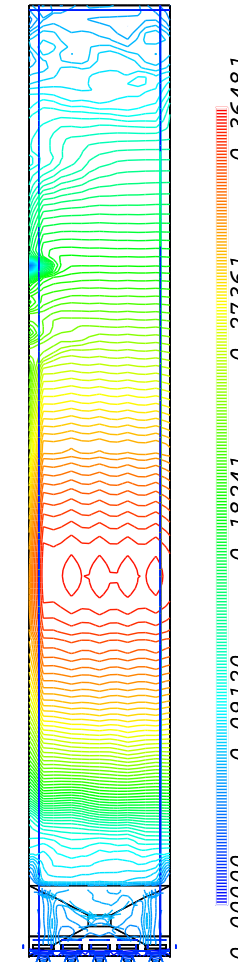


Figure 7.36: Velocity Field. Density Ratio; 1042:1000.  $z = 1.75\text{m}$ .  $t = 6155\text{s}$ .

Figure 7.37: Velocity Field. Density Ratio; 1042:1000.  $z = 0.5\text{m}$ .  $t = 6155\text{s}$ .Figure 7.38: Velocity Field. Density Ratio; 1042:1000.  $z = 3.75\text{m}$ .  $t = 6155\text{s}$ .Figure 7.39: Solids Fraction. Side View. Density Ratio; 1042:1000.  $t = 6155\text{s}$ .Figure 7.40: Solids Fraction. Bed Form Development. Density Ratio; 1042:1000.  $z = 1.75\text{m}$ .  $t = 6030\text{s}$ .

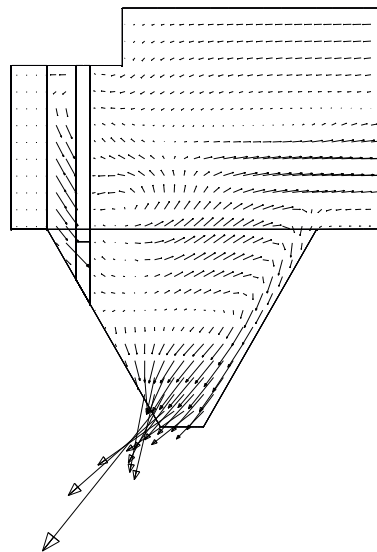


Figure 7.41: Sludge Hopper. Return Sludge Density Current. Density Ratio;1042:1000.

$z = 1.75\text{m}$ .  $t = 6155\text{s}$ .

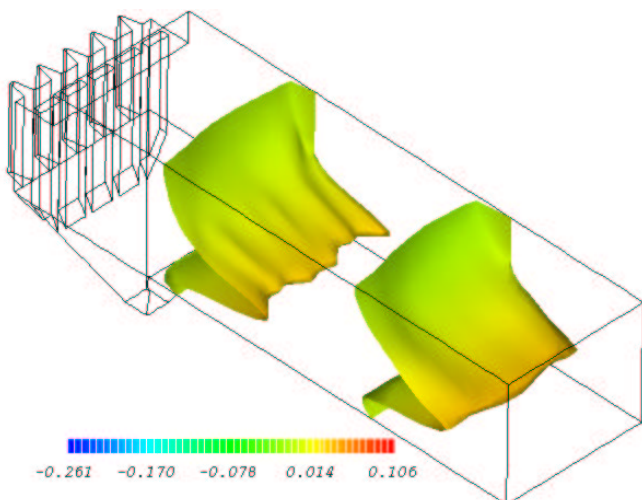


Figure 7.42: Horizontal Velocity Component. 'Mountain Plot'. Density Ratio; 1042:1000.

$t = 6155\text{s}$ .

A plan view of the solids fraction distribution on the tank floor is shown in Figure 7.40. It indicates an essentially uniform solids fraction distribution in the settled bed across the width of the tank at floor level. The plot can also be considered as indicative the depth of settled sludge on the tank floor. The peak concentration appears less than a third of the way along the main body of the tank, so it is also reasonable to assume the sludge is deepest here. The iso-concentration lines exhibit pronounced rippling in the high concentration region and generally, in the region of steep changes in concentration gradient below the density current. It is reasonable to assume that the surface of the settled bed region exhibits this rippling. It can be observed that the indentations or gullies correspond to the locations of the flow through the baffles at the inlet. Similarly the peak regions on the iso-concentration lines correspond to the location in the width-wise direction of the baffles at the inlet.

The uniformity of these features, particularly in areas of high solids fraction, indicates that solids fraction distribution is being affected by inlet geometry as much as half way down the tank. Troughs, or gullies are being left in the surface of the sludge blanket by velocity differences impressed upon the density current by the inlet geometry. The higher velocity currents create the gullies.

Distinct peaks in the density current velocity across the width of the tank can be seen in Figure 7.42. The two surfaces shown represent a 'mountain plot' of the magnitude of the horizontal velocity component at two locations. The section nearest the inlet shows undulations in the velocity field most clearly, again, the peaks correspond to the inlet grating. A section further downstream on the same figure shows the peak value of the density current horizontal velocity component to be more uniform across the width of the tank.

Plots of transverse sections through the vector field are shown in Figures 7.43, 7.44 and 7.45. Figure 7.43 shows a section just downstream of the hopper. The vectors in heaviest print, forming a band in the lower third

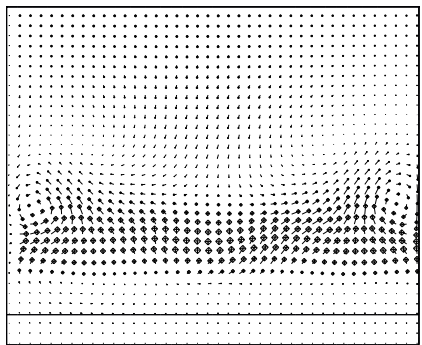


Figure 7.43: Secondary Flow 5m

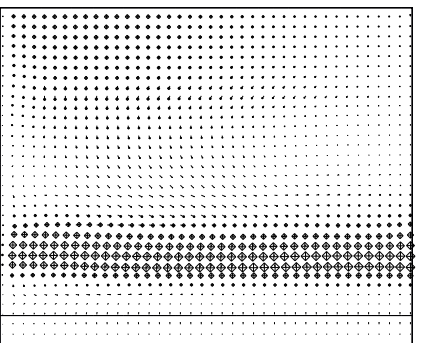


Figure 7.44: Secondary Flow 20m

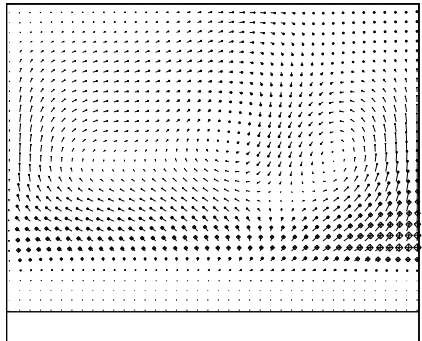


Figure 7.45: Secondary Flow 40m

of the plot, indicate a section through the density current. The peak velocity is at the center of this band.

The transverse section at 5m shows two small counter rotating vortices on the left and right hand side of the density current. This recirculation can be created by the interaction of the density current and the hopper sides as it rises into the main body of the tank. Vorticity of this kind can also be created by density inversions where a higher density fluid overlays a low density region, hence, a combination of tank geometry and density inversion may be the cause this vorticity. Towards the center of the tank the magnitude of the secondary flow pattern is much reduced, with only small upward motion at the interface between the settled bed and the density current.

The transverse section at 20m, Figure 7.44, shows uniformity across the width of the density current with no secondary flows visible within it, indicating this is a very stable region. At 40m, Figure 7.45, secondary flows exist in the upper fluid and seem to disrupt the flow field in the density current.

#### 7.4.5 Simulation with a 2:1 density ratio.

Velocity profiles from the simulation for the inlet dispersed phase density of  $2000 \text{ kg/m}^3$  are compared with the experimental values in Figures 7.46 and 7.47.

It can be seen that the settled bed does not rise to the required height at any point in the simulation, which was curtailed at around 5200s because there had been no noticeable increase in settled sludge depth for most of the latter half of the period. The velocity profiles are close in form to the experimental results at nearly all stations. This is made more apparent if the profiles are moved upward by an amount equal to the depth of the sludge blanket.

Solids fraction plots are compared to the experimental values in Figures 7.48 and 7.49. These results are normalised with the inlet value, in this case  $\alpha_{in} = 0.002$ . This simulation also shows the trend to high values of solids fraction in the settled bed region, here a maximum value of twice the inlet concentration is recorded at  $x = 10\text{m}$ .

A vector plot of a section at  $z = 1.75\text{m}$  is shown in Figure 7.50. It has similar large scale features to those found in the 1.042:1 case, Figure 7.36. The surface return current is shown in Figure 7.51, it is strongest above the region of the thickest mixing layer, the middle part of the tank.

#### 7.4.6 Simulation with a 1.3:1 density ratio.

As part of the inlet condition sensitivity study, the density ratio and density difference between the influent and effluent were adjusted to see which values created a flow field most similar to that found in the experiment.

A suspended sludge density of  $1300\text{kg/m}^3$  with an inlet solids fraction of 0.0034 was found to produce very good agreement with the experimental results. This represented a density difference between the influent and effluent of  $1\text{kg/m}^3$ , half the value of the two previous simulations.

Comparison of the predictions with velocity measurements at 5m and 10m,

Figure 7.52, shows good agreement both along the length of the tank and across its width. The density current is well predicted in terms of both its depth and its maximum velocity. The sludge depth is also well predicted.

For the velocity comparison at 15 to 45m, Figure 7.53, the simulation over-predicts the peak velocity and depth of the density current at 15m, 20m and 25m. However, at the last two stations, 35m and 45m, the numerical simulation and experimental results are in good agreement. This is a very quiescent region at the end of the tank in which the density current has dissipated.

The solids fraction plot at the first two stations, 5m and 10m, Figure 7.54, shows good agreement at all points in the density current and main body of the tank. The simulation shows relatively high solids fraction in the settled bed with a maximum of twice the inlet value.

The main feature of the later stations, 15m to 45m, Figure 7.55, is the characteristic low solids fraction in the upper part of the tank above the density current, evident in both the simulation and the experiment.

Figure 7.56, is an iso-surface plot of solids fraction, 0.003, just below the inlet value of 0.0034. It shows the heavier influent plunging into the hopper from the inlet region. This iso-surface is almost continuous across the hopper. The surface is broken at the top left and right hand corners at the interface with the main body of the tank. This is a consequence of the twin vorticities generated in this region and illustrated on the transverse vector plot for the 1.042:1 density ratio simulation, Figure 7.43. The vortices dilute the dispersed phase concentration in this region by mixing with relatively clear fluid from the region above, hence the break in the iso-surface.

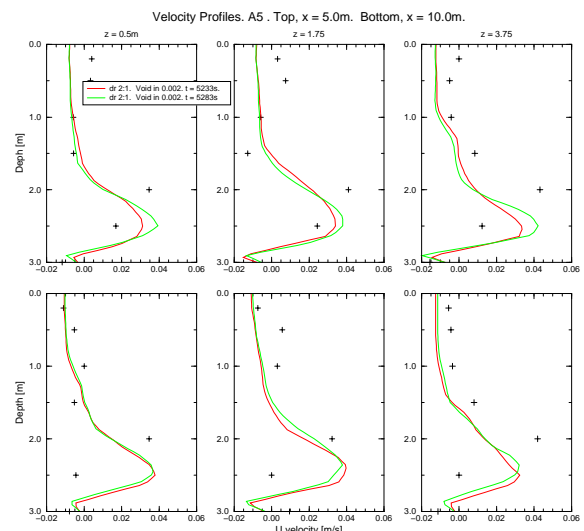


Figure 7.46: Velocity Profiles. Density Ratio 2:1. 3D Simulation.

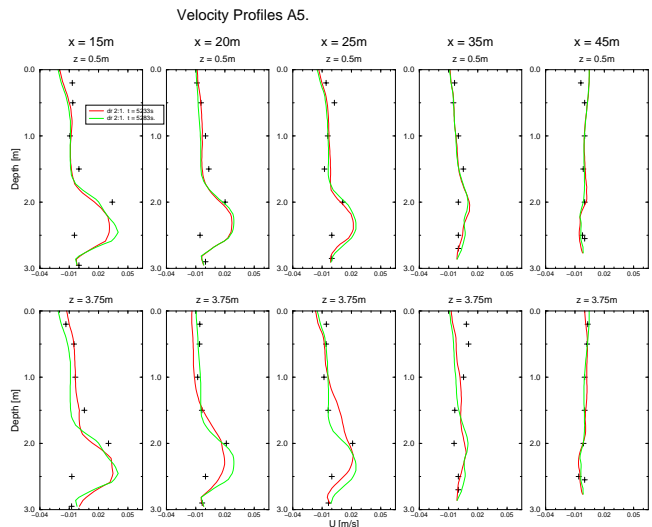


Figure 7.47: Velocity Profiles. Density Ratio 2:1. 3D Simulation.

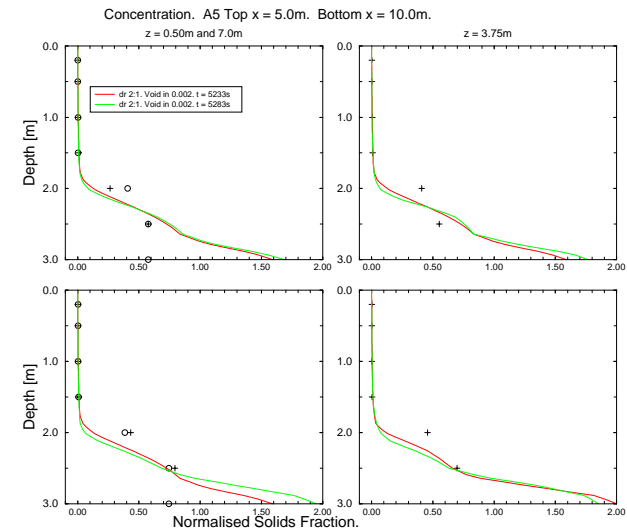


Figure 7.48: Solids Fraction. Density Ratio 2:1. 3D Simulation.

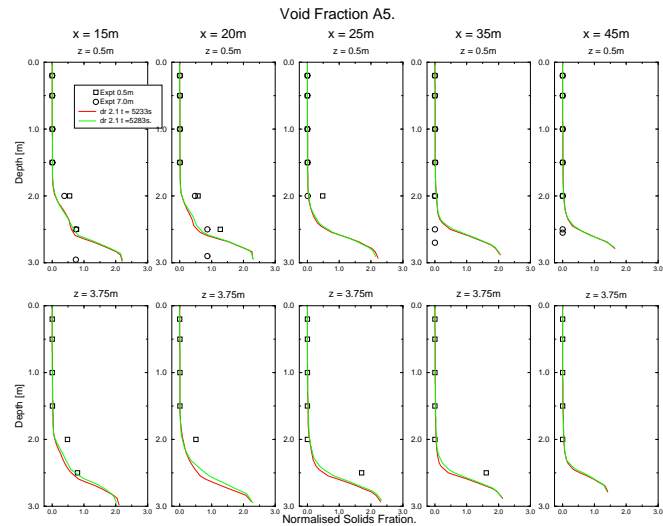


Figure 7.49: Solids Fraction. Density Ratio 2:1. 3D Simulation.

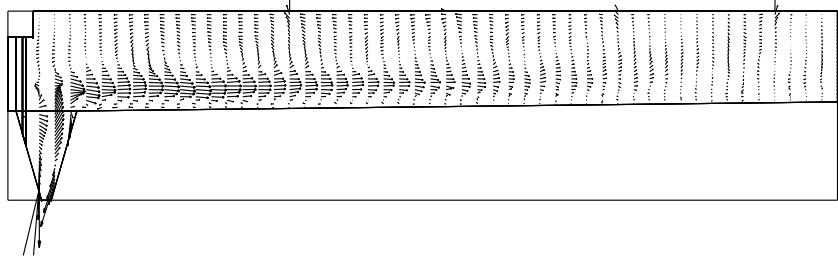
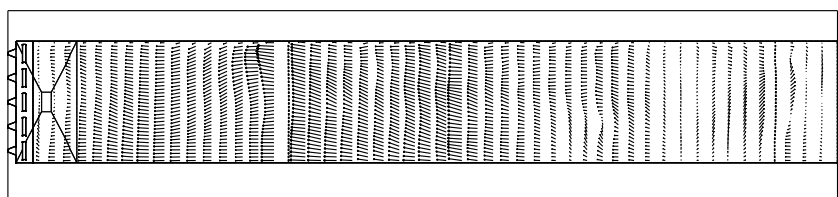
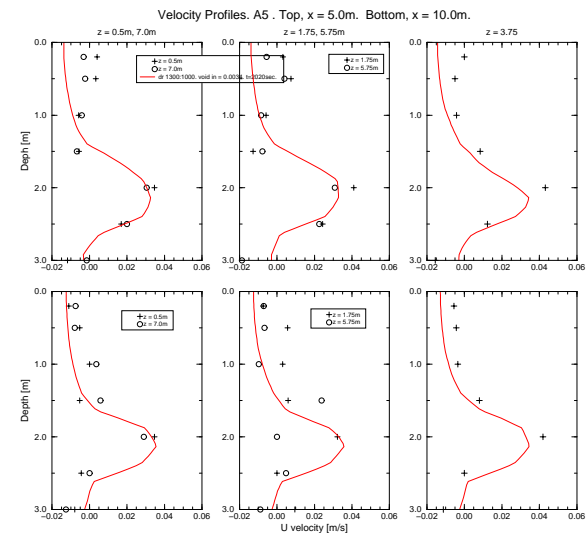
Figure 7.50: Velocity Field. Density Ratio; 2:1.  $z = 1.75\text{m}$ .  $t = 5233\text{s}$ .Figure 7.51: Velocity Field. Surface Return Current. Density Ratio; 2:1.  $t = 5283\text{s}$ .

Figure 7.52: Velocity Profiles. Density Ratio 1.3:1. 3D Simulation.

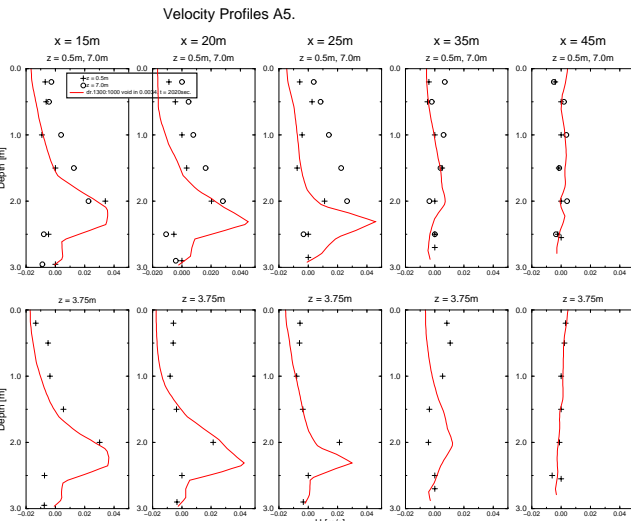


Figure 7.53: Velocity Profiles. Density Ratio 1.3:1. 3D Simulation.

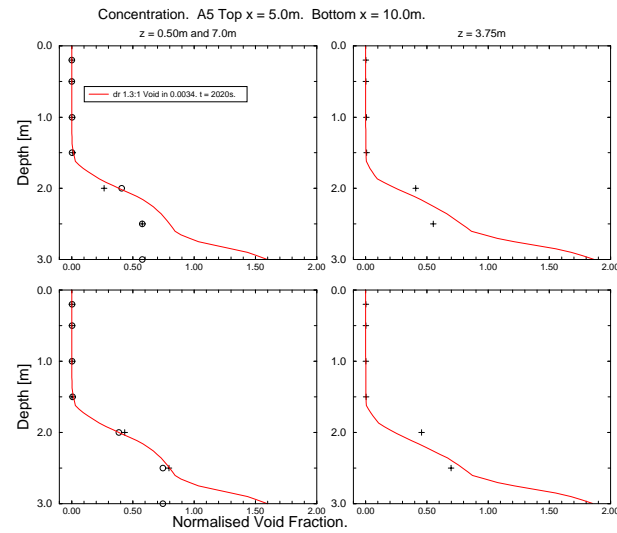


Figure 7.54: Solids Fraction. Density Ratio 1.3:1. 3D. Simulation.

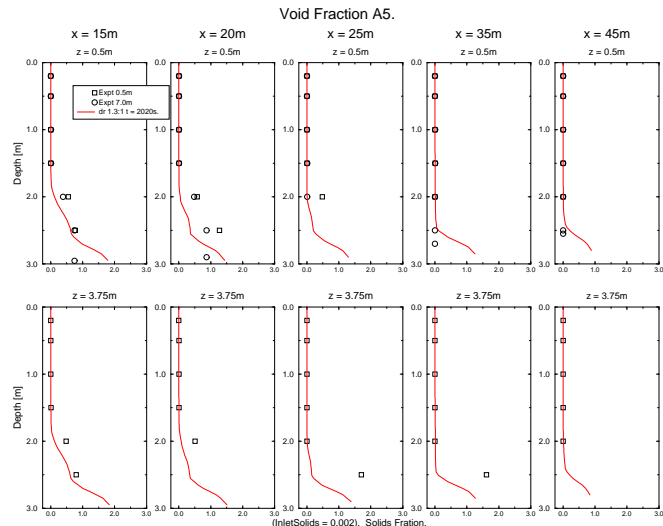


Figure 7.55: Solids Fraction. Density Ratio 1.3:1. 3D Simulation.

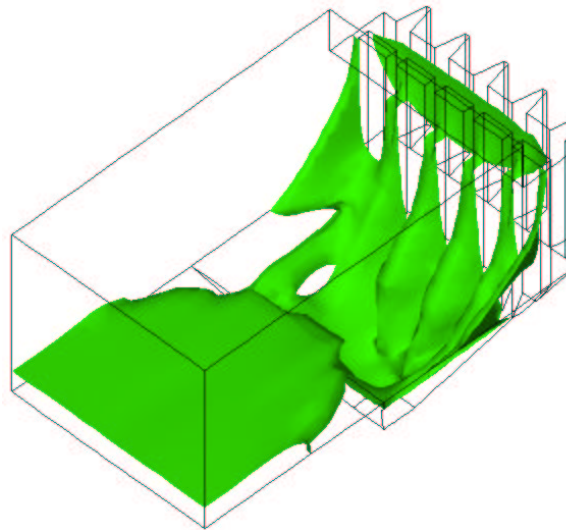


Figure 7.56: Iso Surface. Solids Fraction = 0.003. Density Ratio 1.3:1. 3D Simulation.

### 7.4.7 Mixing and Dispersal of the Density Current

In this section the mixing layer which is formed between the density current and the fluid in the upper part of the tank is discussed. The thickness and the growth rate of this mixing layer is shown to be controlled by the settling velocity of the dispersed phase.

Both the experimental data and the simulation show two distinct forms for the velocity profiles in the density current within the settling tank. Most predominant is the familiar wall-jet-like current with the highest velocities confined to a the lower third of the tank. This form of profile is best illustrated in the results, for  $z = 3.75\text{m}$  at both 5m and 10m, Figure 7.52. A schematic of this shape is illustrated in Figure 7.57, shape a.

Less frequently encountered is a more linear shaped profile, in which the velocity increases uniformly from the top to a maximum near the bottom of the tank. This form is illustrated by the experimental data in Figure 7.53, for  $z = 7.0\text{m}$  ( round plotting symbols ) at 20m and 25m. A schematic of this shape is illustrated in Figure 7.57, shape b.

The most frequently encountered velocity profile, type a, corresponds to a situation whereby a sharp density change takes place between the density current and the fluid above. As has been illustrated in Chapter 4, density stratification inhibits the mixing of the buoyant plume with the fluid above it.

Settling takes place from the density current as it runs along the tank floor, one of the effects of which is to reduce the solids fraction in the upper layers of the current. These then become similar in density to the ambient medium. The suppression of turbulence by density stratification is reduced and turbulent mixing of the upper layers of the density current and the ambient fluid is able to take place. The large velocity gradient between the upper layers of the current and the ambient medium is reduced by turbulent mixing. This amounts to the suppression of the buoyancy term within the buoyancy modified  $k - \epsilon$  model,

equation 4.4. It can be observed that this velocity profile is similar in form to that produced by the standard  $k - \epsilon$  model when applied to buoyancy driven flows Figure 4.8.

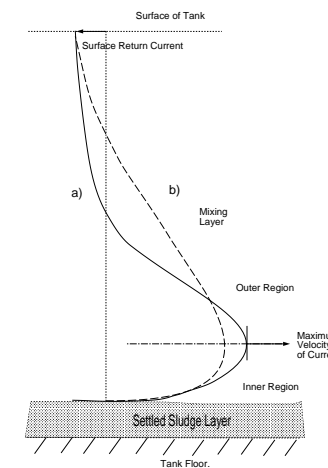


Figure 7.57: Schematic of Density Current Velocity Profiles.

Once settling has taken place from the upper layers of the density current a mixing layer is formed which can be considered to have similar properties to the mixing layer formed in the outer layer or jet region of a wall jet in a constant density fluid. Further settling within the density current allows more fluid to be made available which increases the thickness of this mixing layer. The high gradient in the velocity at the interface of the density current and the fluid above it is further reduced and the velocity profile then has the form illustrated in Figure 7.57, type b.

As has been stated, this mixing layer transfers momentum out of the density current and into the ambient fluid in the tank. The induced motion helps drive the large recirculation zones that occupy the main body of the tank. A schematic illustrating this process is shown in Figure 7.58. The schematic also

illustrates flow field behaviour in the inlet and the viscosity dominated hopper region.

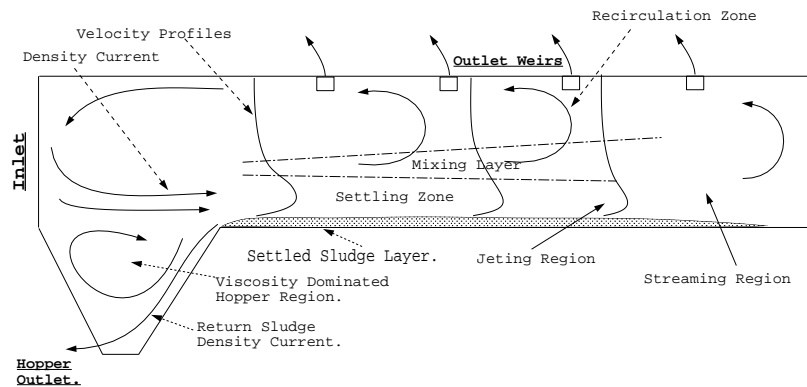


Figure 7.58: Settling Tank Flow Field Schematic.

## 7.5 Conclusions

Calculations of three settling tank geometries at five operating conditions have produced good accuracy in all cases. Generally, the density current velocity profiles and peak velocities have been well predicted as has the solids fraction distribution in the free stream and the settled bed.

The model has helped clarify the nature of the flow field in the hopper, identifying a new density driven current which carries high concentrations of settled sludge from the settled bed to the hopper outlet, it takes over 3000s to fully establish this return sludge density current. The hopper region is dominated by a large, highly viscous recirculation zone which is non-Newtonian in character. The zone separates the influent current and the return sludge density current thus reducing the dilution of the return current and increasing the efficiency of the tank.

The model has also helped illustrate that the flow field in the density current is laminar with very little induced secondary flow.

For the Ueberl case, it was demonstrated that although the measured sludge density is low and the solids fraction high in comparison to previously reported values, the predicted flow field compares well with the data. This indicates that the sludge density has been correctly reported. Using a higher, more commonly reported, dispersed phase density together with appropriately scaled physical properties, produced identical simulations in 2D but not in 3D. The reasons for this are not clear but some numerical instability may have entered the calculation in 3D with the higher dispersed phase density.

The Dahl simulations section 6.4 reproduced good correspondence with the measured velocity field and solids fraction distribution for the cases without the inlet board and for the low volumetric flow rate case with the slot inlet. The high flow rate with this geometry tended to produce a much more confined jet than found in the measurements. The velocity measurements in the Dahl case represent the beginning and the middle of the density current but not its dissipation, the current runs out of the tank via an exit slot before being dissipated, so the dissipation mechanism is not tested in the simulation.

The model has been less successful, however, in predicting the dissipation of the density current in the Ueberl case. Two of the three simulations over predicted the magnitude of the density current in the later part of the tank, from about 20m to near the end wall of the tank.

Some reasons for this were put forward in section 7.3.1. It was demonstrated in the lock exchange simulation, section 6.1, that viscosity plays an important role in the dissipation mechanism. Viscosity in the jetting region of the density current may not be high enough, while the viscosity of the settled bed region exhibits the correct viscous properties. The single exponential relationship for physical properties, equation 6.3, proscribes the viscosity of both the settled bed and the density current, however, it may not be able to

predict the Bingham rheology in both regions equally well at the same time.

It is possible to conclude, however, that the overall agreement is encouragingly good and probably satisfactory for practical purposes.

# Chapter 8

## Summary and Conclusions.

The overall objective of this study has been to create and test a mathematical model of the two-phase flow regime found in settling tanks. The model, in conjunction with a modified pressure interpolation technique, was shown to work well both in resolving the flow field features of the settling tank and in providing a robust numerical solution procedure. This concluding chapter is divided into two sections, namely a summary of the research findings and suggestions for further research to enhance the models performance.

### 8.1 Summary.

In the first two chapters the activated sludge process was described together with the flow field features of settling tanks used within this process. The flow field was seen to be dominated by a density current, driven by the density difference between the influent and the effluent, which flows underneath the less dense tank fluid. The hindered gravitational settling of the dispersed phase takes place mainly from this current, resulting in the formation of a thixotropic settled bed of the dispersed phase over which the density current flows. In addition, the dispersed phase exhibits non-Newtonian shear thinning behaviour characterised by Bingham plastic rheology. Finally, turbulence is

modified by density stratification, inhibiting the mixing of the density current with the surrounding fluid.

The modelling approach was presented in Chapter 3. A Eulerian approach was adopted in which the two-phases are treated as interpenetrating continua. With the two-fluids model, the averaging procedure introduces unknown correlation terms, which include such forces as inter-phase drag, virtual mass and lift, into the phase momentum equations. These terms are difficult to model and are known to introduce numerical instability. However, a simpler equation set can be derived in which the equations of continuity and momentum are added to yield a single continuity equation together with a single mixture momentum equation, based on the mixture centre of mass, in which case the interphase drag terms do not need to be modelled. In order to predict the distribution of the dispersed phase within the mixture, a convection diffusion equation with an imposed settling velocity is also included in the equation set. This is the Drift flux model used in this thesis.

Such simplification in the equation set is possible because of the close coupling of the two phases i.e. the density ratio between the phases is low and the drag high. However, some of the fine details of the motion between the two phases is lost with such simplifications and needs to be expressed by additional constitutive equations based on experimental data i.e dynamic interaction relations are replaced by the constitutive laws.

The most important constitutive relation is for the settling velocity, this is formulated from data extracted from batch settling experiments. Though not a constitutive relationship, both the yield stress and plastic viscosity need to be calculated for any given concentration. These were obtained from published concentration dependent exponential relationships.

Turbulence closure, Chapter 4, is based on the eddy viscosity hypothesis coupled with a two equation buoyancy modified  $k-\epsilon$  model. A comparative calculation at the Densimetric Froude numbers found in settling tanks demon-

strates the necessity of using buoyancy modifications in the  $k-\epsilon$  model as stable density stratification inhibits turbulent mixing at the interface of the density current and the fluid above it, an effect not reproduced by the standard  $k-\epsilon$  model where the density current is quickly dissipated by turbulent mixing. The buoyancy modified flow field was seen to maintain the velocity profile of the density current and bear a closer relationship to the laminar field - such is the suppression of turbulence in this case.

The numerical solution procedure, Chapter 5, based on the finite volume discretisation of the two-phase equation set, has been substantially improved by the introduction of a novel pressure correction technique which improves the robustness and accuracy of simulations of buoyancy dominated flows at low Densimetric Froude number, Weller(1997). It is based on the standard pressure correction equation set developed by Rhie and Chow (1983) for pressure field calculations on co-located meshes. With the new method, the hydrostatic pressure is treated separately and the density gradient at the cell face, explicitly required by this method, is calculated directly from nodal values either side of the cell face - in a similar fashion to the Rhie and Chow interpolation procedure for pressure.

In order to demonstrate the capability of the model developed in this thesis, it was validated against published data gathered from three diverse experimental studies using activated sludge as the working medium, Chapters 6 and 7. In the first, a lock-exchange experiment, Larsen (1977), the ability of the model to accurately predict the measured velocity of a dense incursion for a given excess density was demonstrated. The velocity history of the dense incursion showed closer comparison to experiment as more of the features of the model, most noticeably turbulence and Bingham plastic effects, were included in the calculation.

Comparison was then made with velocity and concentration data gathered in the free stream and settled bed of a model scale tank, Dahl (1993). Two

different inlet geometries, each with two different influent flow rates and concentrations, were studied. Results were extremely encouraging with velocity and concentration being generally well predicted, in addition the Bingham plastic formulation correctly predicts the deposition and re-entrainment of the settled bed giving a generally accurate bed height at any given time. Finally, the model was stable throughout the simulations despite the fact there are large, stagnant, highly viscous areas in the test section for practically the entire duration of the experiment.

The model was then compared with velocity and concentration data gathered by Ueberl (1995) on a full scale tank. This calculation, carried out in 2D and 3D, produced good comparisons with data and revealed some new features of settling tank hydrodynamics. These included the observation that the 'steady state' condition in the hopper takes a considerable amount of time to become established and that the hopper region itself is dominated by non-Newtonian effects. Also present in the hopper is a return sludge density current which brings material from the settled bed through the hopper to the hopper outlet. In addition, it was observed that the settling velocity provides the controlling mechanism for the rate of growth of the mixing layer above the density current. A clearer idea of the distribution of the dispersed phase within the settling tank as a whole was also gained.

The model was less successful in predicting the dispersal of the density current in the latter half of the tank. The Lock-exchange simulation demonstrates that both viscosity and turbulence play a significant role in this respect. This indicates that either the turbulence model may be over prescriptive in suppressing turbulence generation in the dissipation, streaming, region of the density current, or that the viscosity is under predicted in this region, or both. Although the Bingham plastic formulation generally works well, it may not be able to predict the viscosity in the settled bed region and in the dissipation region of the density current equally well at the same time, this will be discussed

more fully in the next section.

## 8.2 Suggestions for Further Research.

Work needs to be carried out to determine why the length of the streaming, low shear, section of the density current is being over predicted. The two most likely dissipation mechanisms, turbulence and shear thinning viscosity, both dependent on shear rate, may be being under predicted in this region.

Firstly, the turbulence model may be too restrictive in the generation of turbulence. This may be a fundamental limitation of the standard  $k-\epsilon$  model as the density gradient is low here and because the buoyancy modification term should be negligible the model should revert to the standard  $k-\epsilon$  equations. Alternatively, the buoyancy term may over predict turbulence suppression for the degree of density stratification actually taking place. Lakehal et al. (1999), have shown that including buoyancy terms in the  $\epsilon$  equation increases the dissipation rate of the density current in the streaming region, lowering velocities found in the latter part of the tank. This may produce closer agreement with experimental results in this region. These effects need to be assessed independently so that modifications to the existing turbulence model can be carried out or other turbulence models tested.

Secondly, the shear thinning viscosity may be under predicted in the streaming part of the density current. The viscosity in the rest of the tank, as seen by the height of the settled bed - which is also shear dependent - and in the jetting or high shear part of the density current, is generally well predicted. The yield stress value is the main controlling parameter on shear thinning viscosity in the tank, it is concentration dependent and is calculated from a general formulae. In the streaming region, the viscous and inertial forces are low and about equal and under these circumstances, adjustments may need to be made to the general formulae coefficients in order to reproduce the correct

yield stress, and hence viscosity, in this region. Further, the role of the plastic viscosity, calculated in a similar fashion to the yield stress, needs to be evaluated more fully. In the extreme, rheological behaviour may deviate from the Bingham model in this area, so the predictive accuracy of different power law fluid models should be investigated in relation to the overall viscous behaviour in the tank.

The major limitation of the Drift flux model is the loss of resolution of the relative motion between phases, due to the removal of the interphase drag terms from the equation set. In settling tanks, the gravitational settling of the dispersed phase is the main cause of inter-phase slip and this is simply accounted for by proscribing a concentration dependent settling velocity. Relative motion in the lateral direction is less easily accounted for, as the nature of the forces which act on the dispersed phase differ in different parts of the tank. For example, in the near bed region of the density current, shear forces are high and can induce a component of motion in the dispersed phase normal to the flow direction. Such forces play an important role in the distribution of the dispersed phase in this region. As a first approximation, it is possible to account for them by considering the resultant force imposed on a given mass of the dispersed phase for the given shear. This force can be converted into a velocity and included directly in the convection diffusion equation for the dispersed phase.

Further improvements can be made in the numerical discretisation procedure particularly in regard to the treatment of density in buoyancy dominated problems. The present method allows for the correct prediction of the pressure field at low Densimetric Froude numbers, at lower Densimetric Froude numbers, i.e low velocity flows with high density gradients, errors and numerical instability can still occur. These arise from the need to interpolate the discretised momentum equation to the cell face in order to calculate the pressure correction. The interpolated coefficients used contain contributions

from density above and below the cell face and linear interpolation does not capture steep changes in density gradient at the cell face, this becomes critical as the density gradient increases and the velocity falls. This error has been reduced by the separate calculation of the hydrostatic pressure gradient but an improved method for calculating the density gradient with problems of very low Densimetric Froude number is still required.

Such improvements in the model need to be validated against a well planned experimental program. Velocity and concentration measurements both need to be taken at as close a time together as possible, methods for doing this in the main body of the tank are reasonably well established. However, measurements of concentration and velocity in the hopper region and concentration measurements in the settled bed also need to be made to give a comprehensive picture of the flow field in the tank. Increasing the capabilities of the model means that the number of quantities measured in experiment has to increase. Most significantly, sludge physical properties; density, settling velocity, yield stress and plastic viscosity all need to be measured as they significantly effect the flow field. Inlet and outlet velocities, or mass flow rates, and concentrations need to be measured and monitored over the course of the experiment in order to provide a complete set of boundary conditions.

$$v_1 = v_{1m} + v_m \quad (A.5)$$

$$v_2 = v_{2m} + v_m \quad (A.6)$$

$$\alpha_1\rho_1v_{1m} + \alpha_2\rho_2v_{2m} = 0 \quad (A.7)$$

where;

$\rho_m$  = mixture density,

$v_m$  = mixture velocity.

$\rho_1, \rho_2$  = density of phase 1 and 2.

$v_1, v_2$  = velocity of phase 1 and 2.

$\alpha_1, \alpha_2$  = void fraction of phase 1 and 2.

also ;  $\alpha_1 = 1 - \alpha_2$

$v_{1m}$  = velocity of phase 1 relative to the mixture centre of mass.

$v_{2m}$  = velocity of phase 2 relative to the mixture centre of mass.

## Appendix A

### Derivation of the Drift Flux Model from the Two Fluid Model.

#### A.1 Mixture Continuity.

For each of the two phases a continuity equation is required.

$$\frac{\partial \alpha_1 \rho_1}{\partial t} + \nabla \alpha_1 \rho_1 v_1 = 0 \quad (A.1)$$

$$\frac{\partial \alpha_2 \rho_2}{\partial t} + \nabla \alpha_2 \rho_2 v_2 = 0 \quad (A.2)$$

Adding equations A.1 and A.2;

$$\frac{\partial (\alpha_1 \rho_1 + \alpha_2 \rho_2)}{\partial t} + \nabla (\alpha_1 \rho_1 v_1 + \alpha_2 \rho_2 v_2) = 0 \quad (A.3)$$

By definition Ishii(1975);

$$\rho_m = \alpha_1 \rho_1 + \alpha_2 \rho_2 \quad (A.4)$$

For the second term in equation (A.3) and using A.5 and A.6 we have;

$$\alpha_1 \rho_1 v_1 + \alpha_2 \rho_2 v_2 = \alpha_1 \rho_1 v_m + \alpha_2 \rho_2 v_m + \alpha_1 \rho_1 v_{1m} + \alpha_2 \rho_2 v_{2m}$$

Substituting A.4 and A.7 into the above we have;

$$\alpha_1 \rho_1 v_1 + \alpha_2 \rho_2 v_2 = (\alpha_1 \rho_1 + \alpha_2 \rho_2) v_m = \rho_m v_m \quad (A.8)$$

Hence the Mixture Continuity Equation is;

$$\frac{\partial \rho_m}{\partial t} + \nabla \rho_m v_m = 0 \quad (A.9)$$

#### A.2 The Mixture Momentum Equations.

The Momentum Equation For each phase is given by;

Momentum Equation, k = 2.

$$\frac{\partial \alpha_k \rho_k v_k}{\partial t} + \nabla \cdot (\alpha_k \rho_k v_k v_k) = -\nabla \cdot (\alpha_k P_k) + \nabla \cdot [\alpha_k (\tau_k + \tau_k^t)] + \alpha_k \rho_k g_k + M_k \quad (A.10)$$

Adding equation A.10 for  $k = 2$  and using the result from equation A.8 for the time derivative term gives;

$$\frac{\partial \alpha_1 \rho_1 v_1}{\partial t} + \frac{\partial \alpha_2 \rho_2 v_2}{\partial t} = \frac{\partial \rho_m v_m}{\partial t} \quad (A.11)$$

And by definition

$$\alpha_1 P_1 + \alpha_2 P_2 = P_m \quad (A.12)$$

For  $k=2$ , the remaining convection terms on the L.H.S of equation A.10 become;

$$\alpha_1 \rho_1 v_1 v_1 + \alpha_2 \rho_2 v_2 v_2 = \alpha_1 \rho_1 [v_{1m}^2 + 2v_{1m}v_m + v_m^2] + \alpha_2 \rho_2 [v_{2m}^2 + 2v_{2m}v_m + v_m^2]$$

Collecting terms;

$$= \alpha_1 \rho_1 v_{1m}^2 + \alpha_2 \rho_2 v_{2m}^2 + 2[\alpha_1 \rho_1 v_{1m} + \alpha_2 \rho_2 v_{2m}] v_m + [\alpha_1 \rho_1 + \alpha_2 \rho_2] v_m^2$$

and using A.6 and A.7

$$= \rho_m v_m v_m + \alpha_1 \rho_1 v_{1m} v_{1m} + \alpha_2 \rho_2 v_{2m} v_{2m} \quad (A.13)$$

or, more generally

$$= \rho_m v_m v_m + \sum \alpha_k \rho_k v_{km} v_{km}$$

For the gravity term;

$$\alpha_1 \rho_1 g + \alpha_2 \rho_2 g = \rho_m g$$

Hence, the Mixture Momentum Equation has the form;

$$\frac{\partial \rho_m v_m}{\partial t} + \nabla \cdot (\rho_m v_m v_m) = -\nabla \cdot P_m + \nabla \cdot [\tau + \tau^t - \sum \alpha_k \rho_k v_{km} v_{km}] + \rho_m g + M_k \quad (A.14)$$

The mixture momentum equation can also be expressed in terms of volumetric fluxes.

Using the relation in A.13 i.e.

$$\alpha_1 \rho_1 v_1 v_1 + \alpha_2 \rho_2 v_2 v_2 = \rho_m v_m v_m + \alpha_1 \rho_1 v_{1m} v_{1m} + \alpha_2 \rho_2 v_{2m} v_{2m}$$

with the identity;

$$v_{1m} = \frac{-\alpha_2 \rho_2}{\alpha_1 \rho_m} v_{2j}; \quad \alpha_1 \neq 0 \quad (A.15)$$

$$v_{2m} = \frac{\rho_1}{\rho_m} v_{2j} \quad (A.16)$$

where  $v_{2j}$  is the volumetric flux of the 2nd phase relative to the mixture velocity, then;

$$\alpha_1 \rho_1 v_{1m} v_{1m} + \alpha_2 \rho_2 v_{2m} v_{2m} = \alpha_1 \rho_1 \left( \frac{\alpha_2 \rho_2}{\alpha_1 \rho_m} v_{2j} \right)^2 + \alpha_2 \rho_2 \left( \frac{\rho_1}{\rho_m} v_{2j} \right)^2$$

collecting common terms;

$$= \frac{\alpha_2 \rho_1 \rho_2}{\rho_m^2} v_{2j}^2 \left[ \frac{\alpha_2 \rho_2}{\alpha_1} + \rho_1 \right]$$

multiply  $\rho_1$  by  $\frac{\alpha_1}{\alpha_1}$

$$\frac{\alpha_2 \rho_1 \rho_2}{\rho_m^2} v_{2j}^2 \left[ \frac{\alpha_2 \rho_2}{\alpha_1} + \frac{\alpha_1 \rho_1}{\alpha_1} \right]$$

the term in brackets is  $\frac{\rho_m}{\alpha_1}$ , hence;

$$\alpha_1 \rho_1 v_{1m} v_{1m} + \alpha_2 \rho_2 v_{2m} v_{2m} = \frac{\alpha_2}{1 - \alpha_2} \frac{\rho_1 \rho_2}{\rho_m} v_{2j}^2$$

The Mixture Momentum has the form;

$$\begin{aligned} \frac{\partial \rho_m v_m}{\partial t} + \nabla \cdot (\rho_m v_m v_m) &= \\ -\nabla \cdot P_m + \nabla \cdot [\tau + \tau^t] - \nabla \cdot \left( \frac{\alpha_d}{1 - \alpha_d} \frac{\rho_c \rho_d}{\rho_m} v_{dj} v_{dj} \right) &+ \rho_m g + M_m \quad (\text{A.17}) \end{aligned}$$

### A.3 Continuity Equation for the Dispersed Phase.

As before, the continuity equation for the dispersed phase can be written;

$$\frac{\partial \alpha_2 \rho_2}{\partial t} + \nabla \alpha_2 \rho_2 v_2 = 0 \quad (\text{A.18})$$

from equation (A.5);

$$v_2 = v_{2m} + v_m$$

but from equation (A.16);

$$v_{2m} = \frac{\rho_1}{\rho_m} v_{2j}$$

On substitution into equation (A.1), we have;

$$\frac{\partial \alpha_2 \rho_2}{\partial t} + \nabla \alpha_2 \rho_2 \left( v_m + \frac{\rho_1}{\rho_m} v_{2j} \right) = 0 \quad (\text{A.19})$$

The continuity equation for the dispersed phase is thus;

$$\frac{\partial \alpha_2 \rho_2}{\partial t} + \nabla \alpha_2 \rho_2 v_m = -\nabla \left( \frac{\alpha_2 \rho_1 \rho_2}{\rho_m} \right) v_{2j} \quad (\text{A.20})$$

## References

- Adams, E., W. and Rodi, W.  
Modelling flow and mixing in sedimentation tanks.  
Journal of Hydraulic Engineering, ASCE, 116(7), 1990.
- Adams, E., W. and Stamou, A., I.  
A study of the flow in a two-dimensional model settling basin. 1: Slot inlet.  
SFB210/E/40, Institute of Hydromechanics, Univ of Karlsruhe, West Germany, 1988.
- Alhanati, F., J., S and Shirazi, S., A.  
Numerical Simulation of Gas-Liquid Flow Inside a Downhole Centrifuge.  
FED-Vol 185 Numerical Methods in Multiphase Flows.  
ASME 1994.
- Auton, T., R.  
The dynamics of bubbles drops and particles in motion in liquids.  
PhD thesis Cambridge University, 1983.
- Barnea, E. and Mizrahi, J.  
A Generalised Approach to the Fluid Dynamics of Particulate Systems.  
Part 1. General Correlation for Fluidisation and Sedimentation in Solid Multiparticle Systems.
- Barr, D., I., H.  
Densimetric exchange flow in rectangular channels.  
La Houille Blanche No. 7, 739-753. 1964.
- Bird, R. B., Armstrong R. C. and Hassager O.  
Dynamics of Polymeric Liquids: Volume 1 - Fluid Mechanics.  
2nd Edition, John Wiley and Sons, New York. 1987.
- Bokil, S. D., and Bewtra J. K.  
Influence of Mechanical Blending on Aerobic Digestion of Waste Activated Sludge.  
6th Int. Conf. on water Pollution Research, Jerusalem, Israel. 1972.
- Bond, A.  
Behaviour of Suspensions.  
Civil Engineering Transactions of the Institution of Engineers.  
Australia (March 1959).
- Boussinesq, V., J.  
Mem. Pres. Par Div. Saveants a l'Acad.Sci. Paris.  
p46 1887.
- Boutekedjiret, A., H., R., Haboussi, M, and Djellouli, R.  
An Euler 3D-Asymptotic Model Describing a Dispersed Two-Phase Flow in a Duct.  
Computational Fluid Dynamics  
1994.

Bretscher, U., and Hager, W. H.  
Stromungs- und Absetzverbesse-rungen bei Nachklärbecken.  
Gas-Wasser-Abwasser, 70(7), 495-499. 1990.

Bretscher, U., Krebs, P., and Hager, W., H.  
Improvement of flow in final settling tanks.  
J. Envir Engng. 118(3), 307 - 321. 1992.

Casey, T., J., L'Hermite, P., Newman, P., J.  
Proceedings of a Workshop held in Dublin.  
Reidel Publishin Company.  
July 1983

Celik, I., Rodi, W. and Stamou, A.  
Prediction of hydrodynamic characteristics of rectangular settling tanks.  
Proc. of the Int. Symp. Refined Flow Modelling and Turbulence Measurements, Iowa City, Iowa, 641-651. 1985.

Celik, I., and Rodi, W.  
Modelling Suspended Transport in Nonequilibrium Situations.  
Journal of Hydraulic Engineering,  
Vol 114, No. 10 1988.

Chapman, B., K. and Leighton, D., T.  
Dynamic Viscous Resuspension.  
Int. J. Multiphase Flow. Bol. 17 No.4, pp 469-483. 1991.

Clerides, D.

Numerical Simulation of Spray Processes in Diesel Engines.  
Ph.D. thesis.  
Imperial College of Science Technology and Medicine, University of London.  
1997.

Cordoba-Molina, J., F., Hudgins, R., R., Silverston, P., L.  
The Gravity Clarifier as a Stratified Flow Phenomenon.  
Canadian Journal of Chemical Engineering.  
Vol. 57, 1979, pp.24

Dahl, C., P.  
Numerical modelling of flow and settling in secondary settling tanks.  
Ph.D thesis, Dept of Civil Engineering, Aalborg Univeristy, Denmark. 1993.

Dahl, C., P., Larsen, T. and Peterson, O.  
Numerical Modelling and Measurement in a Test Secondary Settling Tank.  
Wat. Sci. Tech. Vol.30., No 2, 219-228. 1994.

Danon, N., Wolfstein, M. and Hetroni, G.  
Numerical Calculations of Two-Phase Turbulent Round Jet.  
Int J. Multiphase Flow.  
Vol 3. pp223-234. 1976.

Davies, L. and Dollimore, D.  
Sedimentation of Suspensions: Implications of Theories of Hindered Settling.  
Powder Technology 13, 123-132. 1976.

Dick, R., I. and Buck, J.,H.  
Measurement of activated sludge rheology.

Proceeding of the Environmental Engineering Division, ASCE,  
Vol. 111, pp. 539-545. 1985.

Dick, R., I. and Ewing, B.  
The rheology of activated sludge.  
J. Water Pollution Control Fed.,  
39(4) 543-560. 1967.

Dittmar, D., F. and Okuda, C.  
West Point treatment plant predesign secondary sedimentation evaluation -  
dye testing tech memo San Jose Creek Water Reclamation Plant.  
Report No. A7110-215, Seattle Metro, Seattle, Wash. 1987.

DeVantier, B., A. and Larock, B., E.  
Modelling a recirculation density driven turbulent flow. Int. J. for Numerical  
Methods in Fluids, 6(4), 241-253. 1986.

DeVantier, B., A and Larock, B., E.  
Modelling sediment-induced density currents in circular clarifiers: full scale  
measurements and numerical modelling.  
Wat. Res. 32(10), 2951-2958. 1987.

Drew, D., A. and Wallis, G., B.  
Fundamentals of two-phase flow modelling. In Third International Workshop  
on Two-phase Flow Fundamentals, Imperial College, London 1992.

Elghobashi, S.  
On Predicting Particle-Laden Turbulent Flows.  
Applied Scientific Research 52: 309-329 1994.

Favre, A.  
Statistical equations of turbulent gases. In Problems of Hydrodynamics and  
Statistical Mechanics, SIAM, Philadelphia, PA, 1969.

Ferziger, J.,H. and Peric, M.  
Computational Methods for Fluid Dynamics.  
Heidelberg: Springer 1996.

Fredsoe Jorgen.  
Modelling of non-cohesive sediment transport processes in the marine environment.  
Coastal Engineering 21, pp 71-103, 1993.

Gupta, R., Cheremisinoff, N., P.  
Handbook of Fluids in Motion.  
Ann Arbor Science Publishers.  
ISBN 0-250-4045803 1983.

Hanel, K.  
The Biological Treatment of Sewage by the Activated Sludge Process.  
Edited by Hemmings B. D and Chambers B.  
Ellis Horwood Ltd. 1988.

Heinke, G., W., Quazi, M., A., and Tay, A.  
Design and Performance Criteria for Settling Tanks.  
Research Program for the Abatement of Municipal Pollution within th Provi-  
sions of the Canada-Ontario Agreement on Great Lakes Water Quality.  
Ministry of the Environment, Vol .II Research Report No. 56.

Hermann, F., Issler, D., and Keller, S.

Towards a Numerical Model of Powder Snow Avalanches.

Computational Fluid Dynamics.

1994.

Hill, D., P.

The Computer Simulation of Dispersed Two-Phase Flows.

Ph.D Thesis.

Imperial College of Science Technology and Medicine, University of London.

October 1998.

Hinze, J., O.

Fundamentals of the Hydrodynamic Mechanism of Splitting in Dispersion Processes.

AIChE Journal, Vol 1, No 3, pages 289-295, 1955.

Hultman, B., et al.

Slamfortjockning. Matematisk beskrivning av diskontinuerlig sedimentering.

Publ 71:7, Inst for vattenforsjning-och avloppsteknik, KTH, 1971.

Ikonomu, E., A.

Computational Study of Diesel Sprays and Combustion. Ph.D. thesis

Imperial College of Science Technology and Medicine, University of London.

October 1995.

Imam, E.,H.

Numerical Modeling of Rectangular Clarifiers.

Thesis presented to the University of Windsor, Windsor Ontario, in partial

fulfillment of the requirement of the degree of Doctor of Philosophy.

1981.

Imam, E., McCorquodale, J., A, Bewtra, J., K.

Numerical Modelling of sedimentation tanks.

J. Hydr. Engrg.,ASCE, 109(12), 1740-1754. 1983

Ishii, M.

Thermo - fluid Dynamic Theory of Two - phase Flow

Eyrolles.

1975.

Ishii, M. and Zuber, N.

Drag Coefficient and Relative Velocity in Bubbly,  
Droplet and Particle Flows.

AIChE Vol 25, No 5 1979

Issa, R., I

Solution of the implicitly discretised fluid flow equations by operator-splitting  
Journal of Computational Physics, 62(1):40-65, January 1986.

Ives, I., J. (Editor)

The Scientific Basis of Flocculation.

Sijhoff and Noordhoff

Alpen aan den Rijn - The Netherlans. 1978.

Jasak, H.

Error analysis and estimation for finite volume method with applications to  
fluid flow. PhD thesis, Imperial College of Science Technology and Medicine,

- University of London, 1996.
- Jones, W., P. and Launder, B., E.  
Int. J. Heat and Mass Transfer.  
15:301 1972.
- Kralj, C.  
Numerical simulation of diesel spray.  
PhD thesis, Imperial College of Science Technology and Medicine,  
University of London, 1993.
- Krebs, P., Stamou, A., I., Garcia-Heras, J., L., and Rodi, W.  
Influence of inlet and outlet configuration on the flow in secondary clarifiers.  
Water Sci. and Technol. 24(5-6) 1-9, 1996.
- Lau, Y., L, Krishnappan.  
Does Reentrainment Occur During Cohesive Sediment Settling.  
Journal of Hydraulic Engineering, Vol 120, No. 2 February 1994.
- Lakehal. D., Krebs, P., Krijgsman, J., Rodi, W.  
Computing Shear Flow and Sludge Blanket in Secondary Clarifiers.  
Journal of Hydraulic Engineering.  
ASCE, 125 (3), 253-262. 1999.
- Lam, C.,K.,G. and Bremhorst, K.  
Journal of Fluids Engineering  
Vol 103, 1981.
- Larsen, P.

- On the Hydraulics of Rectangular Settling Basins.  
Report No. 1001, Dept of Water Res. Engrg.  
Lind Institute of Technology, Lund, Sweden. 1977.
- Landman, K., A. and White, L., R.  
Determination of the Hindered Settling Factor for Flocculated Suspensions.  
AIChE Journal. Vol 38, No. 2. 1992.
- Launders, B. E and Spalding, D. B.  
The numerical computation of turbulent flows.  
Comp. Methods Appl. Mech. Engrg., 3, 269-289. (1974).
- Li, D., Ganczarczyk, J., J.  
Stroboscopic Determination of Settling Velocity, Size and Porosity of Activated Sludge Flocs.  
Wat. Res. Vol 21. No 3. pp257-262. 1987.
- Li, J. and Ganczarczyk, J. J.  
Size distribution of activated sludge flocs.  
Research journal of the Water Pollution Control  
JUL 01 v 63 n 5, page 806. 1991.
- Lick, W.  
Entrainment, deposition and transport of fine-grained sediments in lakes.  
Hydrobiologia, 91, 31-40. 1982.
- Lixing, Z.  
Theory and Numerical Modelling of Turbulent Gas-Particle Flows and Combustion.

CRC Press Inc.  
ISBN 0-8493-7721-8. 1993.

Lyn, D., A. and Rodi, W.  
Turbulence Measurements in a Model Settling Tank.  
Journal of Hydraulic Engineering  
Vol 116 No 1  
January 1990.

Lyn, D.,A. Stamou, A.,I., Rodi, W.  
Density Current and Shear - Induced Flocculation in Sedimentation Tanks.  
Journal of Hydraulic Engineering  
Vol 118 No 6  
June 1992.

McLaughlin, J., B.  
Inertial migration of a small sphere in a linear shear flow.  
J. Fluid Mech.  
224 261-274. 1991.

Mehta, A., J, Hayter, E., J., Parker, W., R., Krone, R. B., Teeter, A. M.  
Cohesive Sediment Transport. 1: Process Description.  
Journal of Hydraulic Engineering, Vol. 115, No 8, 1989.

Mehta, A. J and Partheniades, E.  
An investigation of the depositional properties of flocculated fine sediments .  
J. Hydrl. Res. 13(4) 361-381 1975.

Metcalf and Eddy.

Wastewater Engineering: Treatment Disposal, Reuse.  
McGraw-Hill Book Co.  
New York, N.Y, 1979.

Miller., D., G.  
Sedimentation; a review of published work.  
Water and Water Engineering, p52-58, February 1964.

Minier P.J and Pozorski J.  
Analysis of Existing Lagrangian Models and New Propositions for Particle Dispersion in Homogeneous Stationary Turbulence.  
Electricite de France  
Report He 44/92.29

O'Donovan, E. J. and Tanner, R. I.  
Numerical study of the Bingham Squeeze Film Problem.  
Journal of Non-Newtonian Fluid Mechanics, 15, pp75-83. 1984.

Oliveria, P. J.  
Modelling of Multidimensional Multiphase Flow and Applications to T-junctions.  
PhD thesis, University of London, 1992.

Oliveria, P. J and Issa, R. I.  
On the Numerical Treatment of Interphase Forces in Two-Phase Flow. FED-  
V0l. 185, Numerical Methods in Multiphase Flows. ASME 1994.

Parchure, T. M and Mehta, A. J.  
Erosion of soft cohesive sediment deposits.  
J. Hydr. Engrg., ASCE, 111(10), 1308-1326. 1985.

Patankar, S., V.  
Numerical Heat Transfer and Fluid Flow.  
McGraw-Hill, 1980.

Patry, G. G. and Takacs, S.  
Settling of Flocculent Suspensions in Secondary Clarifiers  
Water Research Volume 26, No 4, 1992.

Peric, M.  
A Finite Volume Method for the Prediction of Three Dimensional Flow in Complex Ducts. Phd Thesis, University of London 1985.

Politis, S.  
Prediction of Two-Phase Solid-liquid Turbulent Flow in Stirred Vessels.  
PhD thesis, Imperial College of Science, Technology and Medicine, University of London, 1989.

Ramalho, R. S.  
Introduction to Waste Water Treatment Processes.  
Second Edition, Academic Press, 1983.

Rampall I and Leighton D. T.  
Influence of Shear Induced Migration on Turbulent Resuspension.  
Int. J. Multiphase Flow. Vol 20. No 3 pp631-650. 1994.

Rhie, C.,M., and Chow, W.,L.  
A Numerical Study of the Turbulent Flow Past and Isolated Airfoil with Tail-ing Edge Separation.

AIAA Journal, Vol 21, p1525-1532, 1983.

Richardson, J., F. and others.  
Sedimentation and Fluidisation: Part 1-4.  
Trans Instn. Chem. Eng. 32,35. 1954.  
36, 270, 1958. 39, 348, 1961. 39, 357, 1961.

Rodi, W.  
Turbulence Models and Their Applications in Hydraulics, 3rd Edition.  
Balkema, Rotterdam, The Netherlands, 1993.

Roth, M.  
Particle size distribution in secondary effluents.  
Effluent and Water Treatment Journal. 1981.

Schamber, D., R., and Larock, B., E.  
Numerical analysis of flow in sedimentation basins.  
J. Hydr Div, ASCE, 107(5), 575-591. 1981.

Serizawa, A. and Kataoka, I.  
Dispersed Flow - 1. Third International Workshop on Two-Phase Flow Fundamentals.  
Imperial College, London, 1992.

Simonin, O., Uittenbogaard, R. T., Baron, F. and Viollet, P.  
Possibilities and Limitations of the  $k-\epsilon$  Model to Simulate Turbulent Fluxes of Mass and Momentum, Measured in a Steady, Stratified Mixing Layer.  
Proc. 23rd Cong. of the IAHR, National Research Council of Canada, Ottawa, Canada, A-55.

Smethurst, G.  
Basic Water Treatment for Application Worldwide.  
Second Edition, Thomas Telford, 1992.

Speziale, C.,G, Gatski, T., B, Fitzmaurice, N.  
An Analysis of RNG - based Turbulence Models for Homogeneous shear flow.  
Phys. Fluids  
September 1991.

Stamou, A.I.  
On the prediction of flow and mixing in settling tanks using a curvature-modified  $k - \epsilon$  model.  
Appl. Math Modelling, Vol. 15, July, 1991.

Stamou, A.I. and Adams, E. W.  
Study of the hydraulic behaviour of a model settling tank using flow through curves and flow patterns.  
SFB 210/E/36, Inst. of Hydromechanics, Univ. of Karlsruhe, West Germany.  
1988.

Stamou, A.I, Adams, E.W, Rodi, W.  
Numerical Modeling of flow and settling in Primary Rectangular Clarifiers  
Journal of Hydraulic Research. Vol 27, No 5, 1989.

Stamou, A.I and Rodi, W.  
Review of Experimental Studies on Sedimentation Tanks.  
Sonderforschungsbereich 210 / E / 2. Universitat Karlsruhe.  
August 1984.

Stone, H. L.  
Iterative solution of implicit approximation of multidimensional partial differential equations. SIAM J. 5, 530-558. (1968).

Takacs, I, Patry, G. G, and Nolasco, D. A dynamic model of the clarification-thickening process.  
Water Res, 25(10) 1263-1271. 1991.

Tchen, C. M.  
Mean value and correlation problems connected with the motion of small particles suspended in a turbulent fluid. PhD thesis University of Delft, 1947.

Teisson, C., Ockenden, M., Hir, P. Le, Kranenburg, C. and Hamm, L.  
Cohesive sediment transport process.  
Coastal Engineering 21, 162-191, 1993.

Toorman, E., A. and Berlamont, J., E.  
Free Surface flow of a Dense, Natural Cohesive Sediment Suspension.  
Computational Fluid Dynamics Volume 2, 1992.

Ubbink, O.  
Numerical Prediction of Two Fluid Systems with Sharp Interfaces.  
PhD thesis, University of London, 1997.

Ueberl, J.  
Verbesserung der Absetzwirkung von Nachklärbecken.  
Ph.D Thesis, Swiss Federal Institute of Technology ETH, Zurich Switzerland  
(In German.) 1995.

Versteeg, H.,K., and Malalasekera, W.  
An introduction to Computational Fluid Dynamics, the Finite Volume Method.  
Harlow: longman Scientific and Technical, 1995.

Vradis, G.C, and Hammad, K.J.  
Heat Transfer in Flows of No-Newtonian Bingham Fluids Through Axisymmetric Sudden Expansions and Contractions.  
Numerical Heat Transfer Part A.  
28:339-353, 1995.

Wallis, G., B.  
One Dimensional Two-Phase Flow. McGraw Hill, New York, 1969.

Water Quality and Water Treatment.  
A Handbook for Community Water Supplies.  
4th Edition.  
American Water Works Association.  
McGraw Hill.  
1990.

Weller, H.  
Private Communication.  
Imperial College of Science, Technology and Medicine, University of London.  
1997.

Witheridge, G., M and Wilkinson, D., L.  
Density Measurement of Particle and Floc Suspension.  
Journal of Hydraulic Engineering, Vol 115, No 3, March (1989).

Zhang, K., and Acrivos, A.,  
Viscous resuspension in fully developed laminar pipe flows.  
Int. J. Multiphase Flow. Vol 20. No 3, pp 579-591, 1994.

Zhou, S., and McCorquodale., J., A.  
Modeling of Rectangular Settling Tanks.  
Journal of Hydraulic Engineering  
Vol 118, No 10, 1391-1405. 1992.

Zuber, N., Staub, F., W. and Bijwaard, G.  
Steady State and Transient Void Fraction in Two-Phase Flow Systems. Vol.  
1. GEAP 5417. 1964b.